Hybrid non-destructive technique for volumetric defect analysis and reconstruction by remote laser induced ultrasound

A thesis submitted for the degree of Doctor in computational and Applied physics

Hossam Selim

Directors

Prof. Crina Cojocaru

Prof. Miguel Delgado

Physics Department

Universitat Politècnica de Catalunya (UPC)

June 2020

Barcelona, Spain

UNIVERSITAT POLITÈCNICA DE CATALUNYA BARCELONATECH

Declaration

This thesis has not been submitted in support of an application for another degree at this or any other university. It is the result of my own work and includes nothing that is the outcome of work done in collaboration except where specifically indicated. Many of the ideas in this thesis were the product of discussion with my supervisors.

Conflicts of Interest: The authors declare no conflicts of interest. The funders had no role in the design of the study; the collection, analyses, or interpretation of data; the writing of the manuscript, or the decision to publish the results.

Resumen

Esta tesis doctoral versa sobre el diseño, estudio e implementación de un método híbrido, sin contacto, de ensayos no destructivos (NDT, non-destructive testing) para el análisis de objetos metálicos que contienen defectos o fracturas internas. Proponemos una técnica híbrida opto-acústica que combina ultrasonidos generados por impacto láser como excitador y transductores de ultrasonidos como receptores. El trabajo plantea un estudio detallado de la detección y reconstrucción en 1D, 2D y 3D de defectos presentes en un objeto metálico, usando la técnica híbrida de NDT sin contacto y controlado remotamente. Nuestro dispositivo presenta varias ventajas de las técnicas fotónicas y de ultrasonidos, reduciendo al mismo tiempo algunos inconvenientes de dichos métodos tomados por separado. Nuestro método combina resultados experimentales con simulaciones numéricas basadas en el procesado de señal de alta resolución. El montaje experimental consiste en un láser pulsado de ns a una longitud de onda de 532 nm, que impacta sobre la superficie del objeto. El pulso láser se absorbe, creando una expansión termoelástica localizada que induce un pulso de ultrasonidos de banda ancha que se propaga en el material. El láser, controlado remotamente, realiza un barrido sobre un área seleccionada de la superficie del objeto. Por cada punto de excitación, el ultrasonido se propaga a través del objeto y se refleja o dispersa en los defectos del material. Dichas ondas se detectan mediante transductores y se registran en un sistema de adquisición de datos para su ulterior procesado. En un primer paso, mediante el análisis del tiempo de vuelo, podemos localizar y determinar el tamaño del defecto en una vista 1D. Las capacidades de detección de defectos internos en una muestra metálica se estudian también mediante transformación wavelet debido a sus características de multi-resolución en tiempo y frecuencia. Se aplica un algoritmo novedoso de agrupamiento (clustering) espacial y se usan los mapas resultantes de tiempo y frecuencia para estimar la posición del defecto. Para la

visualización 2D de los defectos ampliamos el análisis de la señal utilizando la técnica de focalización por apertura sintética (SAFT, synthetic aperture focusing technique). Implementamos un novedoso filtro de apodización 2D, juntamente con la técnica SAFT, y demostramos que elimina efectos no deseados, mejorando la resolución de la imagen reconstruida del defecto. El siguiente paso es un análisis y reconstrucción 3D. En este caso conseguimos una configuración experimental totalmente automatizada y sin contacto, permitiendo áreas de barrido sobre diferentes caras de un objeto. Los detalles de los defectos se registran desde diferentes ángulos, consiguiéndose una completa reconstrucción 3D. Finalmente, mostramos nuestros resultados en un tema complementario, relacionado con un caso particular de propagación de ultrasonidos en sólidos. Desde un primer momento, quisimos tener una comprensión física de la propagación y difracción de ondas de ultrasonidos en materiales sólidos. El control de los patrones de difracción en sólidos, mediante el uso de lentes ultrasónicas, ayudaría a la focalización/colimación del ultrasonido, reduciendo ecos y reflexiones en la superficie de contorno, mejorando del proceso de análisis NDT. Los cristales fonónicos se usan para regular la difracción y la respuesta en frecuencia de ondas de ultrasonido que se propagan en fluidos. No obstante, dichas estructuras se han estudiado mucho menos en materiales sólidos. Hemos realizado detalladas simulaciones numéricas de la propagación de ultrasonidos en un cristal fonónico sólido y hemos demostrado efectos de focalización y autocolimación. Finalmente hemos acoplado nuestra lente de cristal fonónico al sólido objeto de estudio, demostrando que el control de la difracción se conserva en el interior de dicho objeto a través del material de acoplamiento.

Finalmente, proporcionamos una conclusión general sobre el trabajo declarado en esta tesis y un plan de trabajo futuro donde esta investigación puede extenderse y expandirse aún más a aplicaciones industriales en colaboración con el mercado de producción.

Abstract

This PhD thesis is devoted to the design, development and implementation of a non-contact hybrid non-destructive testing (NDT) method applied to the analysis of metallic objects that contain embedded defects or fractures. We propose a hybrid opto-acoustic technique that combines laser generated ultrasound as exciter and ultrasound transducers as receivers. This work envisages a detailed study of the detection and one, two or three-dimensional reconstruction of defects, using the proposed hybrid technique and its application as a remotely controlled non-contact NDT. Our device combines several advantages of both photonic and ultrasonic techniques, while reduces some of the drawbacks of both individual methods. Our method relay on the combination of experimental results with high-resolution signal processing procedures based on different mathematical algorithms. Our basic experimental setup uses a nanosecond pulsed laser at 532nm wavelength that impacts onto the surface of the object under study. The laser pulse is rapidly absorbed into a shallow volume of material and creates a localized thermo-elastic expansion inducing a broadband ultrasound pulse that propagate inside the material. The laser beam scans a selected area of the object surface, being remotely controlled by means of a programmable XY scanner. For each excitation point, the ultrasound waves propagate through the object are reflected or scattered by material 3D defects. They are detected by ultrasound transducers and recorded with a PC data-acquisition system for a further process and analysis. As a first step, the time of flight analysis provides enough data for the location and size of the defect in 1D view. The detection capabilities of internal defects in a metallic sample are studied by means of wavelet transform, chosen due to its multi-resolution time-frequency characteristics. A novel algorithm using a density-based spatial clustering is applied to the resulting time frequency maps to estimate the defect's position. For the 2D visualization and reconstruction of the defects we extended the signal analysis using the synthetic aperture focusing

technique (SAFT). We implement a novel 2D apodization window filtering applied along with the SAFT, and we show it removes undesired effects of the side lobes and wide-angle reflections of ultrasound waves, enhancing the reconstructed image of the defect. We move then towards the 3D analysis and reconstruction of defects and in this case we achieve and implement a fully non-contact and automatized experimental configuration allowing the scan areas on different object's faces. The defect details are recorded from different angles/perspectives and a complete 3D reconstruction is achieved. Finally, we show our results on a complementary topic related to a particular case of the ultrasound propagation in solids. We were concerned on the physical understanding of the propagation and diffraction of ultrasound waves in solid materials from the first moment. The control of the diffraction pattern in solids, using an ultrasonic lens, would help focus/collimate the ultrasound reducing echoes and boundary reflections, resulting in a further improve NDT process. Phononic crystals have been used to regulate the diffraction and frequency response of ultrasonic waves traveling in fluids. However, they were much less studied in solid materials due to the difficulty of building the crystal and to high coupling losses. We perform detailed numerical simulations of the ultrasound propagation in a solid phononic crystal and we show focusing and the self-collimation effects. We further extend our analysis and couple our phononic crystal lens to a solid under study, showing that the diffraction control is preserved inside the target solid object trough the coupling material.

Finally, we provide a general conclusion about the stated work in this thesis and a future work plan where this research can be further extended and expanded to industrial applications in collaboration with production market.

Preface

In this workwe focus on the non-destructive testing (NDT) of metallic objects that may contain embedded defects or fractures of different size and shape. We study the damage detection and visualization using a laser induced ultrasound approach We propose and implement a hybrid system that combines laser-induced ultrasound as an exciter with a conventional contact or noncontact ultrasound transducers as a receiver. This method combines advantages of both technologies to obtain a contactless, and remotely controlled one-dimensional, two-dimensional or even three-dimensional reconstruction of an embedded defect with good resolution, and to improve the applicability of the system in industrial applications.

In Chapter 1 we present a brief introduction about the main concepts used in this study and a review of the related research in scientific and academic literature. In addition, a description of the objectives of the work achieved and subsequent constraints are presented.

In Chapter 2 we present the general purpose and the basic experimental configuration, followed by a description of the block diagram of the signal processing algorithms. We implement a simple configuration of the experimental set-up and we apply a first algorithm of signal processing to the acquired data. We show the results of one-dimensional (1D) defect reconstruction using 1D laser-ultrasounds experimental scanning process, namely B-scan. We use contact transducers as receivers, coupled to the surface of the object for the detection of the individual A-scan signals. Finally, we compare these results with those we obtain from a classical commercial device that uses an ultrasound array for both excitation and detection.

In Chapter 3, we improve the experimental configuration implementing a two-dimensional (2D) laser scanning system onto the sample surface. We again use fixed contact transducers for the ultrasound detection. We also

improve the signal processing by using wavelet transform (WT) analysis and clustering techniques. This study allows us to obtain a 2D defect reconstruction with a corresponding analysis of the quality and accuracy of the reconstruction.

The wavelet transform is proposed as a time-frequency processing tool. We study the characteristic damage-frequency-patterns, identified and tracked back to the boundaries of the source, i.e., the damage spatial location in the component under inspection. Then, a damage reconstruction procedure is proposed based on the estimated time of flights of the ultrasound damage propagation patterns. The contribution of this study lies in providing a new approach of damage detection, localization, and shape reconstruction based on the detection and processing of the damage ultrasound echo. We chose an adaptive resolution method using WT in order to check the proposed methodology under a hybrid laser induced ultrasound scheme.

Novelties of this work include a new damage pattern tracking method over the WT-based time-frequency maps, and a time of flight-based damage localization and visualization procedure; both are supported by the application of a density-based spatial clustering algorithm in order to identify the highest probability regions of damage location. It must be noticed that for the first time, to the authors' knowledge, this processing scheme and this damage visualization procedure have been used in the laser-ultrasound inspection of metallic specimens. According to the obtained results, the proposed methodology is reliable and feasible for defect detection and quantification of metallic damages in industrial applications since the proposed method does not require any reference information.

In Chapter 4 we upgrade the experimental configuration using a different scanning technique. Contact ultrasound transducers are used in these experiments as well.

We perform different experiments that we discuss in detail, highlighting the resolution enhancement gained by improving the signal processing algorithms. We implement different SAFT algorithms, with or without applying the improved apodization techniques, in comparison to previous chapters. To our knowledge, in the previous literature, SAFT algorithms are mainly applied for scanning the receivers across the scan line/area or scanning both exciters and receivers. Our method envisages higher resolution at wider view angles of the defects and higher signal to noise ratio given the increased number of detected measurements. In addition to the SAFT method, we implement an enhanced 2D apodization function, as a novel contribution that eliminates the side lobes generated by the laser excitation r as an artifact in the input signal. This technique results in improved quality of the reconstructed image with less redundant or unnecessary shadows. To our knowledge, the apodization function for signal processing using the SAFT algorithm was previously applied only to 1D geometries for 2D defect reconstruction. In this work, we have developed the extended 2D synthetic aperture window apodization function with a volumetric SAFT algorithm as an expansion of the commonly used 1D apodization window in the planar SAFT algorithm.

In Chapters 5 we make a step forward and we implement non-contact transducers as receivers. The experimental set-up is now fully non-contact, both for excitation as well as for detection. A 2D motorized stage is used to scan a 2D square onto the surface of the sample. This experimental configuration allows the scanning to be applied on different faces of the object to get different views/angles of the defect from different perspectives. Both the exciter (the laser spot) and the receiver (only one noncontact transducer) are programmed to automatically scan 2D surfaces of three different faces of the object, which emphasizes the 3D reconstruction of the defect at different perspectives/angles. The recorded ultrasound signals are processed and superimposed using the standard SAFT algorithm for 3D defect reconstruction. The results of SAFT at each face gives information

about the defect from one view angle. Superimposing the results of the three faces together is then performed to provide information about the defect from different angles/perspectives. We apply the three faces scanning and SAFT algorithm processing as a contribution to expand the one face scanning for SAFT analysis with the 2D apodization applied. In the last step, we apply a threshold to reject data in the resulting image with intensity amplitude below a certain threshold as an increased enhancement to the final image, resulting in reduced defect size error.

In Chapter 6 we present results of numerical simulation on a complementary topic related to the physical understanding of the propagation and diffraction of ultrasound waves in solid materials. We address the question of the diffraction pattern control in solids, using an ultrasonic lens made by a phononic crystal (PC) made of a periodic arrangement of two different materials. We target a focus/collimation of the ultrasound that would reduce echoes and boundary reflections, resulting in a further improve NDT process. We split the work in two stages. We first consider the PC to be part of the solid object under test. In this case we avoid any effect of acoustic coupling and boundaries between the PC and the object's materials. Secondly, we consider the PC as an external coupling device externally coupling it with the sample surface. The simulations are performed using COMSOL 5.4 and Matlab 2019 software.

Finally, we summarize the general conclusions of the presented work and a discussion of the achieved objectives with a brief information about potential future research work.

At the end of the thesis a list is provided of the bibliography of the cited references in this thesis book.

Keywords

Non-destructive testing (NDT), laser generated ultrasound; 3D defect reconstruction; spectral signal processing; wavelet transform (WT); synthetic aperture focusing technique (SAFT); phononic crystals;

Acknowledgement (1)

This research has been conducted at the Universitat Politècnica de Catalunya (UPC), Barcelona, Spain, as a collaboration between two groups of research:

1 "Nonlinear Dynamics, Nonlinear Optics and Lasers" group (DONLL), Physics Department, (UPC), Terrassa, Barcelona, Spain.

2 "Motion Control and Industrial Applications" (MCIA), Electronic Engineering Department, Terrassa, Barcelona, Spain;

We counted from the beginning on the close collaboration of Dr. Ruben Picó from the Instituto de Investigación para la Gestión Integrada de Zonas Costeras, Universitat Politècnica de València (UPV),Gandia, València, Spain.

The work was supported partially by the Spanish Ministry of Economy and Innovation (MINECO) and European Union FEDER through project FIS2015-65998-C2-1 and by the US Army Research, Development, and Engineering Command (RDECOM) through project W911NF-16-1-0563.

Acknowledgement (2)

First and foremost, all thanks are due to Allah, the arbiter of all success, for giving me strength and endurance to conduct this research despite all hardships, troubles and tight schedules, which all come as a challenging by-product of my career.

I would like to express gratitude to all those who helped me complete this thesis.

I dedicate this work to my director, Professor Crina Cojocaru (DONLL), for her ultimate support, sharing of experience and insights throughout the practical and technical constraints I found in this thesis. She always was making physics problems easy to understand by her deep and clear explanations and discussions. I want to thank her as well for believing in me and giving me the chance to join the PhD research program. She was so patient with me and gave me hope and solutions on the academic level as well as on personal level. She helped me by solving all side problems that could have distracted me for the main goal to concentrate on the research work. She always helped find a project fund to the work of the research to make sure the work continuity never stops. I want to say, without Dr.Crina, it was impossible to be here defending my thesis of doctorate.

Also, I am deeply indebted to my co-director, Professor Miguel Delgado Prieto, (MCIA), whose help, stimulating suggestions, creative ideas, and encouragement were so much useful for me, both in lab and during programming and modelling sessions, throughout the research work and the writing of the thesis. He always treated me as a brother and provided solutions at different levels. The fund support he provided to the experimental equipment, hardware, supercomputer servers. He always had a technological solution to make the signal processing and computer

modelling easier than it looks. His detailed checks on the programming and algorithms to make sure of their accuracy and efficiency gave me the confidence to find more enhanced ideas and developments.

I am deeply grateful to Professor Jose Trull (DONLL), the non-linear optics laboratory director. His hand work with me on preparing all the experiments and his recommendations, advices made the lab sessions for me more interesting and joyful. His ultimate care for my personal safety during experiments and his feeling of responsibility to all co-workers is unbeatable. Even though he was not one of my thesis directors, however, without his presence for me all the duration of the study, the thesis research would have not moved forward ever. All thanks to Professor Jose Trull for his sincerity and integrity.

I would like to express my sincere appreciation to professor Luis Romeral director of the MCIA group as he was always supporting the research with his engineering ideas. His close connection with the industry made it easy to find applications to our work, his funding of the research work in collaboration with my directors helped keep the work going without interruption. He had always given me recommendations and advices to match the work with the industrial challenges. He provided the tools of electronics lab for me to ease the experiments performed in the non-linear optics lab.

During the research, I had several visits to Universitat Politècnica de València, Gandia, València, Spain with direct collaboration of professor Rubén Picó Vila. I have to mention that before starting this thesis I had very basic knowledge about acoustics and ultrasonics, since my Bachelor and master studies were mainly related to electrical, electronics and optical engineering. In addition, the research groups DONLL and MCIA at UPC were mainly focused on Optics and electronics technology. However, with the help of professor Rubén Picó Vila, I found

an easy transition to get deeper knowledge about acoustics and ultrasonics at a theoretical as well as an experimental level. His patience and guidance at this level was greatly helpful and supportive to keep my thesis research up to the efficient level. He supported us by hardware and software capabilities as a collaboration between both UPC and UPV universities. His recommendations and suggestions on the NDT part of the thesis as well the phononic crystal part of the thesis were so much valuable to the research details. His contribution to this thesis was one of the main factors that made the work successful.

Very special thanks to professor Ramon Vilaseca, the head of the DONLL group. He was the first connection I had with UPC university, and he is the reason to connect me with Dr.Crina Cojocaru for the first time, and convinced her that I could be a good PhD student under her supervision. Without his humble and modest assistance to me, this whole research would have just been a dream. Thanks to him, this dream came true. In addition, I was one of his students at the course "Introduction of Photonics" that was one of the best courses I ever had in my life. He was explaining such a complicated field of science with a smooth and easy to understand way that made it look like a simple subject. He was one of the best professors who taught me a course ever in my life. I am thankful for him creating such a great research group and for the whole group we consider him our God father.

Special thanks to professor Kestutis Staliunas (DONLL) for his exchange of ideas about phononic crystals and providing recommendations and suggestions to enhance the simulation results thanks to his deep experience and knowledge in such a complex field.

The DONLL research group has a very valuable tradition of creating a weekly or bi-weekly meeting to discuss the recent updates of the research work conducted by the group members (professors and PhD

students). These meetings were great to help share ideas between the whole group members, critical thinking and questions, doubts, ideas, recommendations and sharing helped the brain-storming and the discussions after the meetings were really helpful to find solutions to the main problems we face in our research, I would like to thank all the professors and PhD students of the DONLL group that really supported me directly or indirectly to develop the ideas of the thesis research. I want to give special thanks to Jordi Tiana Alsina and Carlos Quintero, the post-doctoral researchers, for their close assistance with programming and algorithm development and finding solutions to programming problems.

I would like also to express my appreciation to Dr. Daniel Zurita and Dr. Fernando Piñal (MCIA) for their assistance with hardware interfacing and computer configuration.

Last, but not least, I am really grateful to my colleagues at UPC and UPV universities, and all of those people on whom I have heavily relied in the process of completing my thesis. In addition, they made the work atmosphere very friendly and passionate that helped relieve the stress and hardness of the work. In addition, the afterwork casual and cheerful activities, sports events, etc… helped make a close connection between us and relax our minds. We had several leisure trips together across Spain. These trips were a very important reason to become great friends together.

I would also give a big credit for my friends at the university as well as friends form outside the university that helped me get connected to the Spanish culture and enhance my level of practicing Spanish language. So, I should thank them for all their help, support, concern and valuable remarks.

Of course, much credit goes to my parents and family members as they have always supported me, no matter what I got myself into. They showed sympathy for my effort and did not complain about my being away most of the time. Being in a different country was difficult on both my family and I, however their support made it easier for me to keep working on my passion of research. They rather waited most patiently, having faith in my ability to meet their great expectations. Therefore, I dedicate this work to my family, without whose support and prayer, this work would not have been completed.

Contents

Chapter 1. Introduction

Embedded structural damage is a typical defect in metallic objects and structures exposed to a defective manufacturing procedure or subjected to a complex and cyclic loading during their service. It is, then, of high importance to be able to detect and characterize these defects, if possible, using non-destructive techniques (NDT) that will not affect the structure. Among various non-destructive evaluation (NDE) and structural health monitoring (SHM) techniques, ultrasound-based approaches have been widely applied in the last decade, in particular for metallic materials inspection [1,2]. These techniques provide useful information for quality control, condition-based maintenance, and preventive measures that are all related to industrial safety, reliability, and quality features [3,4].

The emitter-receiver ultrasound inspection scheme, based on ultrasound transducers, has been classically adopted for damage detection and failure localization as a cost-effective NDE strategy [3–5]. In this technique, one or several transducers generate ultrasound waves that propagates inside the sample. Another transducer, used as receiver, registers the result of the propagation, that brings information about the

internal structure of the sample under test. This quite simple scheme has been largely implemented in industry and give satisfactory results in many particular applications. However, this technique is limited in several aspects. From one side, the increase of resolution is limited by manufacturing technology and transducer size. From the other side, the low output excitation power of the ultrasound transducers prevents such approaches from being used remotely. In this regard, non-contact variants of the ultrasound excitation sources have been investigated in recent years [6,7]. However, the acoustic coupling impedances limit their applicability to use in air at an air gap of few millimeters or to use in water following water immersion procedures or other fluids of interest [8,9]. Finally, typical NDT techniques use contact transducers fixed in a single position on the object's surface. Although in contact mode the received signal has a higher signal to noise ratio (SNR) with higher gain and less attenuation, the mode has an important drawback when the same detector has to be used to scan a certain area. When the detector is moved from one point to another, the coupling factor changes, rendering impossible a quantitative comparison of the two measurements. Moreover, automatic scanning is not possible to be implemented with contact sensors and transducers arrays have to be used when multiple scanning points are required On the contrary, a noncontact transducer can be programmed to automatically scan a larger area, with the drawback of signal attenuation due to the airgap and the weaker sensitivity to detect small variations in the ultrasound signal.

In the last few years advanced sensor designs have been of interest to improve damage detection. For instance, and just as one example, nonlinear technologies have been applied to the design of ultrasound transducer using phononic crystals (PCs). PCs filter out unnecessary second harmonic frequencies and enhance spatial focusing properties enabling detection of nonlinear effects without modifying the acquired signals and allowing one to determine the spatial location of the damage

[10]. Furthermore, another advanced technique uses smart materials to detect damage through the use of arrayed sensors. Integrated thin film paint ultrasonic transducer arrays is used in different aerospace applications thanks to its fabrication novelty and production flexibility [11].

As an alternative to exclusive ultrasound approaches, photonic strategies, based on laser-induced ultrasound and interference laser detection, have been revealed as a powerful remote NDE technique. The electromagnetic radiation carried by the laser excitation pulse is rapidly absorbed into a shallow volume of the metallic material and creates a localized heating effect resulting in a thermo-elastic expansion, finally inducing a stress pulse that generates a multi-component ultrasound wave [12–15]. The detection can be done also using optical technology, such as optical interference or holographic interferometry [16]. For instance, the electronic speckle pattern interference techniques are used in non-contact detection of ultrasonic signals. Mast et al. report that the two-dimensional ultrasonic surface wave data are obtained by optical electronic speckle pattern interferometry (ESPI) techniques [17]. Digital holography can measure phase and amplitude information directly with one hologram. Holography is a technique for recording and reconstructing static or dynamic wavefronts. Holographic interferometry allows the comparison of wavefronts recorded at different time instants and has been used for vibration measurement for many years [16,18]. These all-optical methods considerably increase the resolution and the ability to send and receive signals remotely at intensities and wide frequency ranges that are not achievable by conventional transducers [19–21]. This implies larger penetration of the ultrasound to deeper areas inside the object and the ability to detect deeper embedded defects. These approaches offer the possibility of inspection at higher resolution ratios, even when the power density of the pulsed laser is lower than the ablation threshold of the material under test, i.e. working on the thermo-elastic regime [22]. Although all optical laser-based technologies are nowadays used for crack

detection, the inspection device is highly sensitive to the environmental vibrations, which mostly limits this strategy to laboratory procedures, together the high cost of the device. The system needs to be isolated against surrounding vibrations, making it difficult to implement in practical industrial applications [18]. Due to these drawbacks, some of all-optical NDT methods are only implemented for the detection of defects with micrometer sizes, where the ultrasound-based techniques fail.

In this regard, the hybridization of the laser-ultrasound technique, taking advantage of the optical system for ultrasound wave generation, and conventional ultrasound transducers for detection, is currently being investigated to overcome the drawbacks of the aforementioned approaches. Indeed, this hybrid approach allows ultrasound wave generation by the laser pulse impact at a far distance from the object, enabling remote excitation and scan without the need for a direct contact with the sample. The resulting broad excitation frequency bandwidth covers the majority of the ultrasound bandwidths of interest for available applications involving material characterization. The ultrasound transducers integrated in the structure are used for detection, to detect the received signals [23,24]. Research on such a laser-ultrasound inspection scheme has been done by several authors. For instance, A. Cavuto, et al., used air-coupled ultrasonic probe that detects the ultrasonic waves generated by a high-power pulsed laser to improve the performances of train axle ultrasonic inspection [25]. Levesque D. et al., used laser-ultrasonic technique combined with the synthetic aperture focusing technique (SAFT) on 25 and 50mm thick butt-welded joints of steel both completed and partially welded. Line scans transverse to the weld are performed with the generation and detection laser spots superimposed directly on the surface of the weld bead [26].

Once the signal is detected, it has to be processed and interpreted. Signal processing, usually implemented through contact or noncontact ultrasound techniques, is based on the extraction of the time-of-flight

(*TOF*) corresponding to the reflected echoes generated by the embedded defects and also by the object boundaries. Several algorithms have been proposed, as for example the B-scan [27,28], Fourier-Transform (FT), Short-Time Fourier-Transform (STFT) [29], Wavelet Transform (WT) [30–32], Time Reversal [33], and Synthetic Aperture Focusing Technique (SAFT) algorithms [27,28,34–37]. Each algorithm has advantages and limitations. For instance, the B-scan algorithm, consisting in space-time graphical analysis with color representing the amplitude of the signal's intensity can give time domain and 1D space domain information of the defect by combining multiple A-scan measurements in cascade [27,28]. For example, W. Zeng et al. showed that the presence of damage in the component under inspection can cause a significant increase of amplitude and bandwidth of reflected wave signals. In this regard, the Wigner-Ville transform was proposed for quantization [38]. However, the procedure requires the selection of a specific frequency component to track the propagation of the ultrasound wave and the damage effects. Also, J.-R. Lee et al. presented the study of a laser ultrasound system designed for the damage visualization of a target structure located at a large distance [39]. Although the work showed excellent application feasibility, the study is focused on surface defects. Another significant work is the one proposed by B. Park et al., where the resulting ultrasound waves in the presence of damage, were studied and a correlation strategy among multiple measurements was proposed to enhance characteristic damage effects in ultrasound images [40]. C. Pei et al., studied the interaction process of the laser generated ultrasound with internal defects. He developed a method to characterize defect size based on time of flight (*TOF*) analysis of the scattered waves [41].

Although these procedures show good qualitative information, the damage quantization is limited. The detection and quantization of embedded damages in metallic components is still a challenging field of research in terms of applying suitable signal processing techniques and defect reconstruction methodologies to extract characteristic ultrasound

wave contents and generate reliable defect estimations. In this regard, time-domain analysis represents a set of powerful tools which are applied often for damage detection purposes. If the amplitude of the ultrasound signal events exceeds a certain threshold, they are recorded and characterized. Although these methods are used even for damage localization, their intrinsic limitations restrict them to certain applications such as fault detection, since the coexistence of multiple frequency-modes may mask characteristics patterns for damage reconstruction [42]. Thus, many studies fall into the frequency-domain analysis of ultrasound waves [43]. However, the Fourier transform does not provide information about the evolution over time of each component and its instantaneous strength, which is critical in dealing with ultrasound propagation modes and damage effect characterization. The Fourier transform may even mask the components that appear in a given time instant, but they are of very short duration [44]. In consequence, different time-frequency domain transforms are the most promising techniques to apply for ultrasound signals.

Some authors, such as Y. Zhang et al. [45], studied Empirical Mode Decomposition (EMD) to analyze the ultrasound signals captured from an object that suffers from a certain defect. Afterwards, the Fourier transform was applied over the selected Intrinsic Mode Functions (IMFs). The study exhibits good characterization capabilities, but the number of the resulting IMFs cannot be controlled a priori. Other authors focused their efforts on comparing and clarifying the capabilities of different Cohen's class-based time-frequency distributions [46]. The main drawbacks of these methods are related to time and frequency resolutions and undesirable components called cross-terms, which appear in the time-frequency representation and make interpretation difficult.

In this regard, the wavelet transform is considered a suitable time-frequency technique based on the correlation between the target signal and a shifted set of dilated and compressed versions of a specific wavelet

[47]. The flexibility of choosing the proper mother wavelet is one of the strongest advantages of the WT. The choice of the mother wavelet for a particular problem instead of classical sinus based function, may improve the characteristic pattern identification. and a lead to a dramatic signal-to-noise ratios improvement , which represents a huge potential for ultrasound signal analysis and defect pattern identification [48,49]. Although several studies have exhibited the potential of the WT to analyze ultrasound signals, the analysis and interpretation of the resulting time-frequency maps are still a challenge in the field. In fact, the energy values extracted after the time-frequency calculation are commonly used for a qualitative interpretation (i.e., ultrasound wave arrival time), but they are not further analyzed in order to extract a damage indicator containing the diagnosis information itself. A quantitative damage visualization methodology, as proposed in this thesis, is more challenging.

STFT as well can detect information about both frequency and time with a certain level of uncertainty that is acceptable for various applications. However, WT is more flexible and accurate than STFT due to the fact that the window size in the WT changes with frequency and time, whereas the window size, in the case of STFT, is fixed, which limits the resolution of the algorithm [50].

Moreover, time reversal techniques rely on the principle of detecting the ultrasound wave field using a receiver and transmitting the same wavefield to the source reversed in time, producing a convergence of the signal towards the initial source position. If the source of this signal is a defect, then the convergence of the reversed signal will occur at the defect position allowing its visualization [33].

The SAFT technique relies on the principle of Delay And Sum (DAS) that generates a focused image of the defect out of multiple unfocused images. This focused image has much higher amplitude at the defect

position compared with healthy positions inside the object of interest. The SAFT has the advantage of being able to visualize the whole volume providing 2D or 3D information about the object depending on the resolution and the number of scans performed on the object [27,28,34–37].

An apodization function can be enclosed in the SAFT algorithm in order to enhance the reconstructed image by removing the effect of side lobes. The function can be used in 1D when one performs a line scanning, as described in the literature [51]. Using this approach, a window function is selected to cover the size of the synthetic aperture to filter out the signals detected by the receiving transducer at angles greater than the beamwidth angle. This signal conditioning removes the effect of side and redundant echoes that are not generated by the main lobe of the incident signal. The beamwidth angle depends on the frequency passband, the size of the transducer and the wave velocity. When the scanning is performed in 2D (i.e., a scan area), the apodization window is extended from a line to an area since the beamwidth angle is extended to become a solid angle [28,34,51,52]. The size of the synthetic aperture changes with the depth of the scattering point. Therefore, the size of the apodization function should be adjusted accordingly to cover the synthetic aperture area. A drawback of apodization is the possible change of the main lobe width, which affects the lateral resolution [28,34,51,52]. Hence, good selection of the apodization function and its width help optimize results with minimum lateral resolution deficiency. Rectangular and Hanning apodization functions are commonly used in the SAFT analysis.

Other advanced signal processing algorithms are also used to detect defects by analyzing echoes received by guided waves that travel long distances without substantial attenuation in irregular-shaped waveguides. Any perturbation in the detected signal represents a defect. Signal processing is applied by exploiting dispersion compensation properties of a warped frequency transform (WFT) [53]. In addition, other techniques using nonlinear contact dynamics have shown interesting

results for detecting defects inside materials using resonance and non-resonance vibrations [54]. Nonlinear elastic wave spectroscopy combined with the elastic energy localization of the time reversal mirror can isolate surfacial nonlinear scatterers in solids [55]. Combining Time reversal and laser vibrometry made it possible to locate an impact event by applying a correlation of the measured impact response and a set of measured test data acquired at various grid points along the specimen surface [56].

In the next sections we are going to discuss a short theoretical background about the nature of ultrasound waves and their propagation in solid materials for the purpose of NDT applications. Moreover, a description of laser generated ultrasound waves is presented to familiarize the reader with this kind of propagation. In addition, a short discussion about the main signal processing techniques used in the present thesis is included.

1.1. Ultrasound wave propagation in different media

Ultrasound waves are acoustic waves with a frequency above 20kHz. They can propagate through a medium as stress or strain waves depending upon the elastic properties of medium. Based on particle displacement of the media, most important ultrasound waves are [57,58]:

(i) **Longitudinal or compressional or pressure ultrasound waves.**

In the longitudinal waves particles of medium vibrate back and forth parallel to the direction of propagation of wave. These waves, typical for the sound propagation in fluids, propagate through the medium as a series of alternate compression and rarefaction. These waves are most widely used in the ultrasound inspection of materials. This mode is exhibited when medium of propagation has no boundaries i.e. it has

infinite span. Due to propagation of these waves both pressure and density of medium fluctuate periodically.

(ii) **Transverse or shear ultrasound waves.**

In the transverse waves particles of the medium vibrate perpendicular to the direction of waves propagation. In this case the medium undergoes shear deformations periodically.

(iii) **Surface or Rayleigh waves.**

The surface waves travel along the flat or curved surface of thick solids without influencing the bulk of medium below the surface. The depth to which these waves propagate below the surface with considerable intensity is approximately equal to wavelength of the wave. Practically all of its energy is attenuated within this depth. These waves are used to detect cracks or flaws on or near the surface of test objects. During the propagation of surface waves, the particles of medium describe elliptical orbits.

(iv) **Lamb or Flexural or Plate Waves.**

The lamb waves are produced in thin metal, whose thickness is comparable to the wavelength of ultrasound wave.

Ultrasound waves go through different propagation patterns depending on the acoustic properties of the corresponding media whether it is solid or fluid. liquids are very compressible unlike solid materials. Hence, we use the acoustic pressure and the compressibility as parameters proportional to the propagation effect of ultrasound waves in liquids. On the other hand, the stress and the elastic constants are the appropriate parameters when propagating in solids. Another important consideration is that liquids can change shape to match its container. Hence, a fluid cannot support shear waves and only longitudinal waves

can propagate in fluids. However, in solids it is essential to consider longitudinal and transverse waves to give a full description. Additionally, in liquids the pressure is a scalar and acts uniformly on a volume element, while in solids one can have a unidirectional compression or tension.

1.1.1. Ultrasound propagation in solid material

Let's consider an element of solid material of length l that suffers elongation due to the application of an external force F in the positive X direction acting on a surface area A_s, The external stress is $T = \frac{F}{A_s}$, so the net stress on the element is $\partial T = l\frac{\partial T}{\partial x}$. Hence, the strain can be defined as [57]:

$$S = \frac{\partial u}{l} = \frac{\partial u}{\partial x} \qquad \textbf{1-1}$$

According to Hooke's law, $T = cS$ where c is a constant. Considering Newton's law:

$$\frac{\partial T}{\partial x} = \rho \ddot{u} \qquad \textbf{1-2}$$

Hence substituting equation 1-1 into equation 1-2, the wave equation can be written as:

$$\frac{\partial^2 u}{\partial x^2} = \frac{\rho_0}{c}\frac{\partial^2 u}{\partial t^2} \qquad \textbf{1-3}$$

where ρ_0 is the equilibrium state density. We will focus on the solutions for the displacement $u(x, t)$. These can be written as:

$$u = A.e^{j(\omega t-\beta x)} + B.e^{j(\omega t+\beta x)} \quad \textbf{1-4}$$

where A, B are displacement amplitudes. $A.e^{j(\omega t-\beta x)}$ corresponds to the forward propagation in the direction (+x) and $B.e^{j(\omega t+\beta x)}$ corresponds to the backward propagation in direction (-x). wave number $\beta = \omega / V_L$ where $V_L = \sqrt{c / \rho_0}$ is the wave velocity.

Three-dimensional wave equation for solids has solutions that are pure longitudinal and pure shear waves. The two equations are decoupled, which has the consequence that longitudinal and shear waves are independent modes of propagation in bulk solids [57].

Since perfect fluid does not have any shear stress, the wave propagation analysis in a perfect fluid medium is much simpler and can be considered as a special case of that in the solid [57].

1.1.2. Media impedance

The amplitude reflection coefficient R at the interface between two media is given by [57–59]:

$$R = \frac{Z_2 - Z_1}{Z_2 + Z_1} \quad \textbf{1-5}$$

where Z_1 and Z_2 are the characteristic acoustic impedances in media *1* and *2* respectively and their unit of measurement is *rayl*. The relationship between reflected and total intensities is:

$$\frac{I_{reflect}}{I_{Total}} = R^2 \quad \textbf{1-6}$$

and the transmitted intensity is

$$I_{transmit} = I_{total} - I_{reflect} \quad \textbf{1-7}$$

The analysis is performed assuming that the incident wave is moving from medium *1* and partially transmitted into medium *2*. If $Z_2 = Z_1$, the reflection coefficient is zero; it is as if the wave continued traveling forward in a single medium. On the other hand, if $Z_2 >> Z_1$ then $R < 1$, i.e., the wave is almost totally reflected [57–59].

1.1.3. Mode conversion

When sound travels in a solid material, one form of wave energy can be transformed into another form. For example, when a longitudinal wave hits an interface at an angle, some of the energy can cause particle movement in the transverse direction to start a shear wave. Mode conversion occurs when a wave encounters an interface between materials of different acoustic impedances and the incident angle is not normal to the interface. It should be noted that mode conversion occurs every time a wave encounters an interface at an angle. This mode conversion occurs for both the portion of the wave that passes through the interface and the portion that reflects off the interface [57–59].

Ultrasound attenuation α in isotropic solids is a difficult parameter to specify in absolute terms, yet it is very important. Sources of attenuation can be divided into two classes: intrinsic (e.g. thermal effects, elementary excitations) and those due to imperfections (e.g. impurities, grain boundaries, dislocations, cracks, etc.).

The amplitude change of a decaying plane wave can be expressed as:

$$A = A_0 e^{-\alpha l} \quad \textbf{1-8}$$

Where A is the final amplitude of the ultrasound wave in the material after travelling a distance l and suffering an attenuation coefficient α, *while* A_o is the initial amplitude at the source. In addition, the viscous forces of the media of propagation increases the attenuation of the propagating waves with increased frequencies. In vacuum, there is no attenuation of ultrasound at high frequencies due to the heat loss due to molecules' collisions.

As a general concept, elastic waves in an infinite elastic solid can propagate in two different modes: P-wave (longitudinal waves) mode and S-wave (transverse waves) mode. When an elastic wave propagates as the P-wave, then only normal stresses (compressional or dilatational) are generated in the solid, and the wave propagation speed is:

$$c_p = \sqrt{\frac{\lambda + 2\mu}{\rho}} \qquad \text{1-9}$$

where ρ is the mass density and coefficients λ and μ are known as Lame's first and second constants, μ also is known as shear modulus. When the elastic wave propagates as the S-wave, then only shear stresses are generated in the solid, and the propagation speed is:

$$c_s = \sqrt{\mu / \rho} \qquad \text{1-10}$$

Considering the wave numbers for P-wave and S-wave as k_p and k_s respectively, we can write them as:

$$k_p = \frac{\omega}{c_p} \qquad \text{1-11}$$

$$k_s = \frac{\omega}{c_s} \tag{1-12}$$

ω is known as the angular frequency (radian/s) and is related to the wave frequency (Hz) as:

$$\omega = 2\pi f \tag{1-13}$$

1.1.4. Phase and group velocity

The phase velocity c_{ph} is the velocity of the individual waves inside a wave packet, whereas the group velocity (c_g) is the velocity of the whole envelope of the wave packet. Different phase velocities in a wave packet means that there is a wave dispersion that causes individual wave frequencies to propagate at different velocities [57–59].

$$c_{ph} = \frac{\omega}{k} \tag{1-14}$$

$$c_g = \frac{d\omega}{dk} \tag{1-15}$$

where c_{ph} is phase velocity and c_g is the group velocity.

1.1.5. Piston source radiation and side lobes

Spherical waves are generated by a point source in an infinite medium, the cylindrical waves are generated by a line source, while an infinite plane generates plane waves, as shown in Figure 1-1 [57].

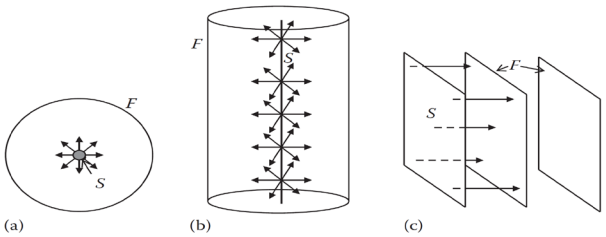

Figure 1-1: a) Point source b) line source, and c) infinite plane source generating spherical, cylindrical, and plane wave fronts, respectively. Sources are denoted by S and the wave fronts by F [57].

The field due to a finite plane source can be assumed to be the summation of fields generated by a number of point sources distributed over the finite source. The combined effect of a large number of point sources distributed on a plane surface is the vibration of the particles in the direction normal to the plane surface because non-normal components of motion of neighboring source points cancel one another. However, non-normal components do not vanish along the edge of the surface. As a result, the particles on the edge not only vibrate normal to the surface but also expand to a hemisphere and contract back to the point. If this edge effect does not have a strong contribution on the total motion, then the normal vibration of a finite plane surface can be approximately modeled by replacing the finite surface by a large number of point sources distributed over the surface. In our analysis in this thesis, we will mainly consider the point source excitation since we use LGU which is a very fine point source for generating ultrasound waves.

The size of the source and the wavelength of the propagating waves influence the wave shape. An ideal ultrasound wave would have only the main lobe that contains all the wave energy. However, in a practical experimental analysis, other sidelobes are present on either side of the main lobe as shown in Figure 1-2.

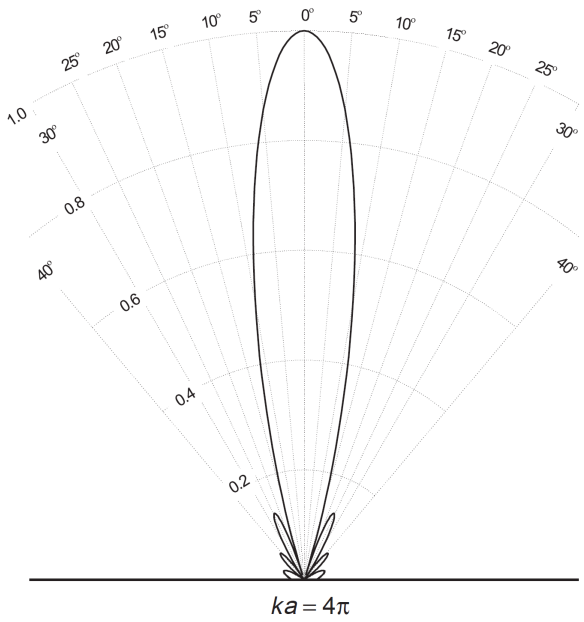

Figure 1-2: side lobe effect on the propagating ultrasound wave. Main lobe in the center, and side lobes on the side [57].

These sidelobes are undesirable for two reasons. The main objective of an acoustic radiator is to produce a narrow-collimated beam of acoustic energy to be used in some application, for example, imaging or nondestructive testing. The sidelobes represent energy lost from the main beam, which is of course undesirable. If the sidelobes are big enough, they can interfere with information obtained from the main beam, which is also unwanted. Hence, an important part of the design of acoustic radiators involves sidelobe reduction. A practical consideration to reduce these side lobes is by considering the value of the multiplication product "k.a". Where k is the wavenumber of the propagating wave, and a is the radius of the circular radiator. Considering far field propagation, it is found that for $ka >> 1$, there are many sidelobes. As ka decreases, the number is reduced and for $ka << 1$ there is really only the main lobe.

1.2. Laser generated ultrasound

Ultrasound waves can be generated by different approaches. In the most general case, acoustic waves are generated by means of material vibration (naturally or by other mechanical source, as for example electrically driven membranes or motor driven machine, etc…). Piezo-electric transducers convert electric signal into mechanical vibration of the active piezo-electric element (membrane) generating ultrasound waves. These transducers work on both directions, i.e, they convert electric signals into ultrasound and vice versa. Depending on their design, transducers can work in contact mode or non-contact mode and they can have narrow frequency band or wide frequency band.

Another approach to generate ultrasound waves is by using laser pulses impact onto a solid material. In Laser Generated Ultrasound (LGU) analysis, the laser is used as the exciter of ultrasound waves when the laser pulse hits the target object's surface. The energy carried by the laser pulse is rapidly absorbed into a shallow volume of the material, and creates a localized heating which results in a thermo-elastic expansion of the material, inducing a stress wave that generates an acoustic pulse [12–15].

Once the ultrasound is generated in thermo-elastic or ablation regimes, its directivity pattern is broad and wave energy is spread at different angles inside the material in which it propagates. As important advantages, with respect to the classical transducer-induced ultrasound, LGU has a more flexible and accurate targeting of the excitation, it is broadband in frequency, it is noncontact and can be

remotely controlled. However, LGU directivity is difficult to control as it depends on many factors such as the intensity of the laser pulse, the wavelength, the interaction regime and the material [12–15].

Figure 1-3 shows the directivity pattern of the LGU in both thermo-elastic and ablation regimes. Figure 1-4 shows the directivity pattern in thermo-elastic regime for both longitudinal and transverse waves at various frequencies and laser-spot sizes. Figure 1-5 shows the directivity patterns in thermo-elastic regime in aluminum at different detecting frequencies for both longitudinal and transverse waves.

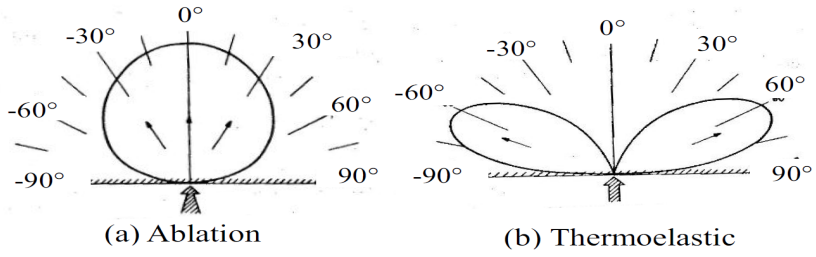

Figure 1-3: Directivity of longitudinal waves of Laser generated ultrasound in a) Ablation regime b) thermos-elastic regime.[12]

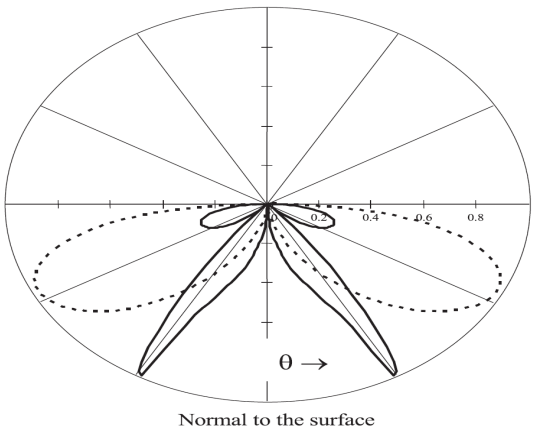

Figure 1-4: Directivity patterns at thermo-elastic regime for a pair of horizontal forces applied to the surface: dashed curve corresponds to bulk longitudinal waves, and solid curve indicates shear waves.[13]

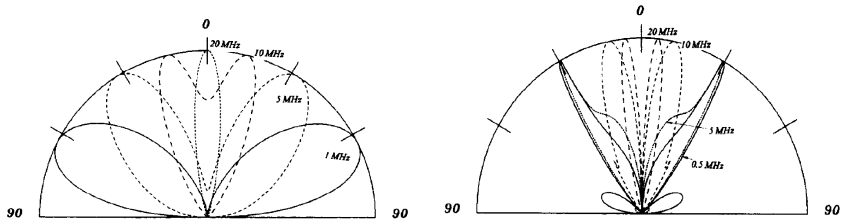

a) b)

Figure 1-5: : The theoretical predictions of the directivity patterns at thermo-elastic regime in aluminum at four detecting frequencies: (i)1 MHz, (ii) 5 MHz, (iii) 10 MHz, and (iv) 20 MHz, while the Gaussian beam radius is I mm, for a) longitudinal wave propagation b) transverse wave propagation.[14]

Figure 1-6 show their directivity patterns at different laser spot sizes for transverse waves.

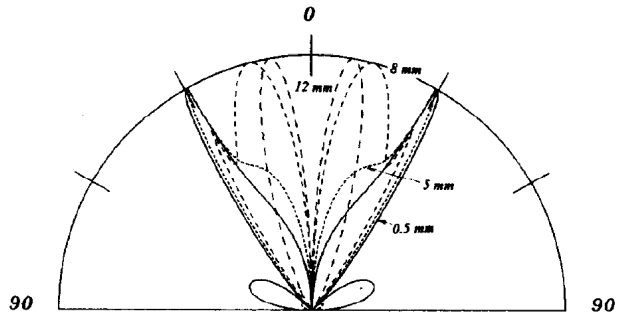

Figure 1-6: Transverse wave propagation, spot sizes: 0.5, 5, 8, 12mm [14].

Figure 1-7 shows the broadband frequency spectrum of the LGU. A broadband covering large spectrum is recognized in comparison to

conventional ultrasound transducers which allows for detection by various optical/ acoustic measurement techniques.

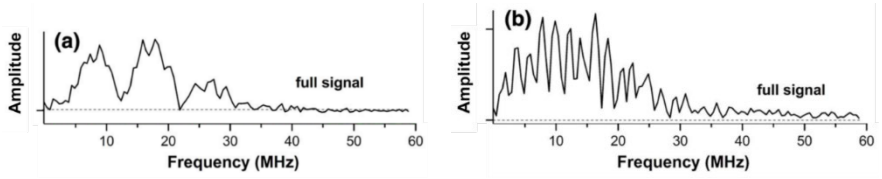

a) b)

Figure 1-7: Laser Generated Ultrasound frequency spectrum for a) Transmission detection transducer b) reflection detection transducer.[15]

1.3. Non-Destructive Testing using ultrasound waves

As discussed earlier, a typical hybrid NDT setup uses a pulsed laser as excitation source producing ultrasound waves in the target object and one or several ultrasound transducers which detect the reflected/scattered ultrasound waves. A proof of principle set-up is shown in Figure 1-8. In ultrasound testing of solids, diffraction patterns are usually generated at the edges of sharp reflectors (or discontinuities) such as cracks. Usually the tip of a crack behaves as point source spreading waves in all directions due to the diffraction of the incident wave. This phenomenon is used to detect the presence of cracks inside materials under test. It is difficult to get enough information about this crack with only one ultrasound transmit/receive measurement. Hence, different measurements done by scanning over a certain object area would provide more accurate information about the size, position and location of the defect. By calculating the *TOF* of the echoes diffracted from the defects at the various scan points, one can extract the crack position. Different types of scan can be performed on the material, the most typical ones being the

A-scan, B-scan and C-scan that are going to be described briefly here [57,58,60].

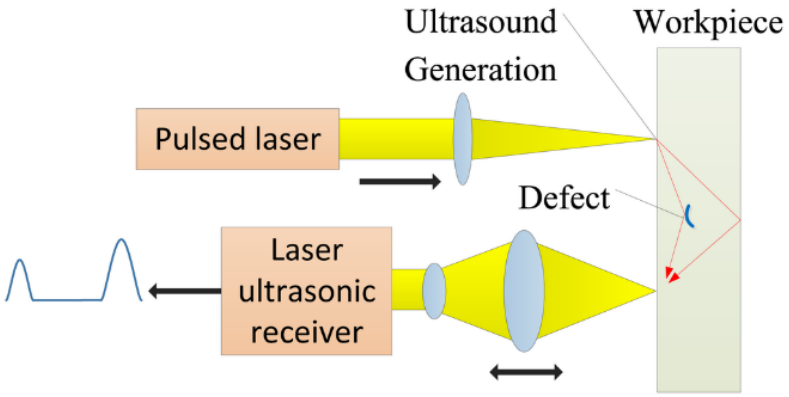

Figure 1-8: Schematic of using Pulsed laser as an excite of ultrasound wave and ultrasonic transducer as a detector [24].

The A-scan presentation is obtained by the record of signal intensity (acquired as a voltage signal by the detector) as a function of time. It is a single capture measurement for one excitation and one detection. In the A-scan representation, relative discontinuity size can be estimated by comparing the signal amplitude obtained from an unknown reflector to that from a known reflector. Reflector depth can be determined by the position of the signal on the horizontal time axis and calculating the distance from the *TOF*.

The B-scan is obtained by a cascaded plot of several A-scan measurements performed by scanning the ultrasound transducer across a scan line with defined step displacements. The representation of the results of the automated linear scanning systems shows a profile (cross-sectional) view of the test specimen. A color map is used to define the amplitude information for each scan position. It provides more information than the A-scan since multiple measurements provide more data of the possible defect reflector inside the material from different positions which give information about defect size.

Finally, a C-scan has both horizontal and vertical axes represent the 2D area of an ultrasound scanning process. The data presented provides information about the 2D positions of the defect at specific *TOF*. Figure 1-9 shows the difference between the three scan modes.

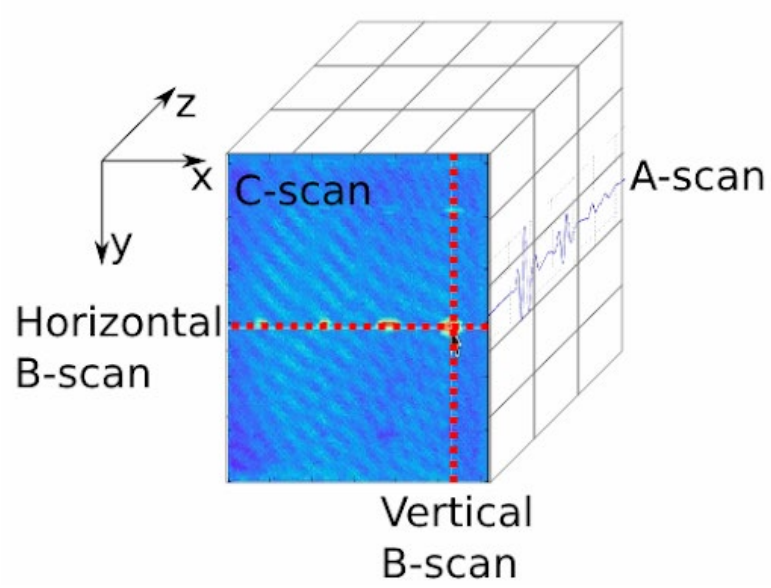

Figure 1-9: Graphical representation of A-scan, B-scan and C-scan analysis [61].

1.4. Signal processing analysis

The results acquired from the scan measurements described in the previous section generate an important amount of raw data that need to be further processed in order to interpret it into useful information about the cracks and discontinuities. Different types of signal processing algorithms are used in literature including analysis, SAFT, time-reversal techniques and synchro-squeezing techniques. We focus on our study on the WT and SAFT analysis and further related signal processing techniques that are described below. These two algorithms are mainly chosen for our research thanks to their flexibility and the enhanced quantitative and qualitative signal to noise ratios and ability to detect

information about embedded defects in time and frequency domains with enhanced results as will be shown in the following sections.

1.4.1. Wavelet Transform mathematics

The WT is a method that converts a function (or signal) into another form which either makes certain features of the original signal more amenable to study or enables the original data set to be described more succinctly. To perform a wavelet transform, we need a wavelet which, as the name suggests, is a localized waveform. In fact, a wavelet is a function, ψ(t), which satisfies certain mathematical criteria. These functions are manipulated through a process of translation (i.e. movements along the time axis) and dilation (i.e. the spreading out of the wavelet) to transform the signal into another form which 'unfolds' in time and scale [48,62–65]. There are, in fact, a large number of wavelets to choose from for use in the analysis of data. The best one for a particular application depends on both the nature of the signal and what we require from the analysis (i.e. what physical phenomena or process we are looking to interrogate, or how we are trying to manipulate the signal) [48,62–64]. Figure 1-10 shows a variety of different famous mother wavelets.

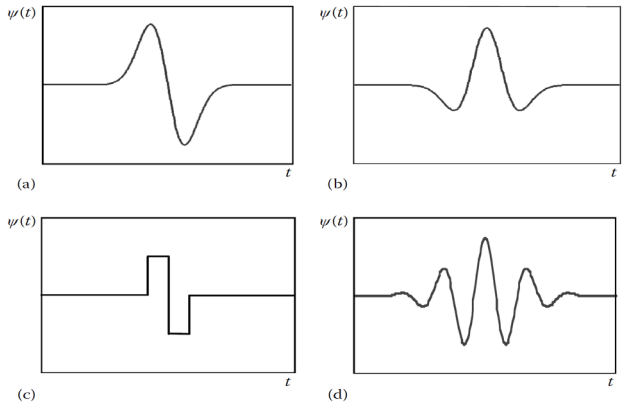

Figure 1-10: Four wavelets: a) Gaussian wavelet (first derivative of a Gaussian), b) Mexican hat (second derivative of a Gaussian), c) Haar, and d) Morlet (real part).

The wavelet transform (WT) of a time series function $x(t)$ can be represented as:

$$x_{\omega}(a,b) = \frac{1}{\sqrt{|a|}} \int_{-\infty}^{\infty} x(t) \psi^{*}(\frac{t-b}{a}) dt \qquad \textbf{1-16}$$

where x_{ω} is the resulting wavelet analysis, ψ^{*} is the complex conjugation of the mother wavelet that has to be a continuous function in both time and frequency domains, a is a scale factor that either stretches (large a) or compresses (small a) the wavelet and, b is the signal's shifting parameter in time.

The above-mentioned formula represents the continuous WT, where our time and frequency signals are continuous, and the analysis in this thesis will be considering this type of WT. Another type of WT is applied to discrete wave functions and the resulting transform is a discrete WT which we are not going to discuss here as it is not part of the next analysis.

The wavelet transform is different from another famous transform called Short Time Fourier Transform (STFT) [48,62–65]. The main difference is that the window size in STFT is fixed, whereas in the WT the window size (a) is changing. STFT sometimes is called the windowed Fourier transform since it is similar to the Fourier transform (FT) except for the fact that the window size in FT is infinity [64,65].

The equation governing the FT is as follows:

$$F_{\omega} = \int_{-\infty}^{\infty} x(t) e^{-i\omega t} dt \qquad \textbf{1-17}$$

Equation 1-18 shows the STFT conversion:

$$F_{\omega}(b) = \int_{-\infty}^{\infty} x(t) h(t-b) e^{-i\omega t} dt \qquad \textbf{1-18}$$

where $h(t-b)$ is the window function that confines the analysed signal. It can be shown that FT gives only frequency information while it loses all information about time. This makes the analysis in frequency domain ambiguous about the time instants where certain frequency components where with specific amplitudes.

STFT solves this problem by providing information about time and frequency components at the same spectrum. However, having a fixed size window makes it difficult to detect oscillations and harmonics happening at a resolution higher or lower than the specified window size. In other words, although a narrow-width window results in a better resolution in the time domain, it generates a poor resolution in the frequency domain, and vice versa.

WT solves this problem because it changes the window size at different frequency scales leading to covering higher resolution range in both time and frequency than in the case of STFT. However, it has to be emphasized that according to Heisenberg uncertainty principle, that it is not possible to get accurate and exact information about both Time and frequency at the same time, i.e: when the information about time are more accurate, you lose information about frequency components and vice versa. Depending on the application, we can accept or refuse the results according to our experimental needs.

1.4.2. Clustering mathematics

Dealing with large data requires some statistical and mathematical techniques to sort and filter the data based on their size, neighborhood, repetition, etc… In this thesis study, the data collected from WT analysis was large enough and for the purpose of further signal processing we needed some sort of clustering to reject the data of no interest and keep only those that help in identifying our defect positions.

Cluster analysis groups data objects based on the information that describes the relationship among data members. The goal is to group data of similar criteria together in separate groups. The greater the similarity within a group and difference with other groups makes the clustering process more efficient [66–68].

There are lots of clustering techniques to achieve this goal. Here we are going to represent only two famous techniques that are called K-means and DB scan. Those two techniques are classical and very well known in the literature.

- **K-means**

k-means clustering, or Lloyd's algorithm, is an iterative, data-partitioning algorithm that assigns n observations to exactly one of k clusters defined by centroids, where k, the number of clusters desired, is chosen before the algorithm starts. Each point is then assigned to the closest centroid. Each group of points assigned to the same centroid belong to the same cluster. The iterative process is repeated several times until all points have been assigned to a cluster and they no longer change their mother clusters [66–68].

This technique is very useful, when the programmer already has an idea how many clusters he expects. However, if the chosen number of clusters was far from the desired application, the formed clusters are going to be misleading. An example of that problem if some programmer tried to group the earth landscapes into clustered continents using K-means algorithm. If the programmer decides to have only 4 clusters instead of 7 clusters, this would result in grouping Africa, Asia, and Europe in one cluster (continent) which is not the case. So accurate selection of the value of k is required for better results.

- **DB-scan**

It is an abbreviation to "Density based clustering scan". In this algorithm the user does not select the number of clusters. It is already generated based on the minimum number of points (*MinPts*) required for each cluster and the size of the cluster by considering a specified distance parameter (*Eps*) [66–70].

The algorithm simply considers a point as a core point if the number of surrounding points within the minimum distance neighborhood exceeds the pre-determined threshold. A border point is not a core point but falls within the neighborhood. A noise point is a point that is neither a core point nor a border point.

This algorithm is very effective, but also could be misleading if the parameters MinPts and Eps are not selected accurately. A clear vision of the programmer and fine tuning is required to achieve good results with this algorithm.

The selection of clustering technique depends on the target application and background of the programmer for using an appropriate algorithm that matches with his goals.

In our WT analysis presented later in the next chapters, we will be using the DB-scan clustering algorithm to segregate data into groups based on their density within specific area.

1.4.3. SAFT analysis

The synthetic aperture method is based on the concept of collecting data from a scanned transducer and then processing that data, so as to simulate a larger transducer with much better resolution and S/N ratio. The argument is based on the idea that the more often the discontinuity is seen by the transducer, the more information that can be gathered

about it. The more the information that is known, the more precisely the discontinuity can be located. Thus, a highly divergent beam is used to keep a discontinuity in view over as large an aperture as possible. When the transducer is located directly above the discontinuity, the time delay to receive the defect echo is minimum and as the transducer moves away from this position, the time delay increases in a non-linear fashion. The curve defined by tracing the peak amplitude (in each aperture element) as the transducer moves parallel to the surface is a function of the speed of the sound in the material and the geometry of the transducer and the target [27,28,34–37].

Synthetic aperture processing involves collection of aperture elements to be processed as a unit to introduce a time shift to each individual A-scans, to sum these individual aperture elements point by point across their length and then to place the result at the centre of the chosen aperture. The process is shown schematically Figure 1-11 (the aperture is chosen to be of seven aperture elements wide). If the aperture is centred over the target, as in the case of Figure 1-11, then the shift and sum operation will produce a strong signal (constructive interference). If the aperture is located off center of the target as in Figure 1-12, then the shift and sum operation will produce a weak signal (destructive interference) [71].

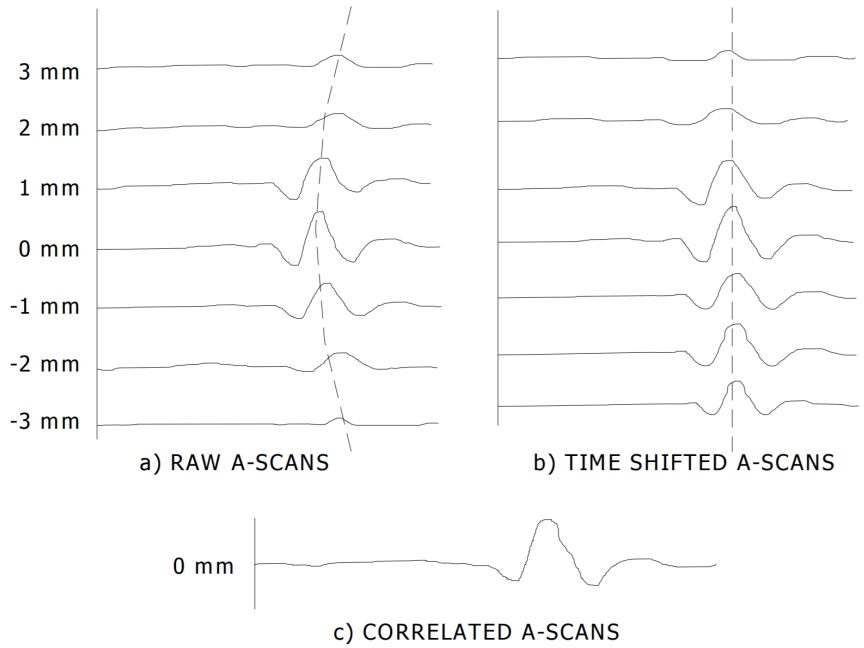

Figure 1-11: Interference of a) raw A-scan data after being b) shifted in time using *TOF* offset shifts, resulting in c) constructive interference because of the high correlation between A-scan signals[71].

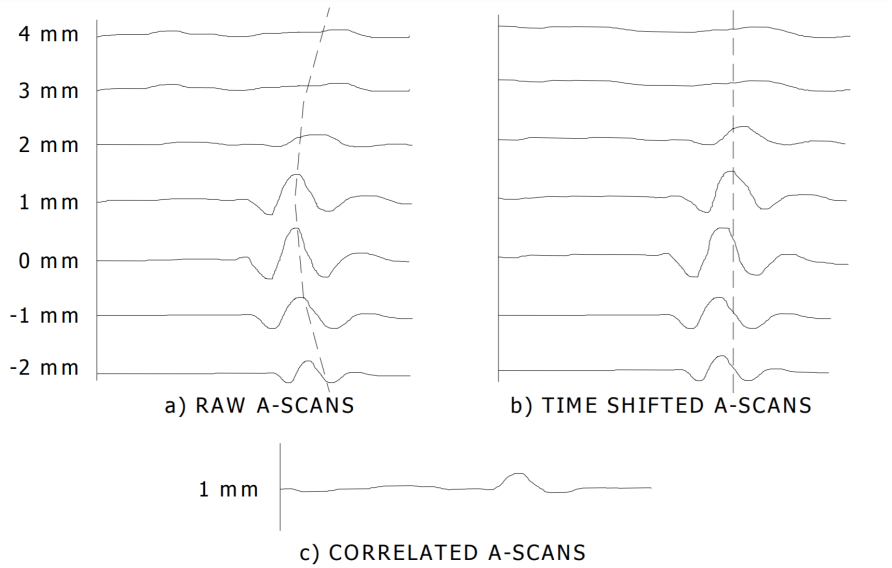

Figure 1-12: Interference of a) raw A-scan data after being b) shifted in time using *TOF* offset shifts, resulting in c) destructive interference because of the low correlation between A-scan signals[71].

Reflections coming from defect are constructively added and other signals such as grain noise and electronic noise are destructively summed, resulting in good S/N ratio for the defect (5). Since simultaneous focusing is obtained along the entire depth of the test specimen, better accuracy is expected (6). SAFT 3 relies less on amplitude information but more on time-of-flight information. Loss of amplitude influences only the S/N ratio in the image. The data acquisition in SAFT is based upon the complete high-frequency ultrasound signal, without time gate or amplitude threshold. Due to the time corrected signal averaging capability of SAFT, signals which are buried within the noise can rise be brought to amplitudes above the noise (7).

The following assumptions need to be followed to have successful results with SAFT analysis:

- **Point source**: The radiation source is assumed to behave like a point source producing spherical waves. Therefore, the diffraction effects of the transducer are neglected in the image reconstruction.
- **A constant speed of sound**: It is assumed that the medium of propagation is homogeneous, non-dispersive, and non-attenuating. As a result, the speed of sound is kept constant throughout the calculations in SAFT.
- **Isotropic scattering**: It is assumed that the scatterers in the ROI scatter the wave isotropically and the reflectivity coefficient of scatterers is assumed to be frequency independent.

For an arbitrary excitation point, T, that generates an ultrasound wave propagating in the volume and an arbitrary receiver, R, which detects the reflected signal by the volume points, one of which is the point

of interest, P as shown in Figure 1-13, we can define the TOF of the signal as [27,28,34–37]

$$TOF_{(i,j,k)P} = \frac{|\vec{d}_{(i,j,k)P} - \vec{d}_{(i,j,z)T}| + |\vec{d}_{(i,j,k)P} - \vec{d}_{(i,j,z)R}|}{c} \quad \text{1-19}$$

where the TOF is the time-of-flight of the ultrasound signal generated by the exciter T, scattered from the point P and detected by the receiver R; $\vec{d}$ is the displacement vector at positions T, R, and P, respectively; i, j, and k represent the indexes of the volume image points in the X, Y, and Z planes respectively; and c denotes the longitudinal speed of sound in the material of the object.

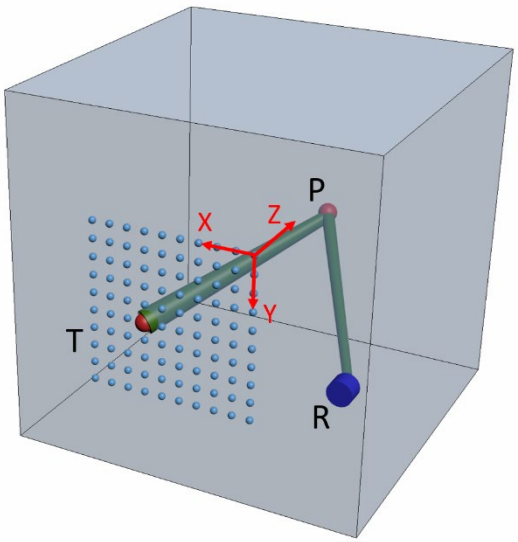

Figure 1-13: SAFT scanning configuration over a volume of an object.

Shifting the position of the exciter/receiver results in a different TOF for the same particular scatterer in the active volume and a different amplitude at the corresponding time instant at the A-scan signal. The summation of all these amplitudes with respect to their $TOFs$ will

generate a focused image, $y_f(p)$, of that scatter with an overall amplitude corresponding to all scan points in the 2D scan area.

$$y_f(P) = \sum_{j=1}^{N} \sum_{i=1}^{M} y_r(TOF_{(i,j,k)_P}, i, j) \qquad \textbf{1-20}$$

where y_r is a preliminary unfocused image of this particular point P; y_f is the high-resolution focused image; and M*N are total scan points in horizontal and vertical directions of the scan area. We note that Equation 1-20 does not take into account the nature of propagating ultrasound in the solid object, which mostly contains main and side lobes at different angles and intensities.

The above-mentioned discussion referred to the standard SAFT algorithm methodology. In our approach we propose the use of the apodization function to enhance the resulting image by weighing the amplitudes resulting from the propagation of side lobes that can produce secondary echoes that influence and distort the main echoes generated by the scatterers (Equation 1-21).

$$y_f(P) = \sum_{j=1}^{N} \sum_{i=1}^{M} a(TOF_{(i,j)_P}, i, j) * y_r(TOF_{(i,j,k)_P}, i, j) \qquad \text{1-21}$$

where $a(TOF_{(i,j,k)_p}, i, j)$ is the weighing or apodization function [36]. we use the apodization window filtering technique, applied along with the synthetic aperture focusing algorithm, to remove the undesired effects due to side lobes and wide-angle reflections of propagating ultrasound waves.

1.4.4. Apodization mathematics

Apodization is often applied in time-domain synthetic aperture focusing to reduce the effect of sidelobe artifacts in the focused image. The synthetic aperture is usually weighted with a function approaching zero at the edges. Since the size of the synthetic aperture increases with the distance from the transducer, the width of the apodization function should be adjusted accordingly [28,34,51,52].

For a 1D scan line X-axis and point scatterers in a plane XZ the width of the synthetic aperture at z is given by:

$$\Delta X(Z) = 2Z\tan(\Delta\theta_X / 2) \qquad \textbf{1-22}$$

Where $\Delta X(Z)$ is the width of the apodization window, Z is the depth of the point scatter, and $\Delta\theta$ is the angular beam width of the transducer. The apodization function can be applied to all points falling within a certain normalized X coordinate, $\hat{X}$, and neglecting all other measurements outside this threshold. The apodization function can be adjusted to the synthetic aperture by using normalized X coordinates.

$$\hat{X} = \frac{X - X'}{\Delta X(Z)} \qquad \textbf{1-23}$$

where X–X' is the horizontal shift between the position of the scan point and scatterer. Figure 1-14 shows the effect of depth of the scatterer point on the beam angle depth [28,34].

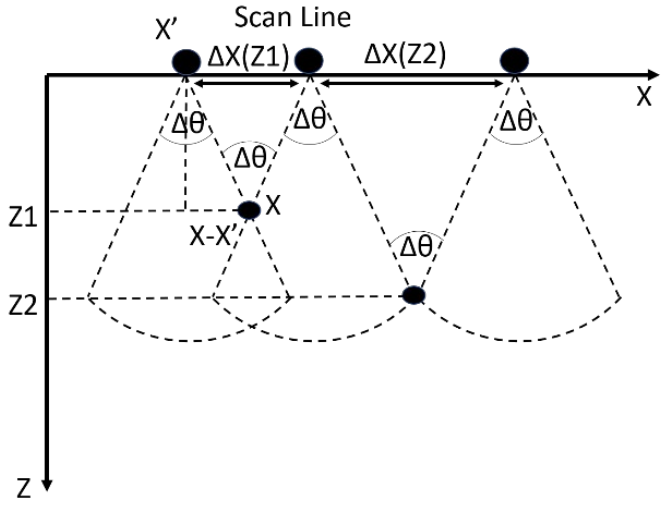

Figure 1-14: Beamwidth angle $\Delta\theta$ for a point scatterer at depth *Z;* when the point scatterer is deeper *Z2 > Z1,* the synthetic aperture size (ΔX) changes accordingly. The apodization window size should be adapted to the synthetic aperture window size.

Different apodization functions can be used for the purpose to weight the main SAFT function as follows:

$$a(\hat{X}) = \begin{cases} F(\hat{X}), & \left|\hat{X}\right| < \alpha \\ 0, & otherwise \end{cases} \qquad \textbf{1-24}$$

Where $a(\hat{X})$ is the apodization function, the selected window function $F(\hat{X})$, α is the threshold criterion. Different window functions can be used for this purpose depending on the application of interest, either one-dimensional, two-dimensional or higher order window functions can be used depending on geometry and application. Here in Table 1-1 is listed some of the most common one-dimensional window functions for filters in signal and image processing studies. The selection of threshold criterion "a" defines the width of the window.

Window	Function	Threshold criterion
Rectangular	$W(x)=\begin{cases}1\\0\end{cases}$	$\begin{cases}\lvert x\rvert \le a\\ otherwise\end{cases}$
Cosine	$W(x)=\begin{cases}\cos\frac{\pi}{2a}x\\0\end{cases}$	
Hann	$W(x)=\begin{cases}0.5(1+\cos\frac{\pi}{a}x)\\0\end{cases}$	
Hamming	$W(x)=\begin{cases}0.54+0.46\cos\frac{\pi}{a}x\\0\end{cases}$	
Blackman	$W(x)=\begin{cases}0.42+0.5\cos\frac{\pi}{2}x+0.08\cos\frac{\pi}{a}x\\0\end{cases}$	

Table 1-1: Common one-dimensional window functions [52].

The two-dimensional window functions presented here have been a direct extension of corresponding one-dimensional window functions. The two-dimensional window function is formed from a one-dimensional separable and circularly symmetric window function, using the relation $w_2(x,y)=w(\sqrt{x^2+y^2}$. This obviously rotates the one-dimensional function about the origin in the x-y plane [28,34,51,52].

In case of a two-dimensional window, the one-dimensional function $W(x)$ is modified to be $W(r)$ where $r = \sqrt{x^2 + y^2}$ and y is the second orthogonal cartesian dimension. The threshold criterion as well changes to be $\begin{cases} |r| \le a \\ otherwise \end{cases}$ for both cases of the window functions.

while one dimensional and two-dimensional windows can be simply related to one another in the time domain, no direct, general parallels exist to relate their transforms in the frequency domain.

1.5. Phononic crystals as ultrasound lens

After a detailed study of the ultrasound waves propagation of for NDT applications, we found that once the ultrasound is generated in the target material, its directivity pattern is broad and wave energy is spread at large angles inside the material in which it propagates. The ability to direct the ultrasound waves at certain angles, for instance far from boundaries or to propagate in a direct path towards the receiving transducer would be a good enhancement to the performance of non-destructive testing. The recorded signal would be potentially easier to interpret thanks to the removal of the interfering scattered and reflected components from boundaries. This issue was concerning us during the thesis research. We needed to study the control and regulation of the diffraction patterns of the corresponding waves for further applications. The ability to direct, focus or collimate ultrasound waves at certain angles have been studied for decades for various applications, e.g: radar, sonar, theaters, microscopy, etc... [72,73] The term acoustic lens was very common in the past as different materials were used to change the diffraction properties of the propagating waves [73–75]. In the last two decades, Phononic Crystal (PC) was used as a more convenient solution

to direct the waves thanks to the characteristics of material periodicity [76,77]. Dispersion relations for propagation modes are regulated in PCs that can modify wave convergence, divergence or collimation depending on PC parameters and propagating wavelength [77–79]. Self-collimation happens in such a way that ultrasound waves can propagate without diffraction broadening [80]. This phenomenon can be used to control the propagation of ultrasound waves and directivity of sources [81].

Using these diffraction properties can be used to develop an ultrasound lens by means of a PC that can control the propagation in other materials behind the lens for various applications. This was applied extensively in the past to focus and self-collimate ultrasound waves exiting from a PC in fluid materials [82]. However, up to our knowledge, the use of PC as an ultrasound lens to control the propagation in solids behind the crystal was not studied deeply. We are going to show the basic background for ultrasound propagation properties in PCs.

El Mokhtar Hamham et al., studied Nonlinear self-collimated sound beams in sonic crystals using a fluid medium with elastic quadratic nonlinearity, where the dominating nonlinear effect is harmonic generation under phase matching conditions [83]. N. Swinteck et al., studied the performance of Multifunctional solid/solid phononic crystal comprised a square array of steel cylinders in epoxy is shown to perform a variety of spectral, wave vector, and phase-space functions including acoustic wave collimation, a defect-less wave guide, a directional source for elastic waves, etc... [84] V. Romero Garcia et al., studied Propagation of sound beams behind sonic crystals by analytical numerical methods showing the main focusing characteristics, such as the focal distance, the width of beam waist, and the beam quality at the waist [85]. Serkan Alagoz studied experimentally intensity maps of far-field focusing using a two-dimensional triangular lattice sonic crystal and intensity maps of near-field focusing using a two-dimensional square lattice sonic crystal for various scatter materials [86]. C. Cro¨enne et al., studied bandgaps in

phononic crystals considering different generation mechanisms and interaction effects. [87]. B. Morvan et al., used a PC-based two-dimensional solid/solid composite to demonstrate experimentally and theoretically the spatial filtering of a monochromatic nondirectional wave source and its emission in a surrounding water medium as an ultra-directional beam with narrow angular distribution [88]. C. Charles et al., investigated the propagation of elastic waves in 2D phononic crystals using plane wave expansion method is used to calculate the dispersion relations of guided elastic waves in these periodic media, including 2D phononic plates and thin layered periodic arrangements[89] . Ralf Lucklum studied the ability to magnify the interaction of acoustic waves with matter through specific geometries that are capable of concentrating acoustic waves in a confined volume forms the basis for a novel type of biosensor [90]. N. Jimenez et al., reported the nonlinear focusing of ultrasonic waves by an axisymmetric diffraction grating immersed in water. They showed numerically and experimentally that the focal gain of the system extraordinary increases in the strongly nonlinear regime. Particularly, the harmonic generation is locally activated at the focal spot, and the second harmonic beam is characterized by strongly reduced side-lobes and an excellent beam profile as experiments show in agreement with theory [91].

PCs are artificial materials constituted by a periodic repetition of two different materials with different dielectric constant (or equivalently the refractive index). The periodicity of the structures can be in 1D, 2D or 3D in a 3D space dimension system as shown schematically in Figure 1-15. We call the spatial periodicity of the PC in space the real lattice [92,93].

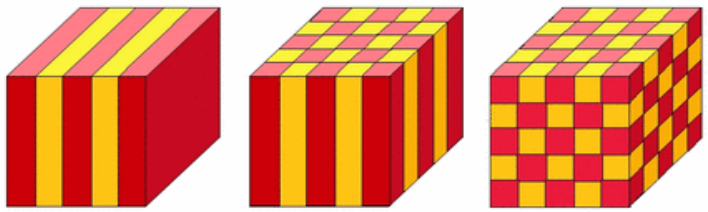

Figure 1-15: 1D, 2D and 3D periodicity of structure in 3D space.

This periodicity in space affects the propagation of ultrasound waves passing through the PC and changes its diffraction nature behind the PC [94,95]. PCs are analogous to Photonic Crystals that do the same change in diffraction properties in light beams. If we have a screen that collects the wave behind the crystal, we can see that there is some periodicity of the light/ultrasound beams on the screen. This periodicity of the diffracted beams, on a target screen, is called the reciprocal lattice. If the spacing between real lattice crystal atoms (inclusions) is wider, the light/ultrasound spots get closer on the screen and vice-versa. When atoms of the real lattice crystal get closer in one dimension, the reciprocal lattice expands only in this direction.

The relationship between spacing of periodicity in reciprocal and real lattices is as shown in Figure 1-16 Where 'a' is called the lattice constant. Propagation of acoustic waves in PC is governed by the Bloch or Floquet theorem from which one can derive the band structure in the corresponding first Brillouin zone [92–95]. The first Brillouin zone is defined as the Wigner–Seitz primitive cell of the reciprocal lattice. Thus, it is the set of points in the reciprocal space that is closer to K = 0 than to any other reciprocal lattice point where K is the wave vector [96]. Due to the periodicity of the crystal lattice, the waves passing through it suffer wave dispersion, i.e: wave's velocity depends on wave's frequency and wave vector direction [94–96].

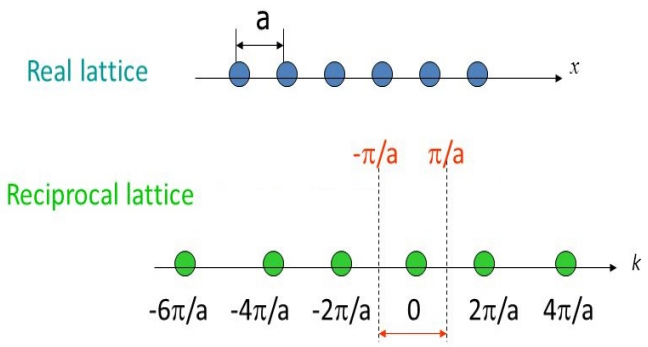

Figure 1-16: relationship between real and reciprocal lattices

There is an analogy between lattice in real space dimensions (Figure 1-17a) and reciprocal space (wave-vector) space dimensions as shown in Figure 1-17b. For both directions *kx,ky* in the wave-vector space, there are different modes propagating in *Γ-K-M* directions as shown in the dispersion curves in Figure 1-17c where Each continuous curve represents a propagation mode (vertical axis represents frequency while horizontal axis represents wave vector sections in directions highlighted in Figure 1-17b). The dispersion relationship in a PC is considering all propagating frequencies at a specific wave number *kx. ky* scanning across all wavenumbers inside the Brillouin zone, we can find that the dispersion relationship is composed of discrete bands formed due to the periodicity of the medium. Depending on the dimensions and shape of the PC, some frequencies are forbidden to propagate in certain wave vector directions [94–97]. This feature is referred to as Bragg gaps. They appear due to the destructive interference of scattering waves because of the inclusions. If all frequencies are forbidden to propagate at all directions, it is called band gaps. If they are prevented to propagate at specific directions, they are called band stops [87].

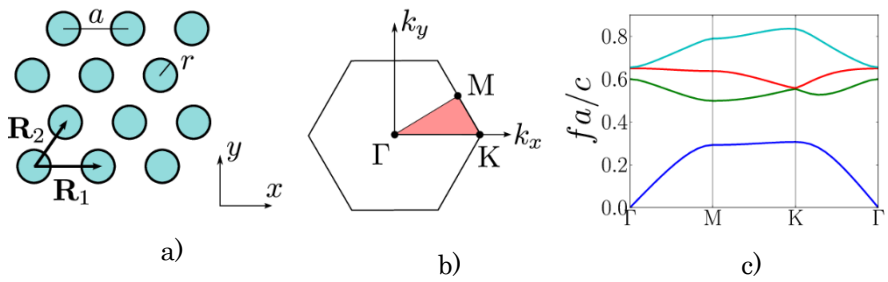

Figure 1-17: a) real lattice propagation directions b) reciprocal lattice propagation direction in reciprocal space (wave-vector space) c) dispersion curves of the propagation modes [97].

Dispersion curves in Figure 1-17c are used for creating a contour map for each frequency response at all the wave-vector directions. This contour map can help deduce the nature of diffraction of ultrasound waves at each iso-frequency contour curve. Iso-frequency contour maps are plots that identify the intersection of a specific frequency with a dispersion surface, by applying this plot strategy to all allowed frequencies of propagation, we get a complete iso-frequency contour maps across all wave-vectors [94–97]. The importance of these iso-frequency contours is their ability to determine the direction of propagation of the wave corresponding to a wave vector. Plane waves in propagation will acquire phase shifts depending on their propagation angles, consequently, this phase difference between the components results in a diffractive broadening of the [92,93,98]. A concave contour line would result in positive diffraction (divergence), a convex contour line on the contrary results in negative diffraction (convergence or focusing) [98–101]. Additionally, any flat contour line would mean that all these wave vectors are going to pass without suffering any diffractions, hence the concept of self-collimation [81,102]. Figure 1-18 shows the concave, flat and convex contour lines and their effect on diffraction for the discussed 3 cases respectively [92,93].

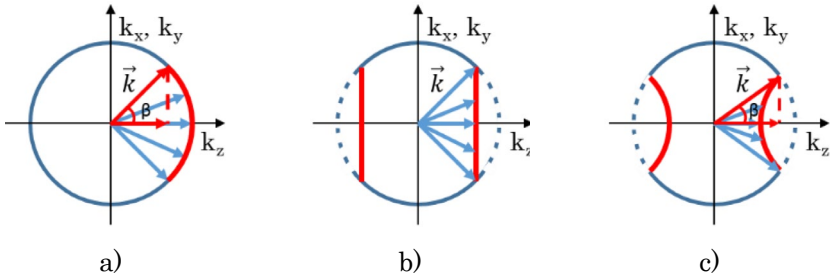

Figure 1-18: Geometrical interpretation of diffraction of the beam propagating along z axis: a) Spatial dispersion for homogeneous materials, where due to the phase difference between $\vec{k}$ vectors, occurs positive diffraction of the beam (focusing); (b) Modified spatial dispersion (by PC) where flat parts on the surface/curve appear. For the flat part of spatial dispersion, all $\vec{k}$ vectors propagate at the same velocity with respect to z axis, therefore self-collimation is obtained (c) modified spatial dispersion (by PC), where convex curvature of the $\vec{k}$ vectors is responsible for the appearance of negative diffraction [92].

Our goal is to use the diffraction control properties of the PC in order to generate an ultrasound lens that can focus or self-collimate ultrasound waves behind the PC (ultrasound lens). At the current research stage and presented here in the thesis, we start by the simulation process using a famous FEM software (COMSOL).

Chapter 2. Experimental set-up and one-dimensional defect reconstruction

As stated in the preface, this thesis is focused on the research of a hybrid photonic – phononic configuration to be used in a NDT configuration for the detection of embedded defects in metallic samples. In this chapter we show the general configuration of the experimental setup we propose, in its simplest configuration. This setup has been used, with several modifications that will be highlighted later, in the other thesis chapters, unless otherwise indicated. The goal of our first experiment is to detect the location of a defect using 1D B-scan analysis. The NDT analysis applied in this section considers a simple metallic object sample with a small thickness and a well-defined defect as a starting point for the studied research. For comparison, we perform the same measurements with a commercial scan array system available in the market.

2.1. Experimental configuration

The schematic representation of our first experimental setup is shown schematically in Figure 2-1. We use a pulsed Nd:YAG laser (Litron, model LPY604-10) which emits pulses of 10ns with a tuneable repetition rate between 1 and 10 Hz. The laser emits in infrared at 1064nm, but in our experiments we have used the second harmonic of this radiation at 532nm generated in a nonlinear crystal. The maximum available energy

is 200 mJ at 532nm. The diameter of the laser beam at the output is of the order of 5 mm and we can focus it to smaller spot size on the object by the use of different focal lenses, increasing the intensity. The focused laser beam impacts onto the surface of the object under study where the pulse is rapidly absorbed into a shallow volume of the material and creates a localized thermo-elastic expansion. This expansion induces a stress wave and an acoustic pulse generating broadband ultrasound waves that propagate inside the material. The laser beam can scan a selected line or an area of the object surface depending on the required experiment by means of a programmable XY galvanometer (model GVS302, Thorlabs). For each excitation point, the ultrasound waves propagate through the object and they are reflected or scattered by the material defects and boundaries. The ultrasound is then detected by a classical ultrasound transducer/s [28].

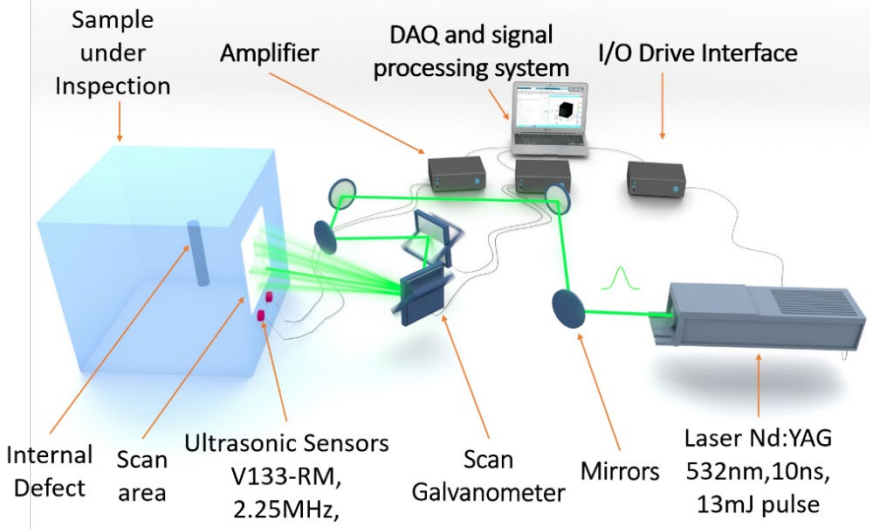

Figure 2-1: Schematic representation of the experimental set-up

For the detection, depending on the required experiment, we either use one or two conventional ultrasound transducer/s (Olympus V133-RM)

at 2.25 MHz central frequency, coupled to the surface of the object. The sensor/scan is placed on the incident surface (measuring reflection/scattering) as well as on the opposite side (measuring transmission). The signal collected by the transducer is sent to a preamplifier (Olympus 5662), connected to a high-performance Gage A/D card (50 MHz sampling frequency, 16 bit of resolution), linked to a computer for further data processing. For each excitation point the transducer records a voltage/time (A-scan) data set.

We considered a longitudinal wave propagation in all studies highlighted in this thesis as it penetrates to the depth of the material. Moreover, our ultrasound receiver's response has higher efficiency at detection of longitudinal waves. The velocity of longitudinal wave propagation in homogenous aluminium (the material used in this study) is 6300 m/s [5].

With this set-up we have tested different samples. . Initially, we analyse two aluminium cuboid samples with identical dimensions of 300 mm x 200 mm x 20 mm. One sample is homogeneous, without any holes or defects, referred in the following discussion in this chapter as "healthy". The second one has a cylindrical hole drilled at the top of the cuboid with a diameter of 8 mm and hole depth of 85mm and is referred to from now on in this chapter as "unhealthy" sample. Figure 2-2a,b show a general representation of both the healthy and unhealthy samples respectively. Figure 2-3 shows a detailed representation of the unhealthy sample together with the laser scanning line and the sensors position.

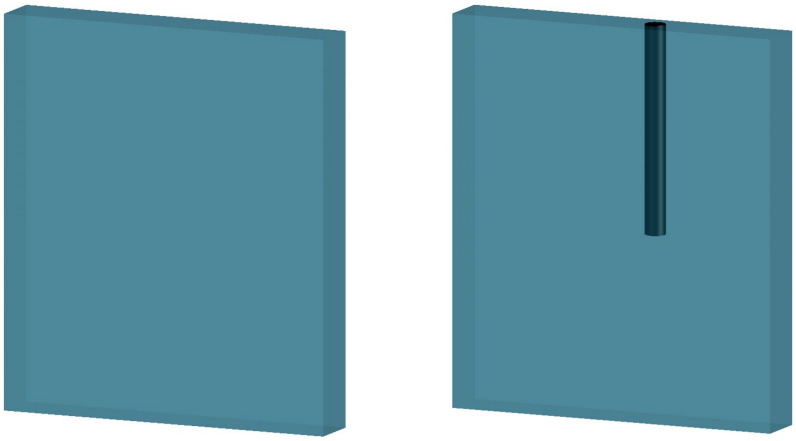

a) b)

Figure 2-2: Representation of the a) healthy and b) unhealthy sample objects used for the experiment, with the unhealthy sample containing a drilled hole from top side.

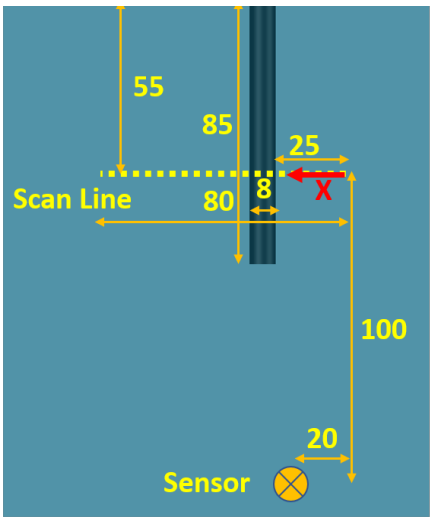

Figure 2-3: Experimental sample with a scan line and ultrasound sensor for B-scan experiment

Prior to more complex experiments and to the application of the reconstruction algorithms for the defect size and location detection, it is mandatory to characterize the initial A-scan signal received by our transducers and their frequency spectrum. The result of an A-scan signal

measured by our transducer is shown as voltage as a function of time in Figure 2-4a, with its Fourier transform frequency spectrum shown in Figure 2-4b. A 3rd order bandpass Butterworth filter is applied to this signal with cut-off frequencies of 1MHz to 4MHz as well as an interpolation filter is shown in Figure 2-4c. The corresponding Fourier transform for the filtered signal is shown in Figure 2-4d. The bandpass filter is used in order to limit our signal processing to high amplitude signals that are within our transducer's sensitive bandwidth and reject captured signal at the transducer's low sensitivity spectrum. This pre-processing signal conditioning is applied to all signals as a pre-requisite before proceeding with any further defect detection algorithm for all experiments discussed in this thesis.

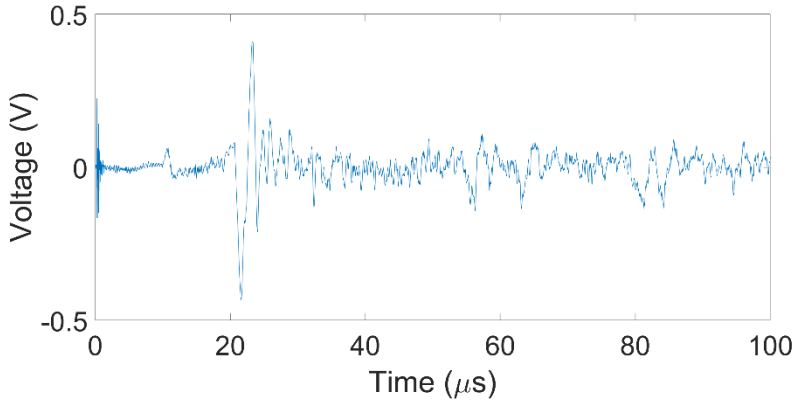

a)

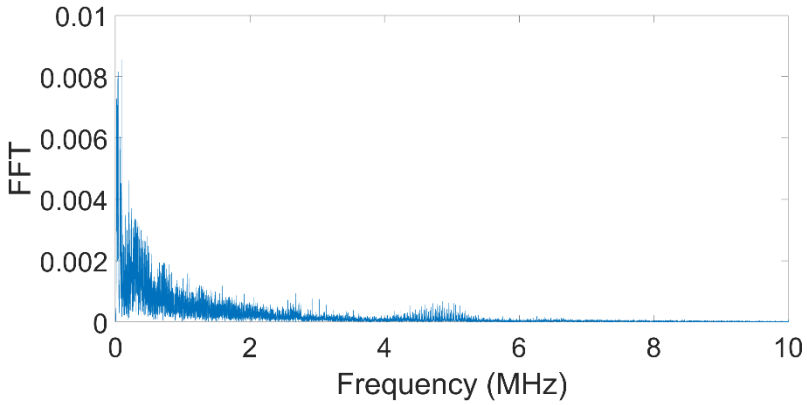

b)

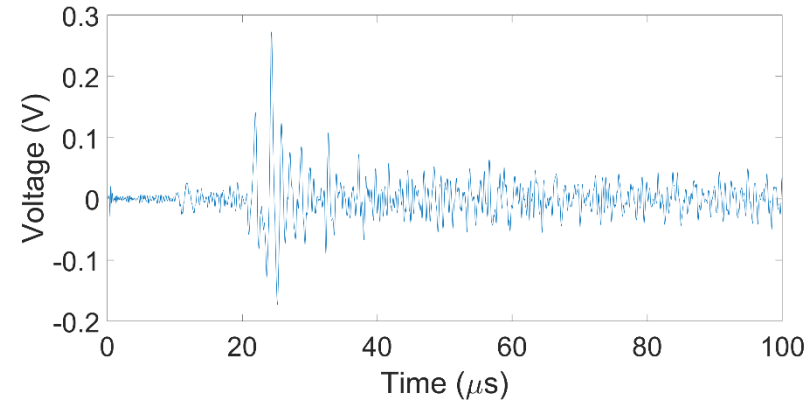

c)

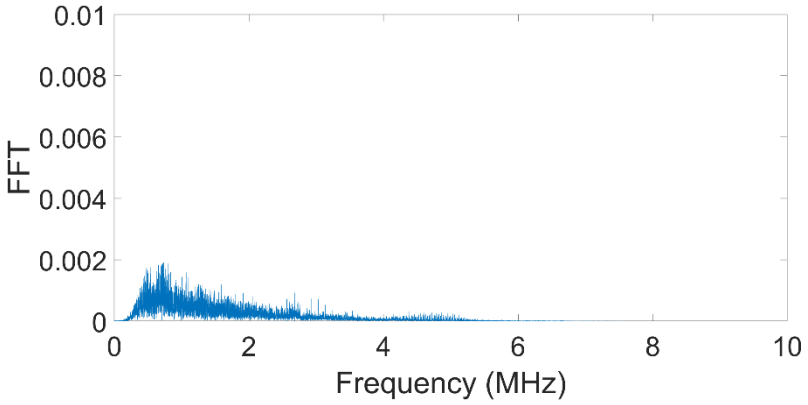

d)

Figure 2-4: Example of AE signal received during the healthy sample test. a) Raw A-scan time-based signal. b) Fourier transform frequency spectrum of the A-scan signal shows broadband response c) A-scan signal after applying the Butterworth and interpolation filter d) Frequency spectral content after applying the Butterworth and interpolation filters.

2.2. One-dimensional reconstruction of the defect: B-scan experiment

2.2.1. Experimental setup configuration

In this experiment, we analyse the healthy and unhealthy samples with the dimensions described previously and shown in Figure 2-3. The scanning was carried out using the galvanometer described in the previous section that was programmed to execute a 1D scan (B-scan) along one line of the object surface in the horizontal (X) direction, passing above the location of the defect (Figure 2-3). We selected 120 scan points covering a distance of 80 mm. For each excitation point the ultrasound waves detected by the sensor were recorded using our data acquisition system. This B-scan analysis is the most commonly used in commercial devices that are used in the industry worldwide.

2.2.2. Results and discussion

As a first step in the signal processing of the recorded data we applied a 3rd order Butterworth bandpass filter of 3 MHz bandwidth around the 2.25 MHz central frequency and an interpolation algorithm, in order to reduce the excessive oscillation noise and unnecessary perturbations [28].

The B-scan results for all processed signals are shown in Figure 2-5a. for the healthy sample, and in Figure 2-5b for the unhealthy one. We plot the position of the scan points as a function of the time of flight (*TOF*) frames, while the colour bar represents the intensity of the signal. *TOF* is calculated according to Equation 1-19 by considering the distance from source to each scattering point and back to the receiving transducer. A higher intensity is a sign of a high reflection towards the sensor coming

from a reflecting source that can be a boundary or a defect embedded in the object under test.

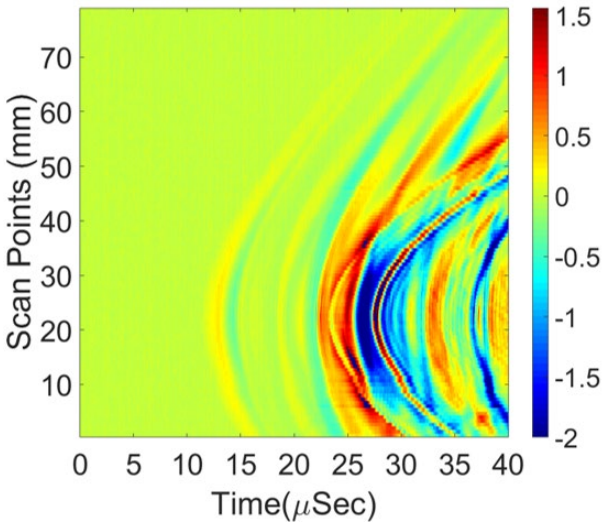

a)

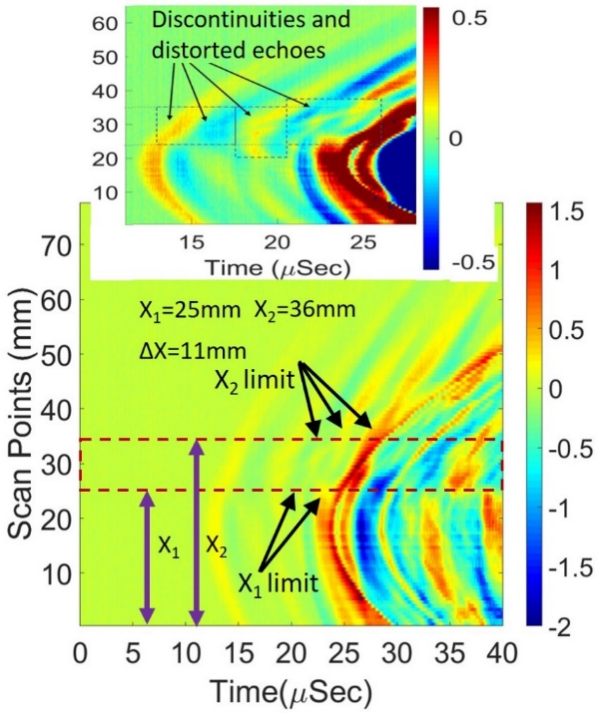

b)

Figure 2-5: a) B-scan results of the healthy sample b) B-scan results of the unhealthy sample with an inset zooming the discontinuities.

The *TOF* of the waves depends on the distance between the laser incidence point and the ultrasound sensor's position. The first wavefront arriving from the laser to the sensor starts to appear at time $t = 11$ μs for both samples, since the relative position of the laser scan line and the sensor was the same. For the healthy sample there is no visible perturbation in the B-scan map, due to the homogeneity of the sample. All reflections come from the boundaries. For the unhealthy sample we see the same boundary reflections, overlapped with the reflections coming from the defect. The latter ones alter the B-scan map, showing major discontinuities and perturbations that correspond to the reflections from the defect. The inset of the Figure 2-4b shows the enhanced area of the discontinuity. The colour map is reduced to lower bounds to emphasize and exaggerate the colour contrast and make it more distinguishable.

We need to emphasize that the echoes from the hole are reflected from both the front and rear surfaces of the cylindrical defect. Front surface is providing higher intensity due to this reflection, while the signal passing to the rear surface is already moving through the air volume filling the hole until it reaches the rear surface and then reflected back to the transducer (passing again through the air in the hole during the return path). This solid/air boundary effect distorts and attenuates the signal and causing lower amplitude for this reflection in addition to abrupt change in the signal behaviour due to change of media of ultrasound propagation. Other latter echoes appearing on the time axis are results of multiple back and forth secondary reflections from defect and boundaries and include a lot of interference making it further complicated to separate the individual echoes. Thus, they are not essential in this analysis. These main reflections are highlighted by the arrows in the Figure 2-5b with the full colour map range.

As highlighted in Figure 2-5b, the discontinuity clearly appears in the range between X_1=25 mm and X_2=36 mm. This means that the defect size in the x direction is ΔX=11mm, centred at X=30.5 mm. We compare these results with the real hole diameter ΔX_{real}=8 mm and its real position on the sample centred at X=29 mm and we obtain a sizing error of 37% (the defect appears to be bigger than it really is), and a positioning error of 4%.

This first experiment shows that the B-scan algorithm, using a remote 1D LGU exciter scan and only one receiving transducer, is a very simple and robust technique that provides reliable information about general position of the defect location and size in a fast measuring process. The resolution of the results is comparable with the commercial NDT full ultrasound devices, available on the market, but have the advantages of noncontact excitation and remote control of the scan. However, this method, due to the linear scan of the excitation is limited to the 1D detection and does not allow a 2D reconstruction of the defect,

We wanted to compare the results of our reconstruction those acquired using a commercial Ultrasound Scan Array device. We have used a device called Omniscan MX2 manufactured and sold by Olympus. The machine uses a scan array of 48 active ultrasound transducers that work in a pulse-echo mode, which represents the defect location to a good accuracy level. We conducted two measurements. In the first one the transducer is placed on the 300mm*200mm plane, being located on top of the cross-section of the hole. In the second experiment (measurement) the array is placed (or positioned) away from the cross-section of the hole. The results of these two measurements are shown in Figure 2-6 and Figure 2-7.

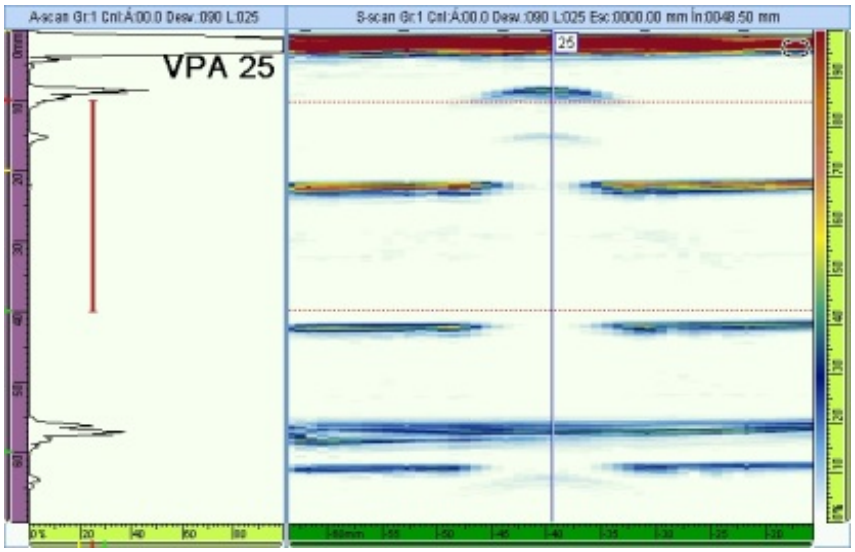

Figure 2-6: Phase array scanning an 8mm hole-phased array at a position passing by the middle of the hole.

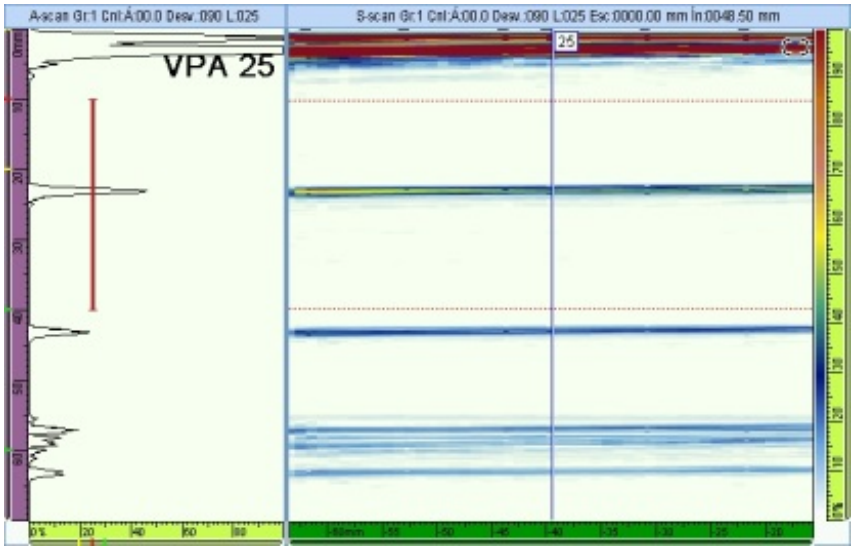

Figure 2-7: Phase array scanning a 8mm hole-phased array at a position passing away from the hole.

In both figures, the left-hand side LHS (A-scan) is representing the reflections from the first reflector which could either be a boundary or an embedded defect. The number on top-left side represents the number of the individual receiver in the 48 array that detected the represented A-scan signal. The right-hand side RHS graph shows the position of this

material reflector that is detected by all the 48 elements of the detecting array in cascaded order from left to right. Due to multiple reflections back and forth from the object boundaries, we can see the different reflection echoes represented as pulse in LHS and straight blue lines in RHS graphs. When a defect is interrupting the ultrasound signal both at a distance shorter than the distance to the object boundaries, a separate shifted pulse at LHS graph and a separate blue curve at RHS graph is appearing at a depth equivalent to the position of the defect as shown in Figure 2-6.

We found that the Omniscan sensor cannot detect any reflections from the hole unless it is vertically positioned under the sensor array scan area as shown in Figure 2-7 where the measurement was taken only 10mm shift away from the defect position (sensor was not able to see the defect). On the contrary, our B-scan experiment, where the ultrasound exciter and receiver are separate components working in a pitch-catch mode, it is not necessary for them to be vertically positioned above the hole defect. Yet we still require a large scan area in our setup in order to get reasonable results.

The defect measured with the Omniscan device appears between positions X=33mm and 47mm, which means a defect size of 14mm, which corresponds to a size error of 75%. This error is much higher than the one achieved with the B-scan analysis whose error was 37%. This happens because of the large size of the Omniscan ultrasound array.

2.3. Conclusion

This first experiment implementing a simple experimental set-up shows that using a remote 1D LGU scan (B-scan) and only one sensor we can easily localize the position and size of the defect with a very good position error and an acceptable size error (a sizing error of 37% and a positioning error of 4% in comparison to commercial device whose

corresponding errors are 75% and 0% respectively). This configuration, although similar to ultrasound array commercial devices, allows a noncontact linear scan of the excitation that combined with only one detector give an enhanced resolution in the defect detection. As limitation, we can only make a 1D measurement of the defect, parallel to the scanning line (*X*-axis in this case). If we want to make a 2D reconstruction of the defect, we have to move to a 2D scan configuration.

Chapter 3. A 2D laser ultrasound inspection and defect reconstruction based on Wavelet Transform and Data Clustering

In Chapter 2, only 1D information about the defect position and dimension can be obtained. In this chapter we extend the reconstruction of the defect to 2D. We chose a cube-shaped object with an embedded volume defect and we modify the experimental including a system able to scan the laser excitation point along a particular direction. We apply an alternative algorithm known as wavelet analysis, with a different signal processing procedure, which is able to detect, analyse and extract the information about the defect embedded in the metallic object under test.

3.1. Experimental set-up and results

The experimental configuration for this experiment is similar to that discussed in section 2.1 with same hardware for laser excitation, galvanometer for scanning and receiver as well as the data acquisition system of the captured signals. In this experiment, we use only one transducer for detection. The schematic diagram of the entire laser-

ultrasound inspection system configuration, considered for method validation, is shown in Figure 3-1.

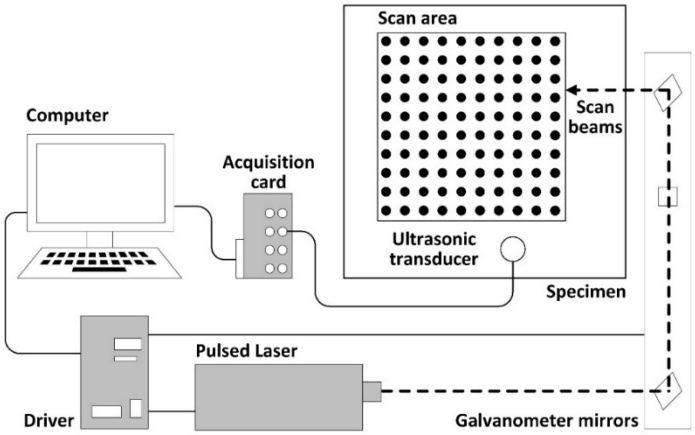

Figure 3-1: A schematic diagram of the laser ultrasound inspection system configuration, including the pulsed laser, galvanometer mirrors, acquisition card, and ultrasound transducer.

As shown in Figure 3-2, the considered aluminium object to be inspected is 200 mm × 200 mm × 200 mm, with a mechanically induced cylindrical defect sized 40 mm of length and 13 mm of diameter located at 95 mm depth from the specimen's surface considered during the inspection. The scan area is 90 mm × 90 mm covered by 10 × 10 laser scanning points. The aluminium object is fabricated on a local casting workshop. The aluminium was cast on a prepared cubic model. A piece of hard glass with cylindrical shape was placed inside the model with the dimensions and positions mentioned in Figure 3-2b and Figure 3-2c to act as the internal defect. The glass was hard solid and temperature resistant to withstand the casting of the hot liquid aluminium [30,32].

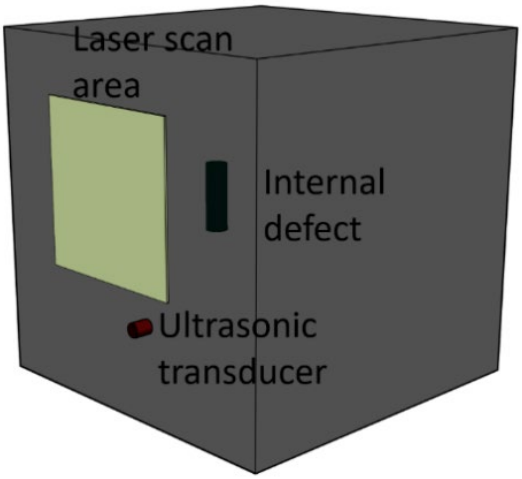
Laser scan area
Internal defect
Ultrasonic transducer

a)

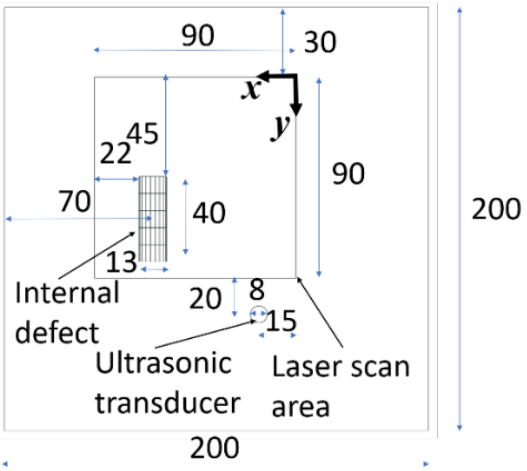
90
30
x
y
45
22
90
70
40
200
13
Internal defect
20
8
15
Ultrasonic transducer
Laser scan area
200

b)

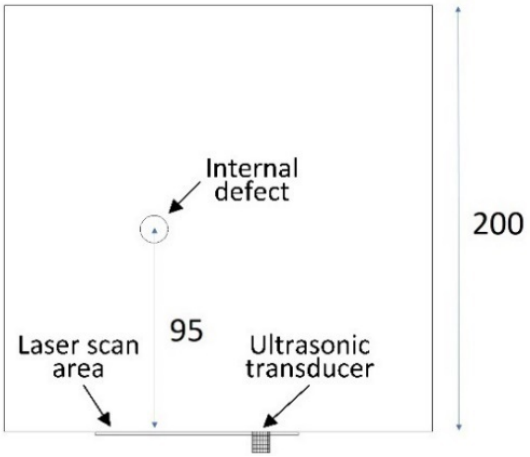

c)

Figure 3-2: Aluminum specimen, internal damage and laser scan area. All dimensions are in millimeters. (a) Isometric view. (b) Front view. (c) Top view.

For each laser excitation point in the scanning area in Figure 3-2, the fixed receiver records a corresponding A-scan signal. We filter the signal using the Butterworth filter with a 3rd order bandpass 3MHz bandwidth (with cut-off frequencies of 1MHz to 4MHz, same as in section 2.1) and the filtered signal is used later for further signal processing described below.

3.2. Wavelet algorithm analysis

The wavelet transform is proposed as a time-frequency processing tool. The characteristic damage frequency patterns are studied, identified, and tracked back to the boundaries of the source, i.e., the damage spatial location in the component under inspection. Then, a damage reconstruction procedure is proposed based on the estimated time of flights of the ultrasound damage propagation patterns. The contribution of this study lies in providing a new approach of damage detection, localization, and shape reconstruction based on detection and processing

of the damage ultrasound echo characteristics. An adaptive resolution method using wavelet transform was chosen in order to check the proposed methodology under a laser-ultrasound scheme.

Novelties of this work include a new damage pattern tracking method over the WT-based time-frequency maps, and a time of flight-based damage localization and visualization procedure; both are supported by the application of a density-based spatial clustering algorithm in order to identify the highest probability regions of damage location. It must be noticed that for the first time, to the authors' knowledge, this processing scheme and this damage visualization procedure have been used in the laser-ultrasound inspection of metallic specimens. According to the obtained results, the proposed methodology is reliable and feasible for defect detection and quantification of metallic damages in industrial applications since the proposed method does not require any reference information. The WT uses small and finite oscillating signals called wavelets as a basic function for representing a signal. The wavelet-based transform has the advantage of adapting time and frequency resolutions to the signal contents, which is known as multi-resolution analysis. This results in a good time-resolution and a limited frequency-resolution at high frequencies, and a good frequency-resolution and a limited time-resolution at low frequencies, which is highly suitable for characterizing short-duration events of high frequencies and long-duration events of low frequency components [30,32,64].

The main purpose of the initially selected mother wavelet is to provide a source function to generate the daughter wavelets which are simply the translated and scaled versions of the mother wavelet [103]. The WT employs a sliding window function that is used to decompose the target signal into a sum of wavelets added together. Each wavelet has finite propagation in time determined by the window size. These wavelets are limited in time, whereas sinusoidal functions that are used for the Fourier-based transforms are continuous in the whole-time range. Hence,

the wavelets are stretched and compressed in frequency. They are also shifted in time to correlate with the original signal under analysis in order to determine the set of frequencies propagating at any instantaneous time moment, following the Heisenberg principle of uncertainty [104]. The WT can be represented by Equation 3-1:

$$x_{\omega}(a,b) = \frac{1}{\sqrt{|a|}} \int_{-\infty}^{\infty} x(t)\psi^{*}(\frac{t-b}{a})dt \qquad 3\text{-}1$$

where $x(t)$ is the target time series, x_{ω} is the resulting wavelet analysis, ψ^{*} is the complex conjugation of the mother wavelet that has to be a continuous function in both time and frequency domains, a is a scale factor that either stretches (large a) or compresses (small a) the wavelet and, b is the signal's shifting parameter in time. By choosing a different mother wavelet, different characteristics of the time signal can be emphasized as an output. The flexibility of choosing the optimal mother wavelet is one of the advantages of using WT, for the choice of the mother wavelet for a particular problem improves the signal processing capability of the technique. If the shape of the signal to be detected is known a priori, a replica of the set can be utilized as the mother wavelet function, or the mother wavelet can be chosen from a set of theoretical signals. In this regard, the Morlet wavelet is extensively used and ultrasound signals are investigated due to their behaviour which is close to the detected signals. It has been proven to be efficient in improving the signal strength and reducing the noise, making the WT-based technique extremely useful for damage detection [48].

3.2.1. Preliminary wavelet signal analysis

An example of the ultrasound waves resulting from the thermal mechanism induced during the pulsed laser excitation scan is shown in Figure 3-3.

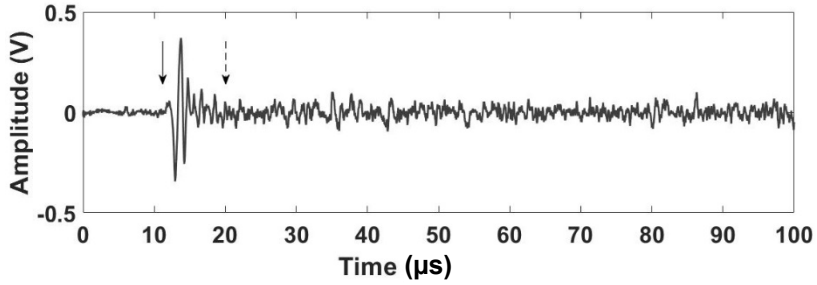

.

Figure 3-3: An example of the resulting laser-generated ultrasound wave experimentally measured over the defective aluminum specimen. The solid arrow indicates the time of the direct laser-induced ultrasound wave arrival (detected visually), while the dotted arrow indicates the estimated time instant of the ultrasound defect-reflected echo arrival (detected theoretically). The absolute coordinates corresponding to the laser scan point are x = 11 mm and y = 51 mm, while the absolute coordinates corresponding to the ultrasound transducer are x = 15 mm and y = 110 mm.

The time of the initial ultrasound wavefront arrival to the ultrasound sensor in Figure 3-3 can be detected visually at the time 12.25 μs. Although the damage effect in the time domain of the recorded ultrasound signal is not detectable, such influence can be expected at time 20.50 μs. This is calculated theoretically as follows [105]:

$$TOF = \frac{\sqrt{(x_{laser} - x_{defect})^2 + (y_{laser} - y_{defect})^2 + (z_{laser} - z_{defect})^2}}{Longitudonal\ Velocity} + \frac{\sqrt{(x_{sensor} - x_{defect})^2 + (y_{sensor} - y_{defect})^2 + (z_{sensor} - z_{defect})^2}}{Longitudonal\ Velocity} \quad 3\text{-}2$$

This section shows the wavelet analysis of each A-scan signals detected by the sensor at positions indicated in Table 3-1 [32]. Three different types of mother wavelets are used to analyse the signal, namely the Morlet, Mexican hat and db4. The three mother wavelets are very

popular for ultrasound wave analysis due to their high correlation with the ultrasound wave form.

Figure 3-4 shows the cross-section front view at *XY* plane of the cylindrical defect embedded at depth of the object. The position of three arbitrary scan points at the surface of the object, used in this section as an example of how the analysis is performed, are superimposed on same figure for clarification of the horizontal and vertical spacing with respect to cylindrical defect. The exact data of the position of each scan point is represented in Table 3-1.

Scan point	X position	Y position	True time of flight
1	11	51	19.65
2	31	51	18.30
3	81	51	17.10

Table 3-1: Scan points considered for samples inspection.

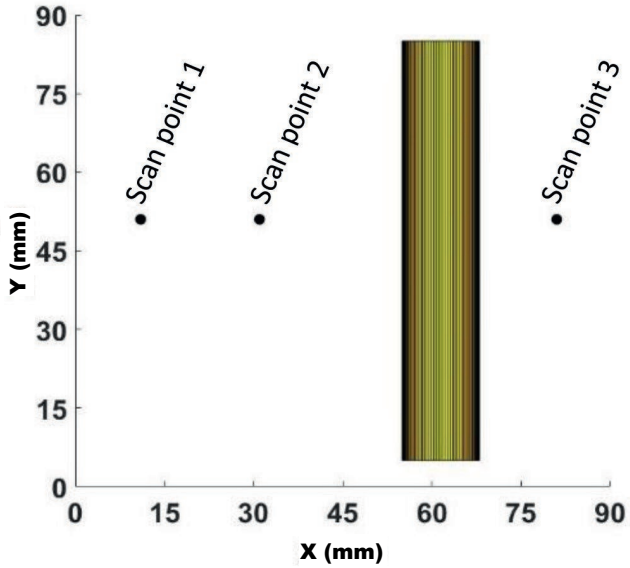

Figure 3-4: Scan points considered for sample inspection and synthetic defect location. At z=0mm.

Figure 3-5 shows the absolute position of the defect cylinder represented by top view for the three scanning points. In addition, the locus ellipsoid estimation based on distance corresponding to *TOF* from exciter to defect point scatter and back to the receiving sensor for the three scanning points. It can be seen that the intersection between the ellipsoid and the cylinder happens at the point of back scattering from the defect to the sensor.

It is shown in Figure 3-6 the wavelet contour map generated using Morlet WT. It is clear that the WT analysis resulted in clustering the signal into groups of segregated echoes. Each echo is governed by its intensity level, time duration, and scale levels. Scale levels are inversely proportional to the frequency spectrum. Hence, we can see lying at the top of the WT spectrum the echoes with low frequencies while the echoes at the bottom correspond to high frequency components. Each of these echoes starts at a certain time shift, and it is clear that the start of the echo is occurring at lower frequencies with less intensity, and later the higher frequency components start to appear with their intensity level increasing. *TOF* of the first echo is corresponding to the direct surface propagation of the signal from the excitation point to the receiving sensor position, while *TOF* of the second large echo signal is corresponding to the reflected signal from the defect. It is possible to estimate the corresponding *TOF* based on that conclusion to be 20, 19, and 18.5 μs for Figure 3-6**a,** Figure 3-6**b** Figure 3-6**c**, respectively.

Figure 3-7 and Figure 3-8 represent the same wavelet echo analysis for Mexican hat and db4 mother wavelets respectively. Table 3-2 show the resulting *TOF* from the internal defects at three scan points with reference to the different mother wavelets while Table 3-3 shows the error

of the resulting *TOF* compared to the calculated true *TOF* for each of the cases in Table 3-2.

Wavelet	Scan point 1	Scan point 2	Scan point 3
Morlet	20.22	18.58	18.28
Mexican hat	23.05	19.98	20.98
Db4	21.65	18.95	18.50

Table 3-2: Resulting time of flight from the internal defect in (μs).

Wavelet	Scan point 1	Scan point 2	Scan point 3
Morlet	0.57	0.28	1.18
Mexican hat	3.40	1.68	3.88
Db4	2.00	0.65	1.40

Table 3-3: Resulting time of flight error compared with the true time of flight, in (μs).

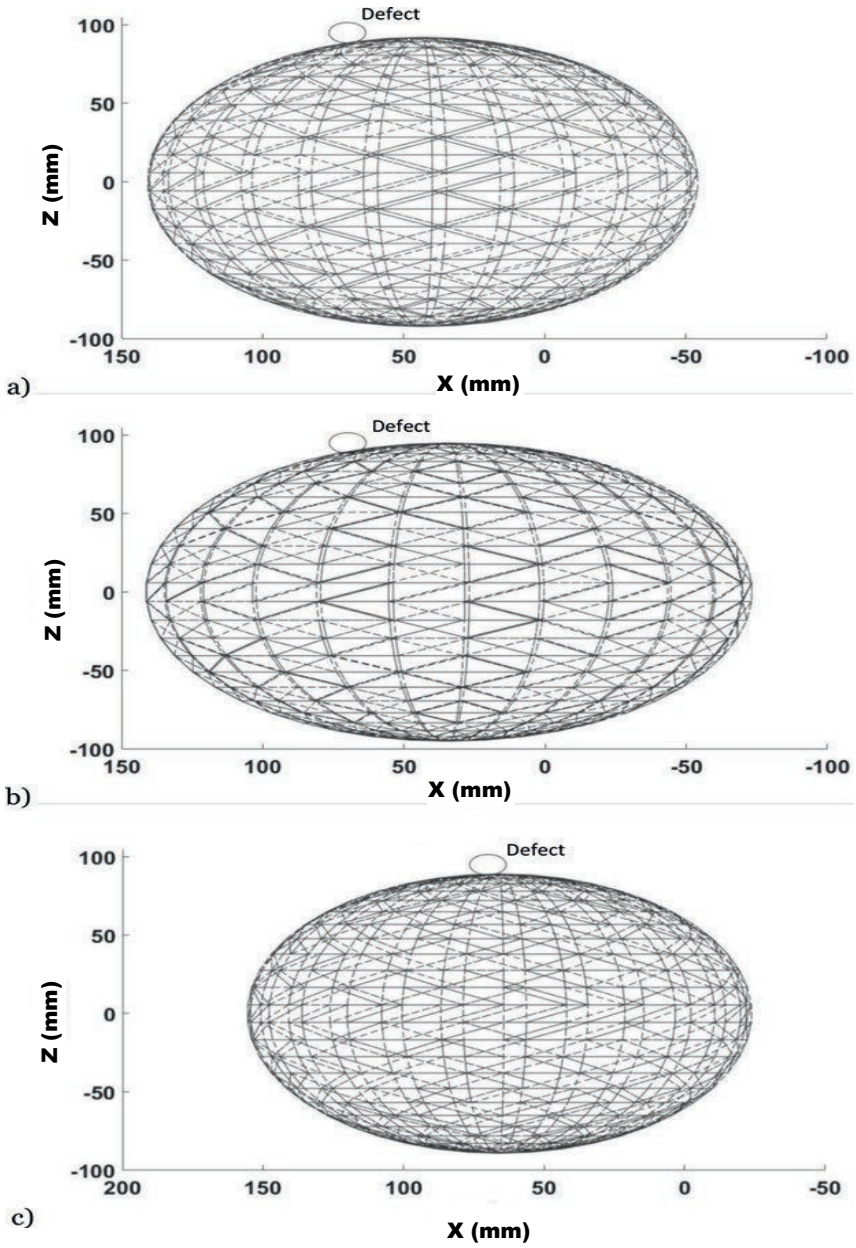

Figure 3-5: Ellipsoid locus of defect position based on true time of Flight estimation resulting from the scan point and acoustic transducer positions. (a) Scan point 1. (b) Scan point 2. (c) Scan point 3, Foci points of ellipsoid are: Scan point position and transducer position.

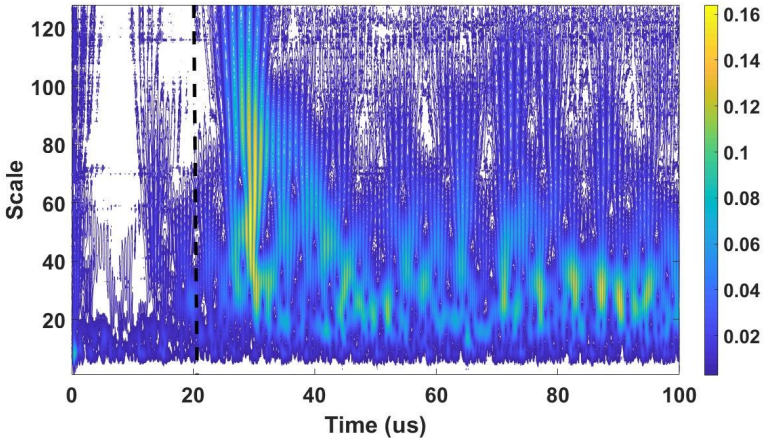
Scale
120
100
80
60
40
20
0
20
40
60
80
100
Time (us)
0.16
0.14
0.12
0.1
0.08
0.06
0.04
0.02

a)

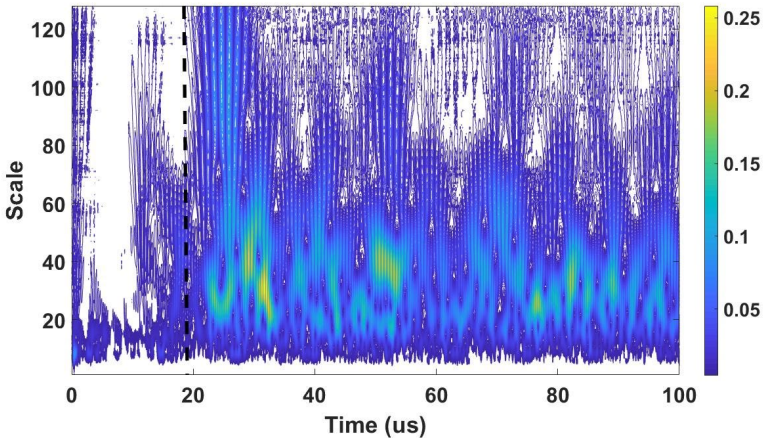
Scale
120
100
80
60
40
20
0
20
40
60
80
100
Time (us)
0.25
0.2
0.15
0.1
0.05

b)

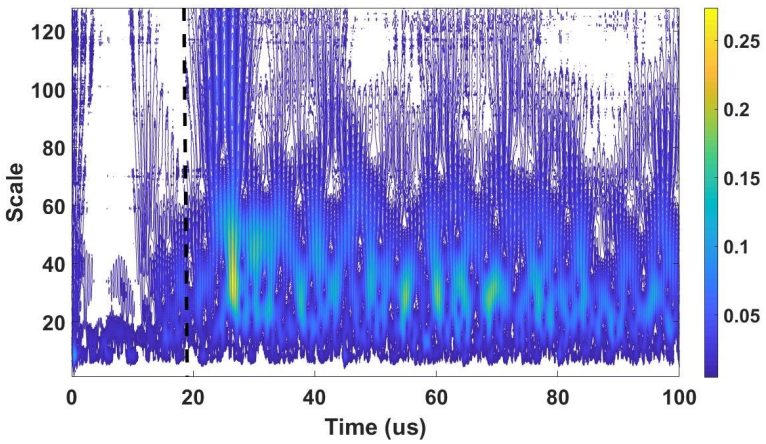
Scale
120
100
80
60
40
20
0
20
40
60
80
100
Time (us)
0.25
0.2
0.15
0.1
0.05

c)

Figure 3-6: Resulting wavelet contour maps with Morlet wavelet. (a) Scan point 1. (b) Scan point 2. (c) Scan point 3.

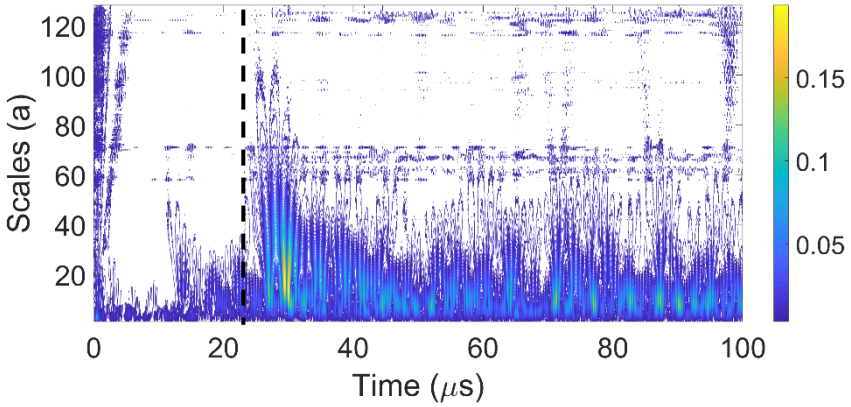

a)

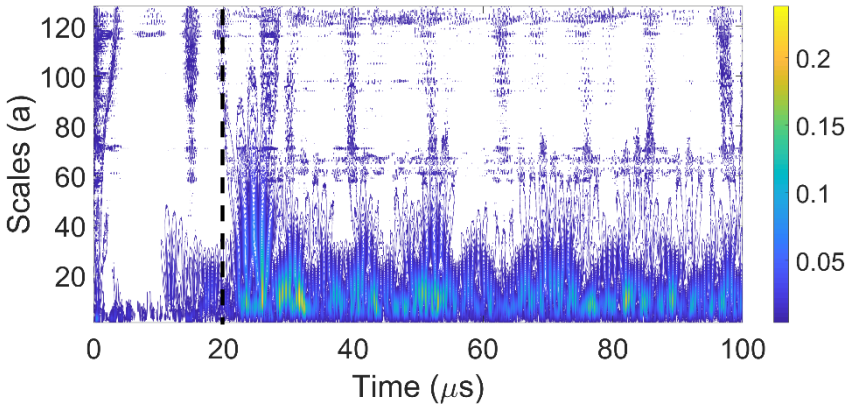

b)

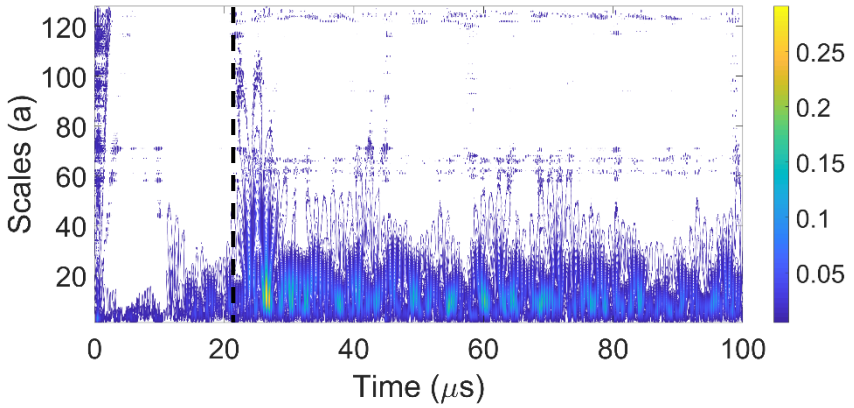

c)

Figure 3-7: Resulting wavelet contour maps with Mexican hat wavelet. (a) Scan point 1. (b) Scan point 2. (c) Scan point 3.

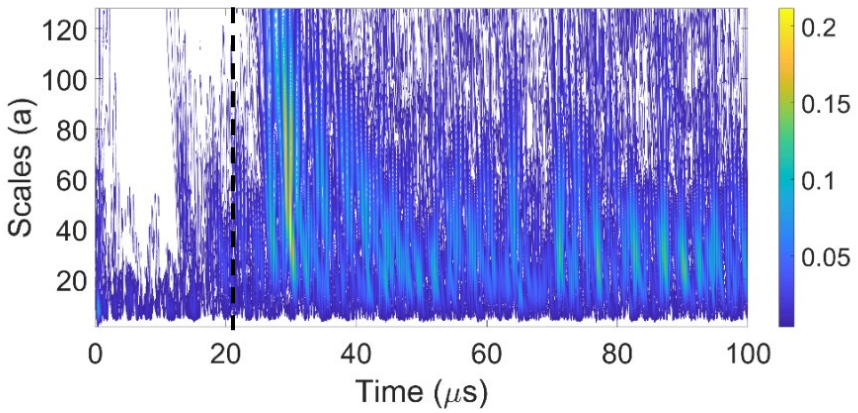

a)

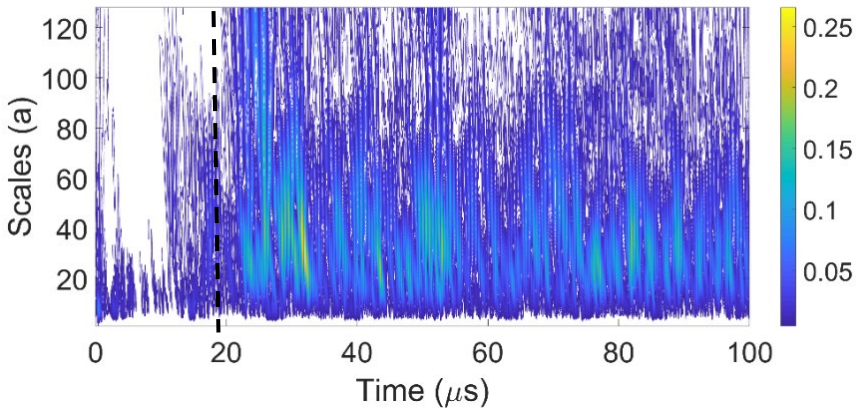

b)

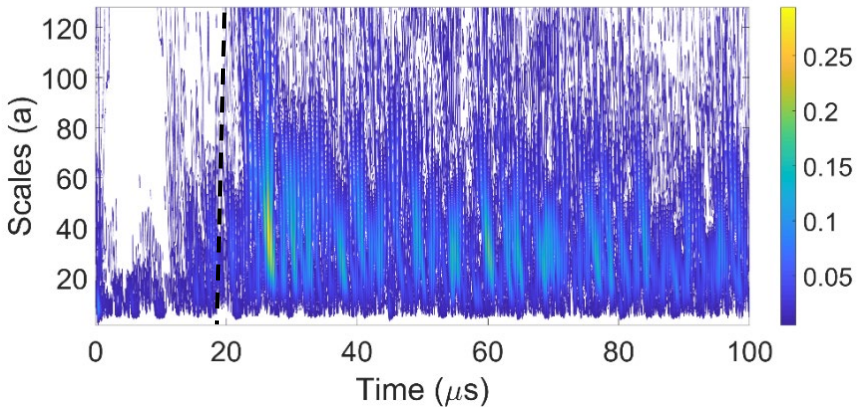

c)

Figure 3-8: Resulting wavelet contour maps with db4 wavelet. (a) Scan point 1. (b) Scan point 2. (c) Scan point 3.

It is found that the use of the Morlet mother wavelet gives the least estimation error and it is apparently the most accurate mother wavelet to use for this kind of analysis. We use the Morlet wavelet for the further analysis for the reconstruction of the defect in the main WT algorithm.

3.2.2. Defect reconstruction using wavelet analysis and clustering techniques

3.2.2.1. Signal analysis block diagram

The proposed laser ultrasound imaging methodology is shown in Figure 3-9. The methodology consists of five major stages [30].

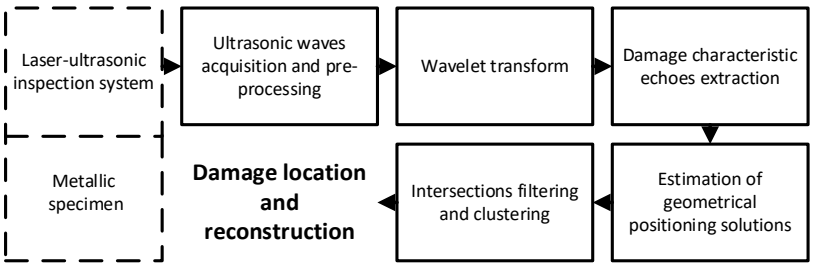

Figure 3-9: The sequence flow chart of the proposed laser ultrasound imaging methodology composed of five stages.

The first stage is the acquisition of ultrasound signals resulting from the thermal mechanism induced by each considered laser scan point over the specimen scan plane. In this stage, the acquired signals are digitally pre-processed by means of a bandpass filtering in order to increase the resulting signal to noise ratio in the frequency band of interest [30].

Second, the wavelet transform is computed for each time-based ultrasound signal. As aforementioned, a Morlet wavelet is proposed as a good trade-off between performance and simplicity [48]. Thus, it is expected that in the case of internal defect, additional wave fronts at shorter distances than those corresponding to the metallic specimen boundaries appear in the time-frequency response [30].

In the third stage of the proposed methodology, it is expected to automatically identify such ultrasound echoes corresponding to the presence of defect in the considered area of inspection. In this stage, a high-performing clustering algorithm, commonly used in image processing applications, is proposed in order to identify the time instant

of eventual ultrasound echoes over the resulting wavelet-based time-frequency maps.

The density-based spatial clustering of applications with noise (DBSCAN) [69,70] does not require previous knowledge of the number of clusters, which makes the technique suitable for dealing with multi-modal ultrasound signals represented in the time-frequency maps. For the purpose of DBSCAN, the time-frequency map points under analysis will be considered as core points, density-reachable ones, or outliers during the clustering procedure. In this regard, the DBSCAN requires only two main parameters, i.e., the distance ε corresponding to the maximum radius of the neighbourhood to be considered during the analysis of a point p, and the minimum number of points to consider a dense region, p_{min} [30].

As a result of this stage, the presence of characteristic damage echoes is detected through the clustering algorithm and its corresponding time is obtained from all scan points. The identified echoes, pertinent to the interaction between the ultrasound wave front and the defect, correspond to the sum of the *TOF* between the laser scan point to the defect and back to the ultrasound transducer.

In the fourth stage, we automatically identify the corresponding *TOF*s of the second detected group of echoes by detecting the time of the second cluster. For each resultant *TOF*, which corresponds to the sum of the individual *TOF*s from the laser to the defect and the individual *TOF*s from the defect point to the sensor, an ellipsoid is estimated, as a locus of defect location, which represents a set of possible geometrical solutions matching the computed *TOF*. An ellipsoid, by definition, is the locus of a point whose sum of displacement from the two well-determined points, the foci of the ellipsoid, is constant. Actually, the proposed method is based on the consideration of discretized three-dimensional curves resulting from the intersections of each pair of ellipsoids. From a

geometrical point of view, the embedded defect generating the corresponding time of flight is estimated to be at any point in such a curve. So, every point of the resulting curve is a potential locus of the defect. This continuous three-dimensional intersection curve, when discretized, is converted to points that become the locus of intersection. Thus, considering N ellipsoids generated by N different measurements resulting from N different scan points. A total number of intersections, I, considering any pair of ellipsoid intersection will be obtained, following:

$$I = N_{C_2} = \frac{N!}{2 \times (N-2)!} \qquad 3\text{-}3$$

Finally, the fifth stage proposes the identification of coherent intersections among the ellipsoids resulting from all laser scan point computations through a density analysis. In this stage, it must be noted that a previous filtering is proposed to reject the ellipsoids resulting from TOFs larger than the dimensions of the considered scan area. Then, the re-iterative intersections in the considered scan volume are projected in the XY scan plane, where the DB-scan technique is proposed to extract maximum density areas corresponding to a higher probability of defect location.

The analysis of the resulting set of ellipsoid intersections is proposed to be faced with the application of the DBSCAN-based clustering algorithm once more in our methodology. Then, the spatial localization of the defect is obtained by the geometrical centre calculation among the resulting clustered intersection points, and the defect reconstruction for visualization is carried out by means of the outline of the clustered intersection points.

3.2.2.2. Reconstruction of the defect

In this regard, the corresponding wavelet transform is carried out for each acquired ultrasound wave during the laser scan process using Morlet

mother wavelet for the scan area described in Figure 3-2. Some resulting time-frequency maps corresponding to ultrasound waves induced in the aluminium specimen at different laser scan points are shown in Figure 3-10. It shows how the first significant wavefront comes at the early stages due to the direct surface waves from the laser source to the ultrasound receiving sensor. Also, as mentioned above, the relative distance between the scan point to the object boundaries and back to the sensors is larger than that from the considered scan point to the defect and back to the sensor. So, the second group of detected ultrasound waves corresponds to echoes due to the existence of damage. The echoes corresponding to the boundaries are much more delayed as their distance is much larger. In this regard, Figure 3-10a shows the first wave front arrival, as indicated by circles on solid lines, at 8.8 μs. In Figure 3-10b, it is at 9.4 μs, in Figure 3-10c, it is at 10.9 μs and, in Figure 3-10d, it is at 9.5 μs. Similarly, a second wave front corresponding to the damage presence, as indicated by circles on dashed lines, appears in Figure 3-10a at 17.4 μs, in Figure 3-10b at 18.6 μs, in Figure 3-10c at 19.6 μs and, in Figure 3-10d at 20.2 μs. Such reflected waves correspond to characteristic damage ultrasound echoes and specifically their corresponding TOF are considered next to estimate the potential localizations of the defect position.

As an example, Figure 3-11 shows the ellipsoid resulting from the defect location estimation based on two measurements corresponding to different scan positions.

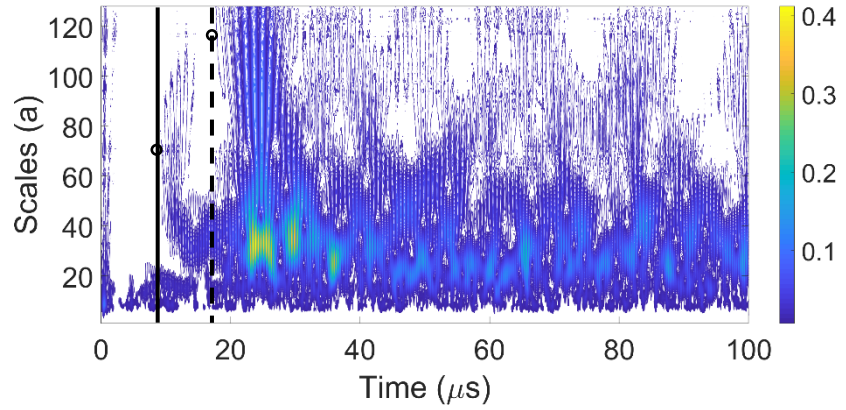
Scales (a)
120
100
80
60
40
20
0
20
40
60
80
100
Time (μs)
0.4
0.3
0.2
0.1

a)

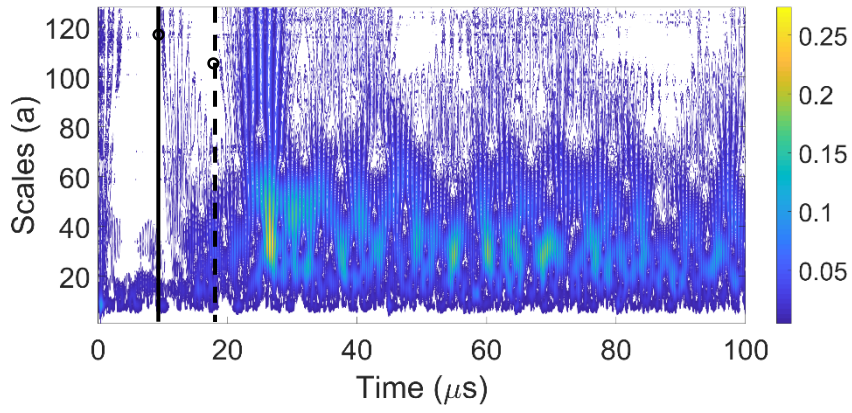
Scales (a)
120
100
80
60
40
20
0
20
40
60
80
100
Time (μs)
0.25
0.2
0.15
0.1
0.05

b)

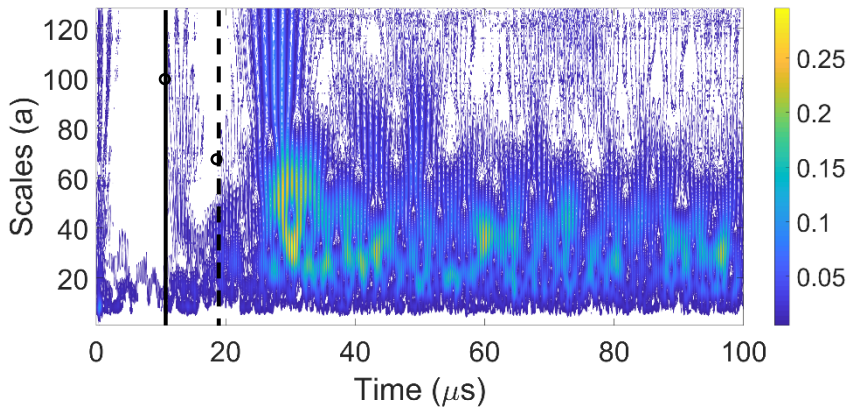
Scales (a)
120
100
80
60
40
20
0
20
40
60
80
100
Time (μs)
0.25
0.2
0.15
0.1
0.05

c)

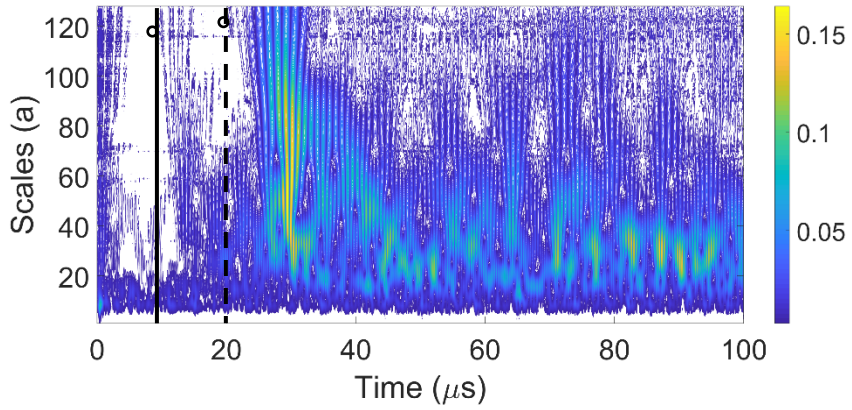

d)

Figure 3-10: Time-frequency maps of ultrasound waves induced at different scan points. The solid line represents direct ultrasound wave arrival, the dotted line, ultrasound defect-reflected echo arrival. The corresponding ultrasound transducer position is X = 15 mm and Y = 110 mm, and the positions of laser scan points are: (a) X = 11 mm and Y = 71 mm (b) X = 81 mm and Y = 51 mm. (c) X = 31 mm and Y = 41 mm. (d) X = 11 mm and Y = 51 mm.

Considering all 10 × 10 ellipsoid estimations the intersections among them correspond to potential locations where the interaction between the laser-generated ultrasound wave and the defect took place during the inspection. In this regard, Figure 3-11 shows the details related to the resulting intersection between the ellipsoids corresponding to the two scan points and the relevant *TOF* of the second echoes.

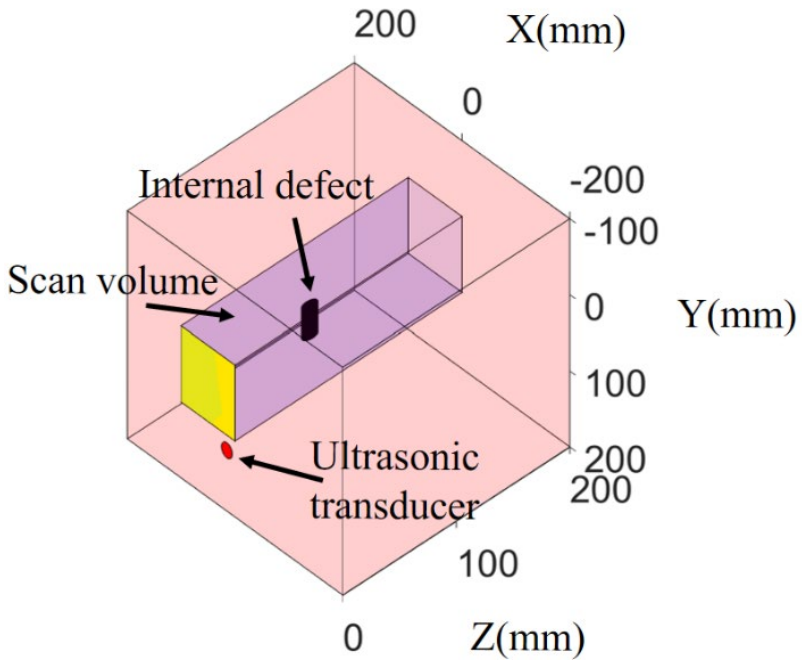
200
X(mm)
0
-200
-100
0
100
200
Y(mm)
200
100
0
Z(mm)
Internal defect
Scan volume
Ultrasonic
transducer

a)

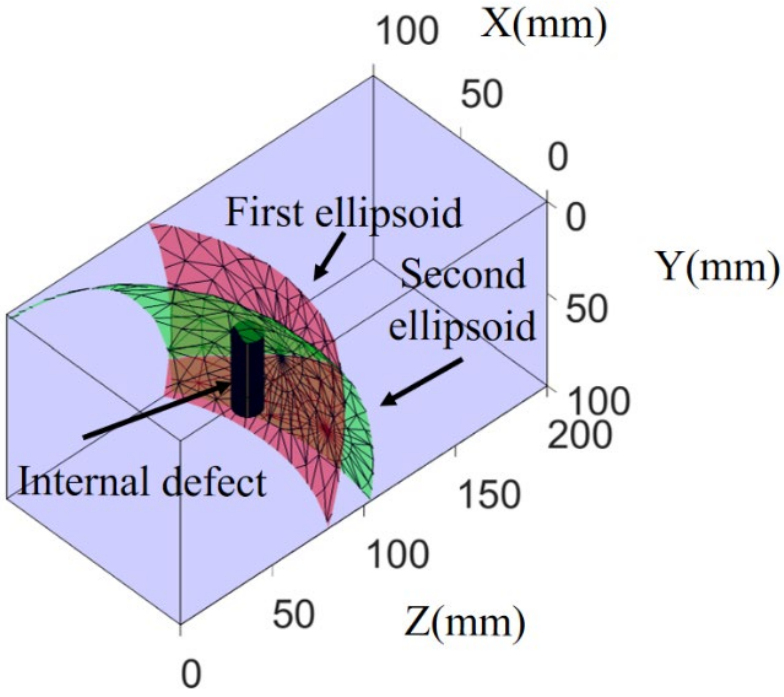
100
X(mm)
50
0
0
50
100
200
Y(mm)
150
100
50
0
Z(mm)
First ellipsoid
Second
ellipsoid
Internal defect

b)

Figure 3-11: Resulting ellipsoid intersections from two-second echo *TOF*s estimated during the proposed analysis of two laser-generated ultrasound waves experimentally measured. (a) Isometric view of the scan volume allocation. (b) Details of the scan volume and the intersection of two resulting ellipsoids and its coherence with regard to the defect position. The first ellipsoid results from the ultrasound transducer's position, scan point 1 position, and *TOF* equivalent to 17.4 mm. The second ellipsoid results from the ultrasound transducer's position scan point 2 position, and *TOF* equivalent to 18.6 mm.

Figure 3-12a shows the complete resulting intersections among all ellipsoids, where only a recurrent filtering is applied. The proposed application of the clustering algorithm, the DBSCAN, over such a resulting set of intersections results in a refined set as shown in Figure 3-12b, where the resulting intersections after the clustering analysis is presented.

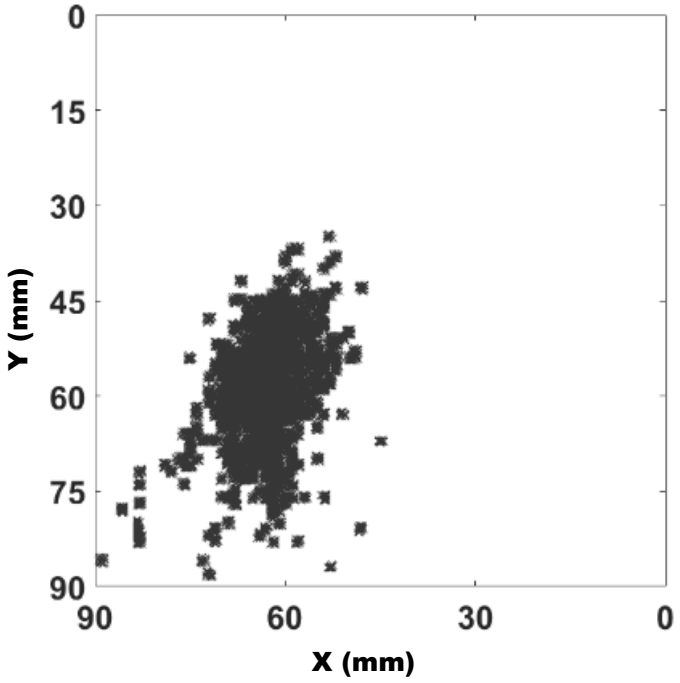

a)

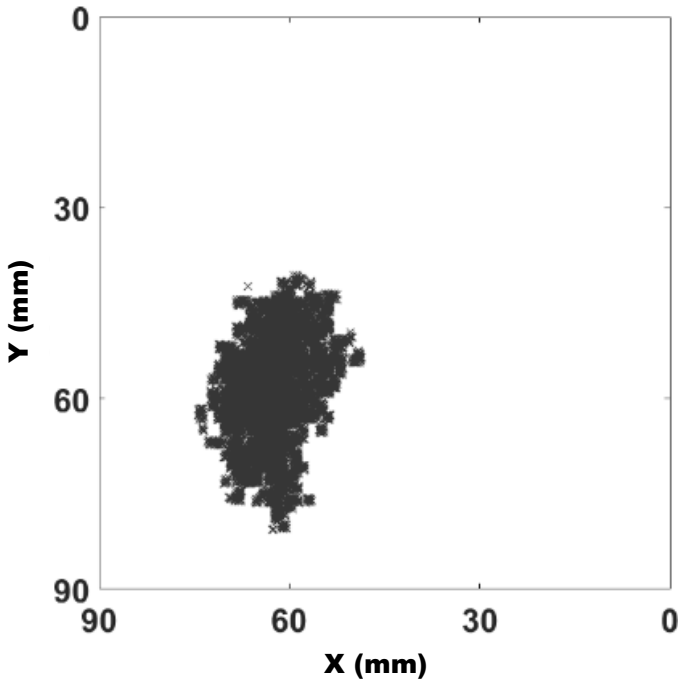

b)

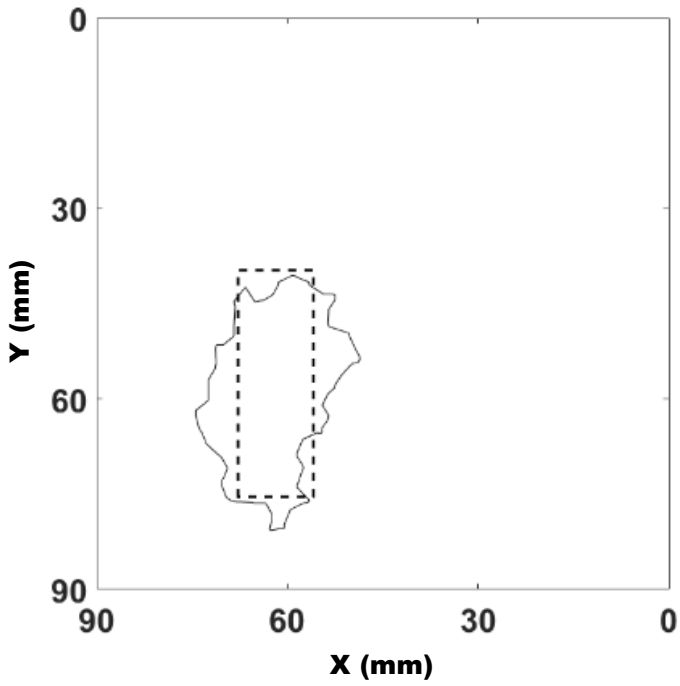

c)

Figure 3-12: The recurrent intersections set resulting from the ellipsoids analysis. (a) The raw set of recurrent ellipsoid intersections. (b) The clustered set of ellipsoid intersections. (c) The resulting defect reconstruction boundary with the superimposed actual cylindrical defect projection.

In Figure 3-12c, we only show the boundary of the resulting clustered set with the superposition of the actual defect location in order to compare the results with the exact position of the defect. The application of the proposed method results in a geometrical defect location estimation centred at $X = 62$ mm and $Y = 69.5$ mm, while the actual defect location centre is at $X = 61.5$ mm and $Y = 65$ mm, thus, revealing a positioning error of 4.53 mm. Considering the size of the defect, the proposed methodology results in an estimation of 578 mm^2, while the actual dimension of the defect's cross-section area is 520 mm^2, thus, resulting in an error of 11.1%.

3.3. Conclusions

This chapter presents a novel methodology to detect, quantify, and reconstruct internal defects on metallic samples based on laser-generated ultrasound. There are three important aspects of this new method. The first one is the ultrasound wave signal analysis through wavelet processing. The multi-resolution capabilities of the wavelet analysis allow the identification of the main ultrasound modes during the front wave propagation from the excitation point to the defect, and finally to the sensor; thus, enhancing characteristic echo detection for each point considered in the scan. The second is the extraction of characteristics of damage echoes and the methodological estimation of ellipses through the resulting time of flight for each laser excitation point. The third is the application of a clustering strategy as a processing stage in order to enhance the significance of the intersection analysis among ellipses. The application of the proposed clustering method over the resulting points of

intersection among ellipses allows the identification of the most coherent region and elimination of the less significant intersections. An internal defect at 95 mm from the surface of inspection is considered, which represents a challenging condition. Under such a scenario, the proposed methodology shows reliable fault diagnosis results, with a location and sizing error of 4.53 mm and 11.1%, respectively. The results obtained in this work suggest that this methodology may be also useful for further 3D imaging reconstruction of defects. However, the three-dimensional reconstruction will require a further analysis of multiple echo intersections in order to estimate the depth of the defect. The future work will focus on the analysis of the proposed laser ultrasound imaging method considering boundary interaction within the scan area.

Chapter 4. Two-dimensional scanning and three-dimensional defect reconstruction using contact transducers

In this chapter, the laser excitation performs a two-dimensional scan and we use two contact transducers, in a fixed position, for the ultrasound detection. We apply the SAFT algorithm for the signal processing that gives us enough information of the defect position and size for its 3D reconstruction The LGU scan is performed on different metallic objects and the receiving transducers are located at the same face of the objects where LGU excitation is performed, i.e. working in pitch-catch and reflection modes. We discuss two different experiments performed and the signal processing algorithms for defect reconstruction. Finally, we present an improved algorithm using apodization techniques that enhance the resolution of the reconstruction results [28,35].

4.1. Experimental setup configuration

We used same experimental configuration shown in section 2.1. We programmed our experimental setup, to perform a 2D scan over a MxN matrix points by remotely controlling the position of laser incident point

onto the object surface by a motorized galvanometer. The scanning area (in grey) as well as the position of the receivers (in yellow) in this experiment are shown in Figure 4-1. For each excitation point, each receiver records a corresponding A-scan signal. The experimental results combined with the SAFT technique are expected to give accurate information about the area of the defect for getting a precise 2D visualization of its location and dimensions [28,35].

Experimental measurements have been conducted in a pitch-catch mode, using two receivers placed at the fixed positions indicated in Figure 4-1. The laser has been programmed to scan an area of 92 mm x 83 mm, with 101 x 91 scan points.

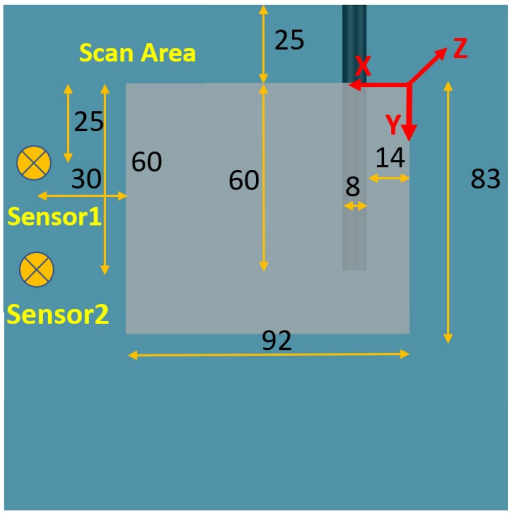

Figure 4-1: LGU scan area in grey for SAFT experiment and ultrasound sensors

4.2. Standard SAFT algorithm

4.2.1. Algorithm review

The standard SAFT algorithm is used under different conditions for the signal processing in the NDT technique for the detection of embedded defects. The analysis of the signal can be performed in the time or frequency domain. Different setup arrangements have been proposed, such as pulse-echo or pitch-catch modes. In the time domain analysis, based on the DAS methodology, the SAFT provides a focused image of the defect inside the object with a SNR higher than that of other techniques that rely mainly on fewer measurements to detect the presence of a defect. A specific approach needs to be considered to create a 3D reconstruction of a volume of interest in order to investigate a particular suspected embedded defect. In this regard, we propose the generation of multiple A-scan measurements at various points with predetermined spacing in both horizontal and vertical directions with high step resolution, creating a 2D scan area. Each A-scan signal comprises the superposition of the contribution of individual scatterers inside the volume of interest. Hence, each time instant on the time axis of the A-scan signal is represented by a specific amplitude corresponding to the influence of scatterers that lie inside the active volume at a similar *TOF* equivalent to their distance from the exciter-receiver, respectively.

For an arbitrary excitation point, *T*, that generates an ultrasound wave propagating in the volume and an arbitrary receiver, *R*, which detects the reflected signal by the volume points, one of which is the point of interest, *P*, we can define the *TOF* of the signal as [36,106,107]:

$$TOF_{(i,j,k)P} = \frac{|\vec{d}_{(i,j,k)P} - \vec{d}_{(i,j,z)T}| + |\vec{d}_{(i,j,k)P} - \vec{d}_{(i,j,z)R}|}{c} \quad 4\text{-}1$$

where the *TOF* is the time-of-flight of the ultrasound signal generated by the exciter *T*, scattered from the point *P* and detected by the receiver *R*; $\vec{d}$ is the displacement vector at positions *T*, *R*, and *P*, respectively; *i*, *j*, and *k* represent the indexes of the volume image points in the *X*, *Y*, and *Z* planes respectively; and c denotes the longitudinal speed of sound in the material of the object.

Shifting the position of the exciter/receiver results in a different *TOF* for the same particular scatterer in the active volume and a different amplitude at the corresponding time instant at the A-scan signal. The summation of all these amplitudes with respect to their *TOF*'s (Equation 4-2) will generate a focused image, $y_f(p)$, of that scatter with an overall amplitude corresponding to all scan points in the 2D scan area.

$$y_f(P) = \sum_{j=1}^{N} \sum_{i=1}^{M} y_r(TOF_{(i,j,k)_P}, i, j) \qquad 4\text{-}2$$

where y_r is a preliminary unfocused image of this particular point *P*, y_f is the high-resolution focused image; and *M***N* are total scan points in horizontal and vertical directions of the scan area. We note that Equation 4-2 does not take into account the nature of propagating ultrasound in the solid object, which mostly contains main and side lobes at different angles and intensities.

4.2.2. Results and discussion

The signals captured by the two sensors have been recorded using the aforementioned amplifier and data acquisition system and were pre-processed using a bandpass filter and an interpolation algorithm to remove the background noise and low/high frequency components. We also applied an averaging algorithm on multi-captured signals at each

scan point (10 signals) to remove the DC components and reduce the noise effect from the acquired signal.

As a result, we obtain in Figure 4-2 the volume reconstruction of the selected scanned area for SAFT analysis for signals received by both sensors where the defect corresponds to the yellow shadows.

The position and dimensions of the defect can be better visualized and measured if we select projections of different cross-sections in the volume of interest, that can be extracted from Figure 4-2a for any required coordinates. Figure 4-2b and Figure 4-2c show two cross-section slices in the *XY* and *XZ* planes respectively. From these projections we measure a defect with horizontal ΔX size of 8.2 mm and vertical ΔY size of 56 mm [28].

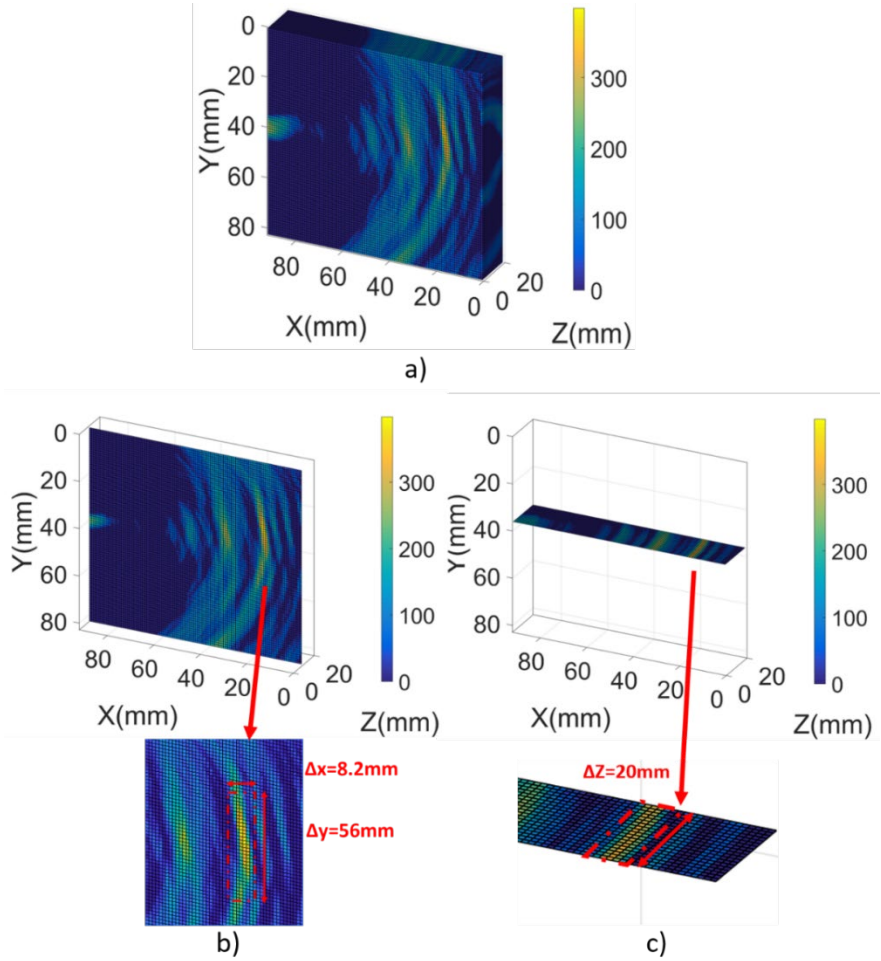

Figure 4-2: Reconstruction results of SAFT technique for a) 3D volume representation b) 3D slice for XY plane c) 3D slice for XZ plane.

The contour map of one of the cross-sections is another representation of the results that can even better visualize the defect. Figure 4-3 shows the contour map of the *XY* cross-section, enabling the reconstruction of the *X* and *Y* dimensions: the defect is centred at *X*=17.5 mm and *Y*=40 mm with the corresponding size ΔX=8.2 mm and ΔY=56 mm. Compared with the real size and position of the defect in our sample, the resulting reconstruction has the following errors: a sizing error of 4.6%, concretely, ΔX_{error}=2.5% and ΔY_{error} =6.7% and a positioning error of

12.25%, concretely, X_{error} =2.5% and Y_{error} =22%. There are several reflections in the resulting images that do not come from the defect, that could be misleading. The contour map helped to identify and ignore them. These reflections can be overcome in further experiments.

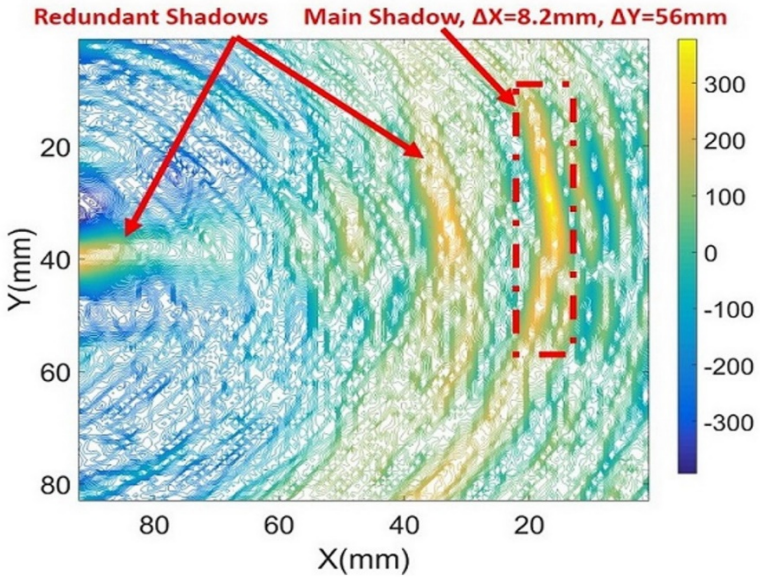

Figure 4-3: a) Contour map of the defect at XY plane at Z=10 mm using SAFT technique.

The reflections appearing in the reconstructed images, as well as the resolution of the reconstruction are conditioned by some aspects of our experiment. On one hand, Z-dimension of the object studied here was too small compared with X and Y ones. In other words, the distance between the laser/sensor and defect is larger than the one to the Z boundaries of the object itself. This results in multiple reflections which arrive to the receiver faster than those coming from the defect, leading to misleading wavefronts that produce some errors in the reconstructed results. To solve this problem, Z dimension of the object under test should be large enough to avoid internal reflections from the boundaries. This applies to all object boundaries in all directions. On the other hand, in our experiment we fixed the position of the receiving sensors and only scanned the laser

impact points. This change in laser scan point position results in a change in the angle between the excitation point and the ultrasound receiving sensor. This angle at certain points of scan increases significantly due to object geometry. Large angles reduce the performance of the SAFT technique and can significantly reduce the signal-to-noise ratio. In addition, side lobes of the LGU could add other shadows to the reconstructed images. These constraints can be resolved by increasing the object's depth and reducing the angle by scanning the receivers along with the laser beam. On the other hand, we can improve SAFT algorithm results by applying a 2D apodization technique that can reduce the redundant shadows as described later on.

The reason we did not add more receivers (e.g: microphone array) is that our main focus is to use the transmitter, not the receiver, as the scanning mechanism with a lot of points with high step resolution. With laser excitation, we can do the scanning of the transmitter with a step size of 0.9mm for more than 9000 scan points. This is very difficult to achieve with conventional arrays. In addition, the scanning with the laser makes the incident pulse on the object surface equivalent to a point source, which is better for the SAFT efficiency.

Figure 4-4a and Figure 4-4c show the results of using only receiver sensor 1, while Figure 4-4b and Figure 4-4d show the results of using only sensor 2. For the mentioned figures, we show the volumetric results as well as the contour results respectively. It is clear that using only one sensor is giving limited amount of information in the image. Using the other sensor is giving another portion of the information. Combining both sensors together gives a much better result and clearer information. Comparing the results in Figure 4-4 with the results of Figure 4-2 and Figure 4-3 shows that when we use the two sensors, we get better results that include more details about the defect form different perspectives.

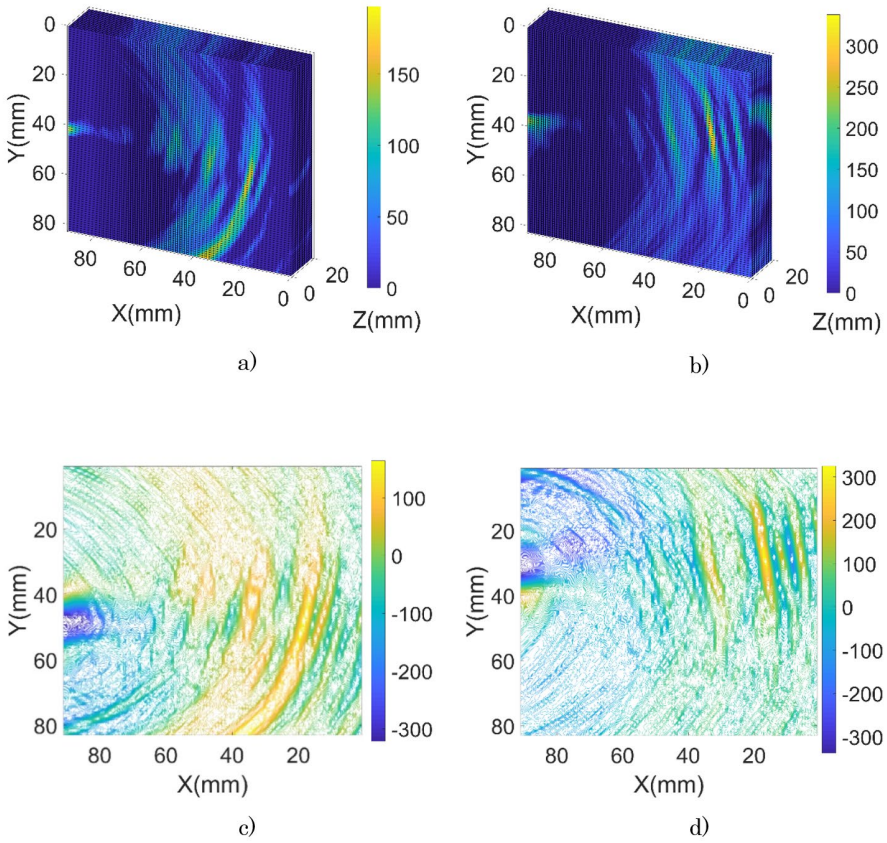

Figure 4-4: results of SAFT algorithm when using only one receiving sensor instead of the 2 receiving sensors used in Figure 4-2 and Figure 4-3 a) Volume view using sensor 1 b) volume view using sensor 2 c) contour view using sensor 1 d) contour view using sensor 2.

4.3. Improved SAFT analysis using 2D apodization

4.3.1. Development of 2D apodization Algorithm

The above-mentioned discussion referred to the standard SAFT algorithm methodology. Here we discuss our improved approach for the same experiment where we propose the use of the apodization function to

enhance the resulting image by weighing the amplitudes resulting from the propagation of side lobes that can produce secondary echoes that influence and distort the main echoes generated by the scatterers as described by Equation 4-3 which is an improved version of Equation 4-2:

$$y_f(P) = \sum_{j=1}^{N}\sum_{i=1}^{M} a(TOF_{(i,j)_P}, i, j) * y_r(TOF_{(i,j,k)_P}, i, j) \qquad 4\text{-}3$$

where $a(TOF_{(i,j,k)_p}, i, j)$ is the weighing or apodization function [108]. Equation 4-3 represents the above idea of DAS, where the summation is applied to the delayed versions of the signals at the corresponding scan points. The apodization function is generally chosen to approach zero at the edges of the SA window edges [51].

In the SAFT analysis, if the scan is performed in a line of scan to generate a reconstruction image in a 2D plane, i.e., scan in one line and inspection of the depth of the object in the plane containing that line, we use a 1D apodization window that represents the aperture line at each point of the scatterers in the cross-section depth of the object. This approach is well-known in the literature [51,52,109,110]. We propose an improvement to this approach by extending this apodization to the 3D case. When the SAFT scan is performed in a 2D area to perform a 3D reconstruction image, the aperture of the apodization window also becomes a 2D area. To make it clearer, the dimension of the apodization window is the same as the dimension of the scan line/area, as it depends on the position of the scan sensors.

To clarify the meaning of the apodization function we first describe this concept in the commonly used case of a 1D scan line on X-axis and scatter plane XZ. Later we will expand the discussion to the general case of 2D scan area and scatterer volume. The expansion to a 2D apodization window has been previously discussed [52]. However, to date, and to our knowledge, it has not been used for SAFT analysis.

For a 1D scan line X-axis and point scatterers in a plane XZ, the width of the apodization function should be proportional to the depth of the scatter point (Figure 4-5) and it is denoted by Equation 4-4 below [51].

$$\Delta X(Z) = 2Z\tan(\Delta\theta_X / 2) \tag{4-4}$$

Where $\Delta X(Z)$ is the width of the apodization window, Z is the depth of the point scatter, and $\Delta\theta$ is the angular beam width of the transducer and can be calculated at −6dB based on Equation 4-5 [51,111]:

$$\sin(\Delta\theta_X / 2) = 0.514 * \frac{c}{fD} \tag{4-5}$$

where f is the central frequency and D is the diameter of the transducer.

The apodization function can be applied to all points falling within a certain normalized X coordinate, $\hat{X}$, and neglecting all other measurements outside this threshold (Equation 4-6).

$$\hat{X} = \frac{X - X'}{\Delta X(Z)} \tag{4-6}$$

where X–X' is the horizontal shift between the position of the scan point and scatterer.

The most commonly used apodization functions are the rectangular or Hanning function [51]. Equation 4-7 and Equation 4-8 represent the apodization functions $a(\hat{X})$ for rectangular and Hanning windows, respectively, for a 1D scan line on the X-axis [51,52].

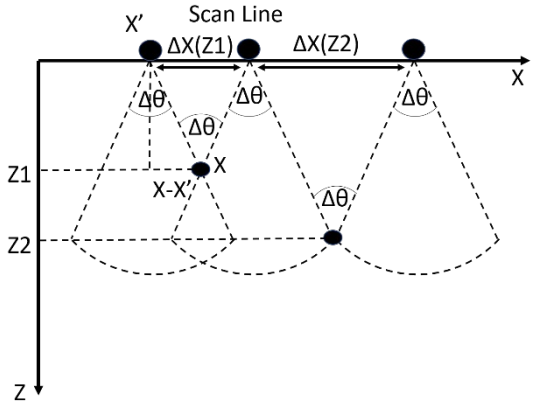

Figure 4-5: Beamwidth angle $\Delta\theta$ for a point scatterer at depth *Z;* when the point scatterer is deeper *Z2 > Z1,* the synthetic aperture size (ΔX) changes accordingly. The apodization window size should be adapted to the synthetic aperture window size.

$$a(\hat{X})_{rect} = \begin{cases} 1, & \left|\hat{X}\right| < \alpha \\ 0, & otherwise \end{cases} \qquad 4\text{-}7$$

$$a(\hat{X})_{Hann} = \begin{cases} 0.5[1+\cos(\frac{\pi}{\alpha}\hat{X})], & \left|\hat{X}\right| < \alpha \\ 0, & otherwise \end{cases} \qquad 4\text{-}8$$

Optimum results are obtained by fine-tuning the threshold criterion value, *α.* In order to apply the same apodization function to the entire volume with a 2D scan area, we require that the beamwidth angle become a solid angle instead of a planar angle. To make it simpler, we will have two angles $\Delta\theta_X, \Delta\theta_Y$ corresponding to the scan area *XY* instead of the scan line *X.* In this case, we deal with the apodization function $a(\hat{r}) = a(\hat{X}, \hat{Y})$ as a separable function (i.e., we can calculate the two-dimensional function by considering a series of one-dimensional functions) [52]. Hence, the one-dimensional window functions in Equation **4-7** and Equation 4-8 can be transformed into the two dimensional window functions in Equations 4-9 and 4-10:

$$a(\hat{r})_{rect} = \begin{cases} 1, & |\hat{r}| < \alpha \\ 0, & otherwise \end{cases} \quad 4\text{-}9$$

$$a(\hat{r})_{Hann} = \begin{cases} 0.5[1+\cos(\frac{\pi}{\alpha}\hat{r})], & |\hat{r}| < \alpha \\ 0, & otherwise \end{cases} \quad 4\text{-}10$$

where $\hat{r} = \sqrt{\hat{X}^2 + \hat{Y}^2}$ with the introduction of $\hat{Y}$ as the normalized Y coordinate $\hat{Y} = \frac{Y - Y'}{\Delta Y(Z)}$ and $\Delta Y(Z) = 2Z\tan(\Delta\theta_Y / 2)$.

With this generalized case, it is possible to apply the 2D apodization window function to the scan area of interest that covers the volume of interest.

In the derivation of the final image reconstruction using the SAFT technique, it is assumed that the ultrasound transmitter is small enough to be considered as a point source, which is applicable in the case of LGU. Receivers also need to be regarded as point-like transducers, i.e., the smaller the size of the transducer, the smaller the numerical error in the algorithm.

An important constraint to this algorithm is the limited angle between transmitter and receiver. Typically, this should not be large to avoid diffraction and side lobes. To avoid calculation error, another important constraint is that the dimensions of the object should allow the transmitter scan area and the receiver locations to be far from the object's boundaries to avoid their reflections. Another constraint of the SAFT algorithm is that it can work with ultrasound signals propagating at a single velocity. Thus, composite or inhomogeneous materials that display dispersion violate the SAFT algorithm, unless the different wave velocities and diffraction are taken into account.

4.3.2. Results and discussion

The apodization function *a(TOF(i,j,k)p,i,j)* in Equation 4-3 was not yet used in the previous SAFT analysis in 4.2.2. Its implementation in the algorithm removes the redundant shadows appearing in the reconstructed images shown in Figure 4-2 and Figure 4-3. First of all, we applied a narrow bandpass filter with cut off frequencies (1MHz to 2.5MHz) to the directly captured A-scan raw data as a pre-processing filter before applying the SAFT algorithm. We then included the apodization function at Equation 4-3 which adds weights to the summation of the recorded signals at specific times of light in order to magnify the effect of the signals within the apodization window and eliminate those falling outside the window limits [28,34,51,52,109,110]. 1D apodization function is used when a line scan is executed, as described in the literature. Here in our case where an area scan is used of a line scan, the apodization window needs to get expanded as well from a line to an area. The 2D expansion has been applied to improve the apodization algorithm from the traditional 1D approach known in the literature to the general 2D approach. The size of the apodization function needs to change with respect to the depth of the scatterer points in the scan volume to cover the synthetic aperture area.

we use the Hann window with a threshold criterion α= 0.8 after proper fine tuning that provided the optimum signal to noise ratio and enhanced the resulting reconstructed image with no redundant shadows.

Applying this apodization function at all point scatterers, we can find the resulting reconstructed image as in Figure 4-6a, where one can note that all the redundant shadows have been eliminated and only the main shadow appears, with a high signal quality. The contour map in Figure 4-6b emphasizes this effect showing only the contour lines of the main shadow. The apodization function clearly improves the reconstructed defect image in comparison with the results shown in Figure 4-2 and

Figure 4-3. The defect is centred at X=17.5 mm, Y=30 mm and Z=10mm with the corresponding size ΔX=8.2 mm and ΔY=37 mm. Compared with the real size and position of the defect in our sample, the resulting reconstruction has the following size errors ΔX_{error}=2.5% and ΔY_{error}=38% and position errors X_{error}=2.5% and Y_{error}=0%.We obtain an improvement in the position error, while the size error increased slightly but still remains within satisfactory limits. The results we obtained with the 2D apodization function added a power to the SAFT algorithm with enhanced results overcoming the challenging constraints of the experimental configuration.

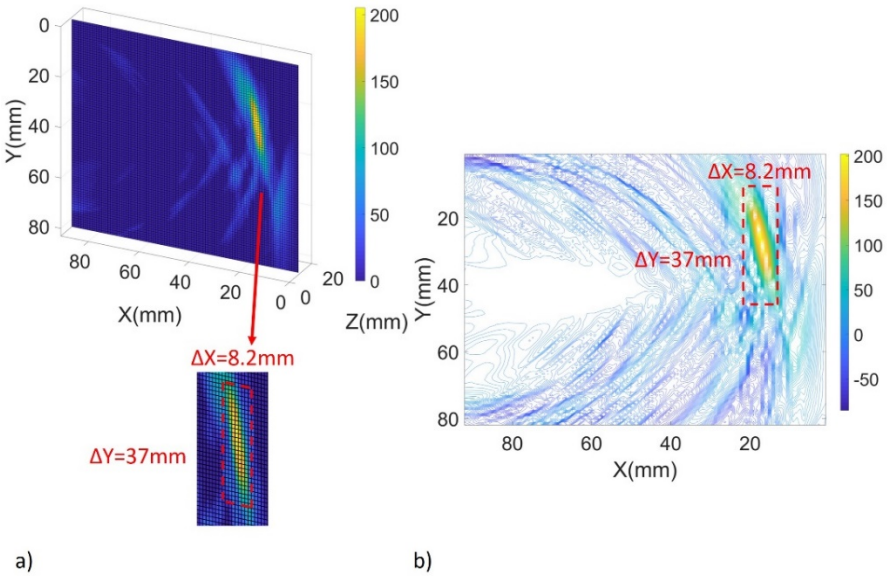

Figure 4-6: Reconstruction of the defect using improved SAFT technique after applying narrow band-pass frequency filter and 2D apodization function a)3D slice for XY plane b)slice Contour map of the defect at XY plane at Z=10 mm.

The implementation of the 2D scanning area and the signal processing using the SAFT technique over the object's volume allows the defect visualization from different angles and at different depths, making possible a 3D image reconstruction. For this application laser generated ultrasound excitation is much easier to implement than scanning with

conventional transducers as it can be applied and scanned remotely and therefore the volume in which the ultrasound is generated is smaller. In the experiment presented here we scanned the laser across *MxN* points, and we used only two fixed ultrasound receivers. This helped make the scan easier and show that by increasing the number of exciters (laser scan points in our case), we can obtain the same good-quality images with a very limited number of receivers fixed at particular points.

SAFT technique is sensitive to defects in agreement with the size of the measuring transducers. It is able to detect and reconstruct 3D defects at relatively large angles despite the corresponding errors. The position of the sensor and scan points do not need strict rules as long as the angle is within the allowable limits and the scan points as well as the sensors are at a relatively far distance from the boundaries of the object. The resolution of the reconstruction is in a range between those of the classical ultrasound and the full optical methods. The algorithm is having a very high signal-to-noise ratio of the defects relative to other techniques.

4.4. A cube test object (two contact transducers)

4.4.1. Experimental setup configuration

As aforementioned, the dimensions of the object and the position of the scanning transmitter/receiver devices affect the results of the SAFT reconstruction, and this is a limitation of the algorithm. We applied a different experiment to another cube object with higher depth to overcome the problem of boundary reflections and sidelobe propagating waves. In addition, we made the defect completely buried inside the cube object. The experiment was performed using same setup configuration we discussed earlier in sections 2.1 and 4.1 on a cubic sample with side length of 150mm made of cast aluminium with an embedded glass cylinder impurity buried

in the cube structure to represent the embedded defect. The embedded impurity of glass cylinder has a diameter of 13mm, a height of 80mm and buried at a depth of 100mm in the Z dimension. The sample has got a scan area of 90x90 mm as shown in Figure 4-7 with a number of scan points of 100 *100 in the X and Y directions respectively. we used the same exciter, receivers, scanning galvanometer and data acquisition tools as in the previous experiment with the thin cuboid sample described in chapter 2. the two receivers were placed below the scan area. The position of the defect is shown as well in Figure 4-7.

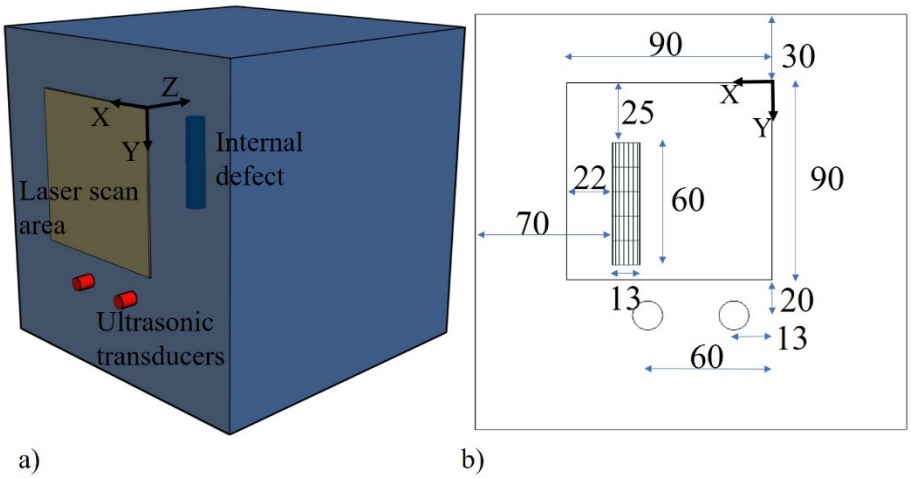

Figure 4-7: Schematic diagram of experimental configuration for SAFT analysis for cube object a) 3D volume representation b) Front view of scan area (XY plane)

4.4.2. Results and discussion

In the signal processing we used the SAFT algorithm without using the 2D apodization improvement technique. The results of the experiment in Figure 4-8 show the calculated defect location at positions corresponding to the higher signal amplitude in the shown figures.

There are a lot of factors that helped get better results with better signal quality. It can be seen that the results show the exact projections

of the defect with a good SNR. It can be shown clearly that only the defect shadow appears in the reconstruction image. There is no redundant shadows due to the consideration of the angle of the exciter/receiver and the reduced boundary effects due to larger depth of the object. Also, the side lobe effect of the laser-generated ultrasound is not affecting the reconstructed image due to the small angle between exciters and receivers at deep Z planes. All these factors provided better reconstruction of the defect as compared to the previous case of thin cuboid.

Figure 4-8a shows the whole SAFT volumetric image of the object, it does not show any defect at the outer surfaces of the volume as the defect is embedded inside and it should not have any significant effect on the ultrasound propagation near the surface. Figure 4-8b and Figure 4-8c show two cross-section slices in the XY and XZ planes respectively with insets showing the exact reconstructed defect dimensions in both planes.

The contour map in Figure 4-9 shows clearly the contour lines of points with highest intensities corresponding to defect. And again, there is only one shadow corresponding to the defect, and there are no redundant shadows as is the case of thin cuboid.

It is shown that we have a defect in the XZ plane from X=59 to 76 mm (ΔX=17mm) and from Z=92 to 101 mm (ΔZ=9 mm) and at XY plane from Y=31 to 79 mm (ΔY=48mm) around same positions. Comparing these results with actual hole size of 13mm diameter by 60mm length and with scan area dimensions in Figure 4-7 results in ΔX_{error}=30%, ΔY_{error}=20%, ΔZ_{error}=30% and the Positioning error in this case is X_{error}=6%, Y_{error}=0%, Z_{error}=3% in the three dimensions.

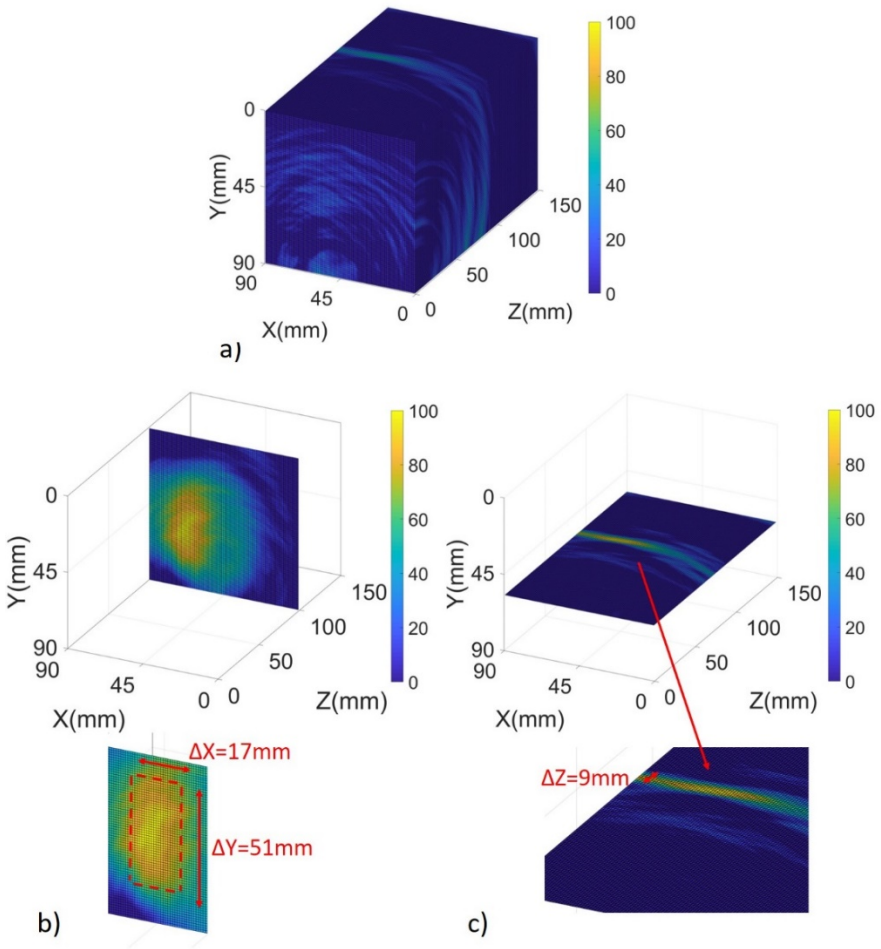

Figure 4-8: Reconstruction results of SAFT technique for the cube object with insets to show reconstructed defect dimensions a) 3D volume representation b) 3D slice for *XY* plane c) 3D slice for *XZ* plane.

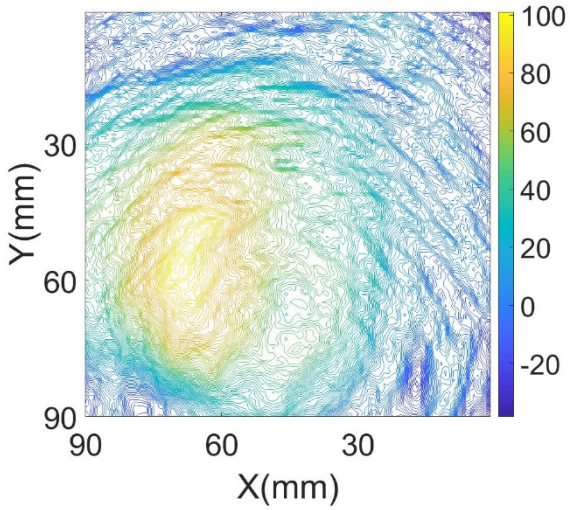

Figure 4-9: Contour map of the defect at the cube object at *XY* plane at *Z*=97 mm using SAFT technique.

4.5. Conclusions

The SAFT technique and the improved SAFT technique with 2D apodization function, indicate similar position of the defect, confirming the reliability of the algorithms. The implementation of the 2D scanning area and the signal processing using the SAFT technique over the object's volume allows the defect visualization from different angles and at different depths, making possible a 3D image reconstruction. We used the discussed algorithms to localize the defect position with a good signal-to-noise ratio, taking into consideration the limitations of structural dimensions. The resolution of the reconstruction is in a range between those of the classical ultrasound and the full optical methods. Boundary reflections, side lobes of the laser generated ultrasound and angle between exciters and receivers influence the quality of the resulting reconstructed image of the defect. When considered carefully, using 2D apodization function, the redundant shadows are removed and only the

main shadow corresponding to the defect is generated with size error ΔX_{error}=30%, ΔY_{error}=20%, ΔZ_{error}=30% and the Positioning error in this case is X_{error}=6%, Y_{error}=0%, Z_{error}=3% in the three dimensions. We believe that this hybrid approach combines different advantages of both photonic and ultrasound devices, reducing the drawbacks of both methods. The remote control of the broad band excitation, possibility of scanning large areas and reduced number of receivers make it easy to implement for different materials and applications.

Chapter 5. Fully noncontact hybrid NDT for 3D defect reconstruction using SAFT algorithm and 2D apodization window

In this chapter we present and discuss our last NDT experiment where we succeed to obtain a 3D reconstruction of an embedded defect using a fully non-contact approach, where both excitation and detection is contactless We use the a hybrid system similar to that presented in Chapter 4 (see Figure 4-7), but here we replace the fixed contact transducers with a noncontact one, whose position can be scanned as well as the Laser [34]. We use a different cast aluminium cube as the object under test with a solid glass object embedded internally representing the defect under investigation. The laser is programmed to scan 3 orthogonal faces of the cube with 2D scanning areas of 90 x90 mm^2 covering 100 x 100 points at each face of the object. The scanning is performed using an automated 2D *XY* motor stage. The laser beam as well as the detector are positioned on the same *XY* motor stage and they move together with a fixed relative distance between both of them.

We apply SAFT analysis as a continuation to the previous SAFT study. This chapter includes some improvement in the hardware setup and signal processing algorithm. Main enhancements are due to the fact that the detector is also scanned along with the laser exciter, and with the same relative distance. The close and fixed distance between laser and detector in such configuration makes the measurements more accurate with less attenuation and more detection sensitivity. The use of non-contact transducer also makes it completely remote excitation/detection configuration less subject to environmental vibrations/alterations or coupling variation between subsequent measurements eliminating greatly their error in the final result. In addition, the small angle between both exciter and receiver in all the scanning steps makes SAFT results more accurate.

5.1. Experimental setup configuration

We use a similar set-up as the one described in Chapter 4, with the difference that now we implement a non-contact transduces as detector recording the ultrasound at a certain distance from the object surface [34]. This configuration allows us to scan more than one face of the cube. The system, schematically shown in Figure 5-1, is automatized to record data from the excitation scan on 3 orthogonal faces of the cube. The detector moves simultaneously with the laser head. The experiment provides simultaneously information of the defect position and size from different view angles and perspectives as shown in Figure 5-1. The schematic representation of our experimental setup and of the object under study is shown in Figure 5-1a. The experiment was performed on a cubic sample with side length of 150 mm made of cast aluminium, with an embedded glass cylinder buried in the cube structure, representing the embedded defect. The cylinder has a 13 mm diameter and a 60 mm height and is positioned vertically inside the cube. The defect was embedded at a depth of 100 mm from the front and side faces (face 1 and 2 in Figure 5-1b) and

70 mm from the top view of the cube (face 3 in Figure 5-1b). Scanning procedure using SAFT algorithm is shown in Figure 5-1c. Figure 5-1b also shows the scan areas of 90 × 90 mm² at three faces of the cube, with scan points distributed equally in the *XY* planes of the three faces. Note that for simplicity each face has its own *XYZ* coordinate system. Figure 5-1c shows the schematic representation of the 3D object under investigation with the scanning area at one of the faces with the positions of the Exciter (T), Receiver (R), and scatterer point in volume.

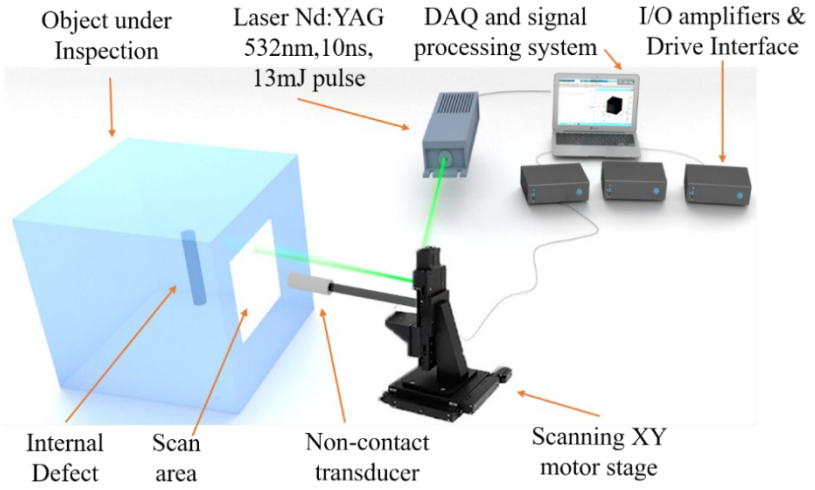

(a)

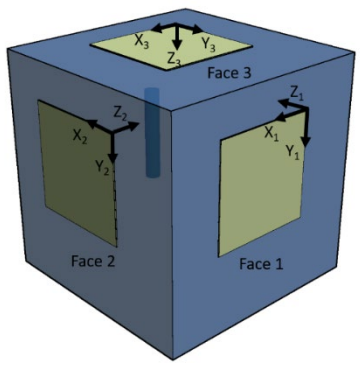

(b)

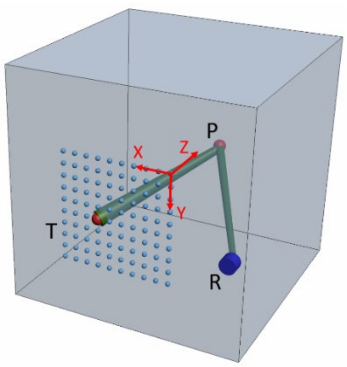

(c)

Figure 5-1:a) Experimental setup used for the excitation and detection of ultrasound waves; b) Schematic representation of the object under study with the three-face scan areas. Different Cartesian axes are represented at each scan face; c) Representation

of the 3D object under investigation using the synthetic aperture focusing technique (SAFT) algorithm with the scanning area at one of the faces with the Exciter (T), Receiver (R), and scatterer point in volume.

In the experiment, we replace the scanning galvanometer used in previous chapters with an *XY* motorized stage (OSMS CS 26-100X-M6 and OSMS26-100 Z -M6 with controllers HIT_M and HIT-S from manufacturer Optosigma) as the scanning mechanism that holds the laser focusing lens and a non-contact transducer (NCT2-D3 from Ultran Group) with a nominal frequency of 2 MHz as the receiver with the same data acquisition system. The reconstruction of the defect gets improved when using this new hardware configuration for better 3D reconstruction of the defect as can be seen later in this chapter.

Software based on LabVIEW and MATLAB was programmed to control the *XY* motorized stage and to define the scanning areas and the number of scan points. the noncontact transducer was fixed to the same *XY* motorized stage that controls the position of the laser beam spot at a fixed vertical spacing of 17 mm from the laser spot as shown in Figure 5-1a. The exciter and receiver move together in the scanning area. The transducer was placed at a fixed distance of 8.5 mm air gap from the object surface.

5.2. Results and discussions

In this signal processing analysis, we used the 2D apodization improvement technique discussed in section 4.3.1 [34]. We performed both excitation and detection scan over the three faces of the cube as shown in Figure 5-1b in order to obtain detailed information of the embedded defect at different perspectives/angles that are needed for the 3D reconstruction. The captured signals were first subject to the signal conditioning algorithm to obtain a higher quality signal. The algorithm involved

filtering and interpolation of the measured signals to remove noise and low/high frequency components that are of no interest. Additionally, we subtracted the noise signal from the main signals to remove background effect. An averaging algorithm (10 signals) was also implemented to remove DC components, signal noise and offsets in the measured signals. The SAFT algorithm was then applied to all signals coming from the three faces scan areas. It should be noted that a 25 μs time delay is added to the TOF values extracted from Equation 1-21 [112]. This delay is equivalent to the velocity of ultrasound exiting the object cube at 340 m/s and travelling through the airgap of 8.5 mm towards the transducer. The 2D Hanning window apodization function was applied to the SAFT algorithm by considering the threshold criterion $\alpha = 0.5$. This value is applied by substitution in Equation 4-10. Any value of $\hat{r} > 0.5$ was rejected and equal to zero. The calculation is applied for each specific point scatterer in the volume with respect to all exciter and receiver positions. The result is substituted in Equation 4-3 for each point scatterer to apply the weighting to the SAFT image. We used the same criterion as validated and investigated in [51], so that cancellation of sidelobes is achieved [51,52]. The beamwidth is frequency-dependent, and the width of the apodization function cannot match the beamwidth for all frequencies within the transducer passband. To cover the complete synthetic aperture, the apodization function must be tuned to the beamwidth by taking into account the lower edge frequency of the bandpass filter [51]. Note that a narrow apodization window increases the amplitude of the main lobe echoes, but also increases the side lobe effects and their redundant shadows, while a wider apodization window reduces sidelobe effects but at same time distorts the focusing of the main lobe and reduces the focusing amplitude [51,52]. The selection of the optimum value of the threshold is subject to a tuning process. We applied fine-tuning of the value of threshold value between 0.3 and 0.9. The best results were obtained at a value of 0.5 similar to [51,52]. Fine-tuning is applied to optimally select the 25-μs time delay corresponding to the airgap effect.

The results of our full noncontact experiment for each scan area are shown in Figure 5-2 [34]. The defect is located and represented for each scan face at positions corresponding to the larger signal amplitude shown in the figures. The Cartesian axes *X*, *Y*, and *Z* are chosen for each face to cover only the respective scanned area and have their origin at the top right corner, with *XY* being the scanned area plane and the *Z* axis is perpendicular to this area. The axes for each face are denoted by X_1, Y_1, and Z_1 (face 1); X_2, Y_2, and Z_2 (face 2); and X_3, Y_3, and Z_3 (face 3), respectively. The results in Figure 5-2 are represented at *XY* and *XZ* cross-sections respectively for the three faces. The colour map at right hand side of Figure 5-2f represents the amplitude percentage and applies to all subfigures.

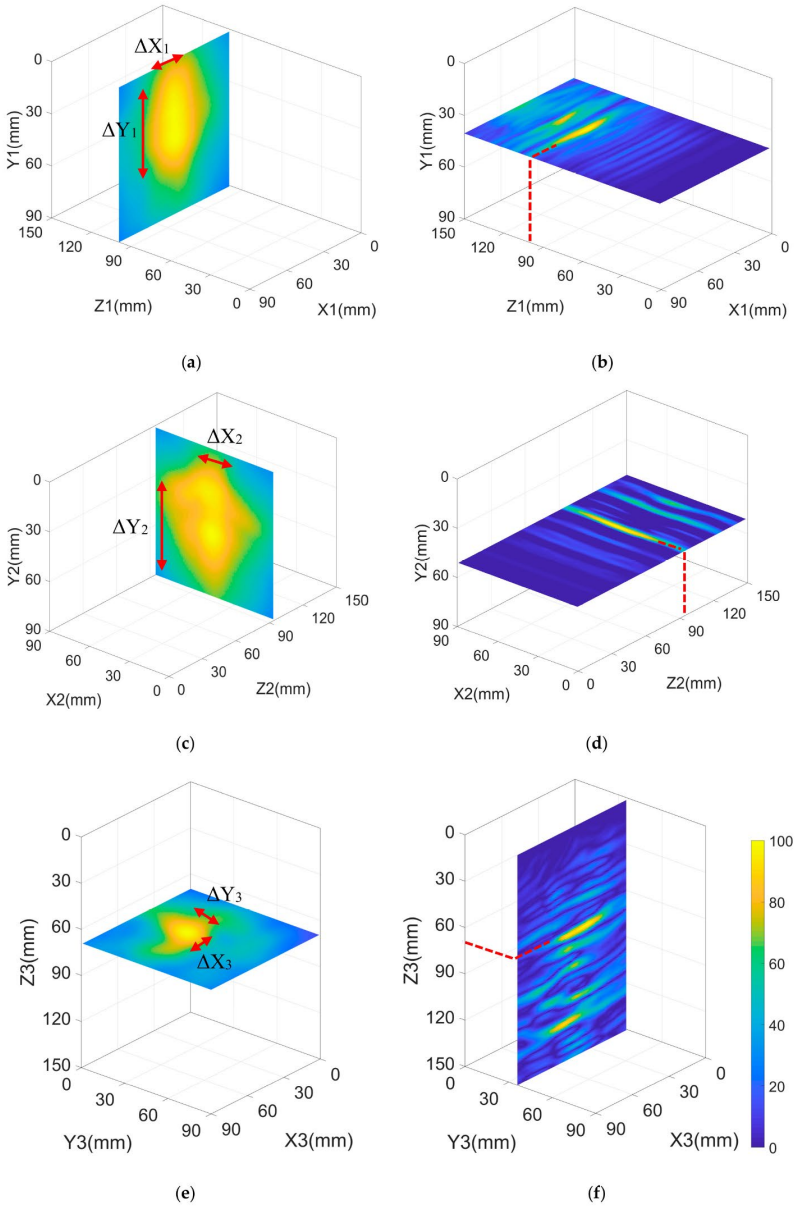

Figure 5-2: The SAFT algorithm results of the three-face experiment: a) *X1Y1* plane slice for face 1 at *Z1* = 99 mm; b) *X1Z1* plane slice for face 1 at *Y1* = 40 mm; c) *X2Y2* plane slice for face 2 at *Z2* = 95 mm; d) *X2Z2* plane slice for face 2 at Y2 = 51 mm; and e) X_3Y_3 plane slice for face 3 at Z_3 = 70 mm; f) X_3Z_3 plane slice for face 3 at Y_3 = 36 mm. (color map at bottom right applies to all subfigures).

For face 1, we have the front view of the defect in the X_1Y_1 (Figure 5-2a) and X_1Z_1 Figure 5-2b) planes centred at X_1 = 41 mm, Y_1 = 41 mm, and at Z_1 = 99 mm. The reconstructed defect dimensions are ΔX_1 = 18 mm and ΔY_1 = 55 mm, which correspond to a size error with respect to the original defect size of $\Delta X_{1,error}$ = 38% and $\Delta Y_{1,error}$ = 8%, and a positioning error of less than 1% in X_1, Y_1, and Z_1 planes. The positioning error refers to the difference between the actual position of the defect's centre in X_1, Y_1, and Z_1 planes and the detected ones. With regard to face 2, we see the side view of the defect at Figure 5-2c and Figure 5-2d in the X_2Y_2 and X_2Z_2 planes centred at X_2 = 49 mm, Y_2 = 45 mm, and Z_2 = 95 mm. The detected defect dimensions are ΔX_2 = 19 mm and ΔY_2 = 58 mm. This corresponds to a size error with respect to the original defect size of $\Delta X_{2,error}$ = 46%, $\Delta Y_{2,error}$ = 3%, and a positioning error less than 5% in X_2, Y_2, and Z_2 planes. Face 3 shows the top view of the defect in the X_3Y_3 and X_3Z_3 planes centred at X_3 = 42 mm, Y_3 = 34 mm, and at Z_3 = 70 mm (Figure 5-2e and Figure 5-2f). The detected defect dimensions are ΔX_3 = 16 mm, ΔY_3 = 16 mm, which corresponds to a size error with respect to original defect size of $\Delta X_{3,error}$ = 23%, $\Delta Y_{3,error}$ = 23%, and a positioning error less than 1% in X_3, Y_3, and Z_3 planes. These error data are summarized in Table 5-1 We emphasize that the ΔX_{error} magnitude in either face is related to the transducer's size, 13 mm in our case. It is not possible for the sensor to accurately measure the size of defects below or equal to the transducer's size.

Indeed, the size error ΔY_{error} is small because the defect size in the Y dimension is much larger than the transducer' size. Therefore, although the resulting size and positioning estimates obtained from each face show good global performance, the errors can be drastically reduced by using smaller size transducers.

Face	Face1		Face 2		Face 3	
Axis	*X*	*Y*	*X*	*Y*	*X*	*Y*
Detected defect size	18mm	55mm	19mm	58mm	16mm	16mm
Size error	38%	8%	46%	3%	23%	23%
Position error	<1%	<1%	<5%	<5%	<1%	<1%

Table 5-1: Detected defect size and size and positioning errors

Combining all the views of the three faces and representing them at the scale of the cube, we may generate the 3D reconstruction of the defect as shown in Figure 5-3. Here, a unique universal Cartesian axis reference *XYZ* is used for all the three faces with the origin in the corner of the cube object itself. The relative displacement between the scan faces is considered when superimposing the scan faces all together on the 3D reconstruction. We applied a thresholding filter to reject all data in Figure 5-2 below a certain amplitude to keep only the high intensity data to represent the defect position and shape. In our case, we selected two thresholds: 65% and 85% as the limits of the rejection of data. That was chosen after visualizing the unfiltered reconstructed images (Figure 5-2). We found that the points with high intensity begin around colour map of 75%, and so we decided to provide a ±10% margin below and above these limits to make our upper and lower thresholds 65% and 85%, respectively. The choice of the intensity reject threshold is a user-decision as in any image processing filter. Therefore, some care should be exercised when applying this filter in order to obtain good results without affecting image fidelity and quality. Applying these thresholds with proper fine-tuning of the limits also helps reduce the size error, improving the accuracy of the

algorithm. Figure 5-3a shows the Isometric view resulting from face 1 (Front view/X_1Y_1) scan area inspection by applying a reject threshold for data with intensity below 65%, while Figure 5-3b shows the front view resulting from face 1 scan area inspection by applying a reject threshold for data with intensity below 65%. Figure 5-3c and Figure 5-3d show the isometric view and side view representations respectively for face 2 with the same threshold condition. Figure 5-3e and Figure 5-3f show the isometric view and top view representations respectively for face3. Figure 5-3g shows the isometric view including the intersection between reconstruction results from the three faces with a filtering threshold of intensity reject for values less than 65%. Figure 5-3h shows the isometric view including the intersection between reconstruction results from the three faces with a more restrictive threshold of intensity to reject data with intensity below 85%. We superimpose the true cylindrical defect shape on the reconstructed defect images to see how close the detected information is, with respect to true information. The colour map at right hand side of Figure 5-3 represents the amplitude percentage and applies to all subfigures.

It is clear that the detected defect size and position match the true defect size and position. Increasing the number of scanned faces results in higher resolution reconstruction of the defect at all 360° angles. The reconstructed planes in our case show a high contrast between the points of high intensity (corresponding to the presence of the defect) and the points of low intensity (no defect). The use of the apodization function helped increase this contrast and eliminated the effect of reflections from side lobes or signals at large angles. The size error is enhanced for the case of a threshold of 65% to be less than 10% for the three faces in the horizontal dimension. In the case of 85% threshold, the size error is reduced to less than 5% in the horizontal dimension. In the vertical dimension, the size error is not affected by a significant change, with the same error as in the case of no threshold. In our case, the optimum

threshold after the fine-tuning was 85%, which strongly reduced the error in the horizontal dimension.

The 3D reconstruction of the defect in Figure 5-3 clearly shows that the improved SAFT method used in this work has powerful advantages in visualizing the defect in the 3D isometric view. The projections of the SAFT planes make it easier to distinguish the location of the defect in a 3D manner instead of just getting two dimensional results. The SAFT algorithms using a hybrid technique allows scanning over large objects without significant loss of information. In fact, we obtain better localized quality image of the defect with larger objects compared with smaller ones due to the aforementioned boundary conditions.

The precision of the results obtained here can be further improved using a noncontact transducer having smaller size, adapted to the horizontal size of the defect. The resolution would be enhanced and calculated accurately with less error. Another significant qualitative enhancement that results from using the noncontact transducer is a cleaner signal with a higher intensity contrast due to having the receiving transducer closer to the exciter. However, there are also some drawbacks. For example, the noncontact transducer must be placed very close to the exciter because otherwise the signal can be overly attenuated. Also, the airgap can affect the quality of the signal. This can be remedied by using a high-power pulsed laser exciter and high-gain preamplifier. Other critical factors related the experimental setup and the signal processing algorithm need to be considered. For instance, the SAFT algorithm is having limitations considering the angle between the exciter and receiver that should be small to avoid diffraction and side-lobe effects. This is already overcome in our case since our experimental setup was configured to place the exciting Laser and the receiving transducer adjacent to each other. Another important factor is the correct choice of the threshold criterion for apodization algorithm to maintain the lateral resolution of the main lobe and get rid of the effect of the side-lobes.

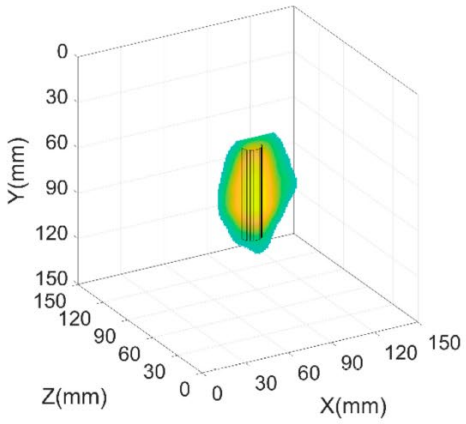
Y(mm)
Z(mm)
X(mm)
0
30
60
90
120
150

(a)

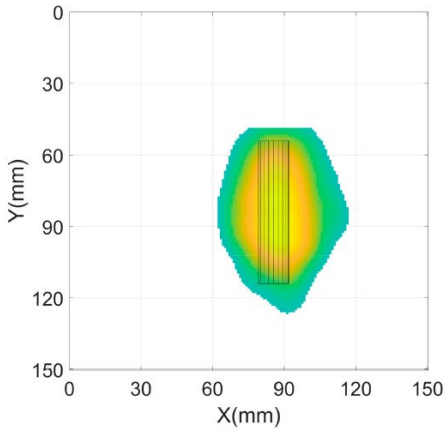
Y(mm)
X(mm)
0
30
60
90
120
150

(b)

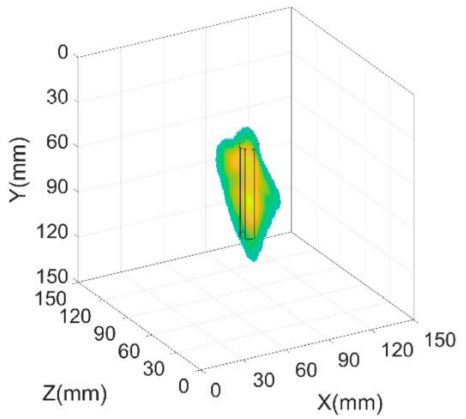
Y(mm)
Z(mm)
X(mm)
0
30
60
90
120
150

(c)

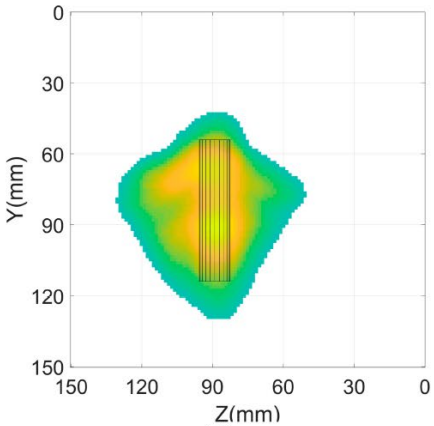
Y(mm)
Z(mm)
0
30
60
90
120
150

(d)

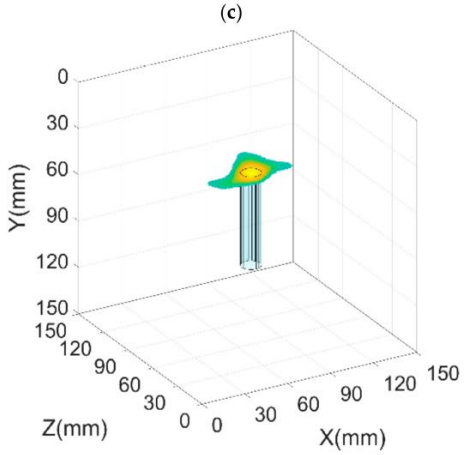
Y(mm)
Z(mm)
X(mm)
0
30
60
90
120
150

(e)

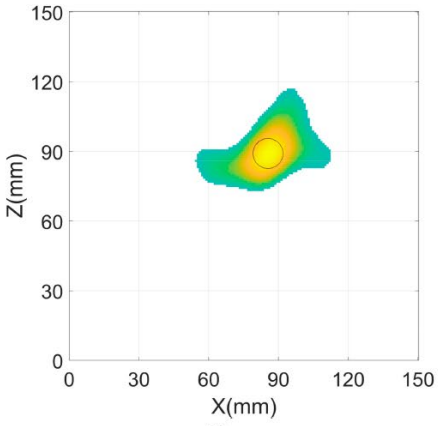
Z(mm)
X(mm)
0
30
60
90
120
150

(f)

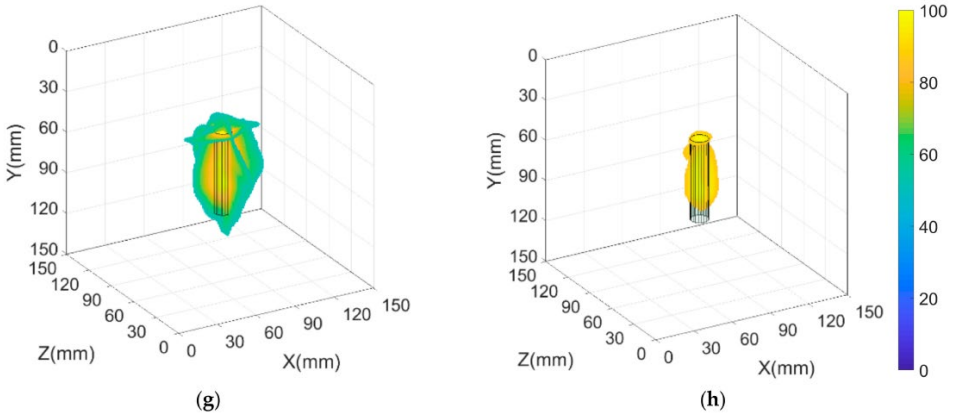

Figure 5-3: 3D reconstruction of the defect by combining the resulting SAFT images from the three faces and superimposing the actual cylindrical shape of the defect. a) Isometric view resulting from face 1 (front view/*X1Y1*) scan area inspection by applying a reject threshold for data with an intensity below 65%; b) Front view resulting from face 1 scan area inspection by applying a reject threshold for data with intensity below 65%; c) Isometric view resulting from face 2 (Side view/*X2Y2*) scan area inspection by applying a reject threshold for data with an intensity below 65%; d) Side view resulting from face 2 scan area inspection by applying a reject threshold for data with an intensity below 65%; e) Isometric view resulting from face 3 (Top view/*X3Y3*) scan area inspection by applying a reject threshold for data with an intensity below 65%; f) Top view resulting from face 3 scan area inspection by applying a reject threshold for data with an intensity below 65%; g) Isometric view resulting from the 3d reconstruction by applying a reject threshold for data with an intensity below 65%; h) isometric view by applying a stricter reject threshold for data with an intensity below 85%. (Color map at bottom right applies to all subfigures.)

Finally, the selection of the amplitude threshold, to the resulting SAFT 3D reconstructed image, is important to be chosen carefully to improve the size and position error, while maintaining the correct dimensions of the defect.

5.3. Conclusions

We have demonstrated that using a hybrid method composed by LGU as an exciter, and noncontact transducer as a detector, we can design a fully noncontact configuration for NDT inspection and 3D reconstruction of a defect embedded in a metallic object. The use of LGU allows remote excitation of large scan areas with higher power levels, not achievable with conventional transducers, which helps with sample penetration and embedded defect detection. On the other hand, noncontact transducers have the advantage of having a large number of points scan and proximity to the exciter, which allows the detection of more details of the reflected ultrasound waves. The combination of signals coming from three orthogonal scanning areas of the object detects the defect's presence from all perspectives/angles. An improved SAFT algorithm is implemented to localize the defect position with a signal to noise ratio, taking into consideration the limitations of structural dimensions. The SAFT algorithm provides more information about the exact location of the defect using 3D reconstruction imaging. The use of the 2D apodization technique helped enhance the SNR ratio and reject the effect of side lobes excited along with the main ultrasound lobes, as well as the effect of wide-angle reflections. The hybrid, fully noncontact techniques presented here provide a strong alternative to conventional NDT techniques, with higher flexibility, higher resolution and powerful detection of embedded defects. An important advantage of the proposed method is that there is no need to use a healthy reference sample to compare with the resulting reconstruction image of the unhealthy sample to detect the presence of the defects. However, in the case of an object that has no symmetrical dimensions or has a composite structure of different materials, it would help to use the healthy reference sample, to avoid misrepresenting the internal reflections from object's boundaries.

Chapter 6. Phononic crystal as an ultrasound lens for ultrasound propagation management in solids

In all the experiments presented in the previous chapters we had to deal with the ultrasound propagation and diffraction in a solid material. In certain configurations, the diffraction is detrimental because it makes the intensity of the ultrasound to decrease very fast with the propagation distance and reduce the resolution in detection. The question if we can control and eventually reduce this diffraction and if this control would improve our NDT measurements arises almost from the beginning of this PhD work. Thus, we have started a parallel study of the ultrasound propagation management using phononic crystals (PC), as briefly explained in section 1.5. Theory shows that we can modify the diffraction properties of ultrasound waves using an artificially build PC structure.

In this chapter we provide a numerical study of a PC designed for the control of the directivity of ultrasound waves propagating in a solid media (in particular aluminum). We aim to generate an enhanced spatial wave-front profile, propagating with the desired diffraction pattern on the focalization or self-collimation regimes.

Finally, we propose a device that can be used for the diffraction management of longitudinal elastic waves based on the properties of an

ultrasonic lens (UL) made of a PC with 2D periodicity. The spatial wave-front profile generated by the UL propagates with a particular diffraction pattern into the medium under inspection. We aim to control and to enhance the directivity of ultrasound waves further propagating in a homogeneous solid medium. We consider a 2D PC, consisting in a periodic distribution of cylindrical holes of air drilled in an aluminium block, arranged in a square periodic lattice. We analyse the dispersion relation and spatial dispersion of the periodic medium. The PC parameters are carefully chosen to provide specific patterns based on physical diffraction effects like focalization and auto-collimation. We evaluate, with numerical simulations, the radiation pattern of the waves emitted by a ultrasound transducer and spatially filtered by the UL coupled to the object under inspection at a specific working frequency.

Figure 6-1 shows a schematic representation of the idea of our proposal. Let's consider an ultrasonic source emitting acoustic waves which are coupled to a solid object under test. In normal conditions, the beam propagates freely in the homogeneous medium and it is strongly diffracted, resulting in a spatial spreading of the wavefront from the source (Figure 6-1a) The ultrasonic field can be generated by an acoustic transducer placed in a contact or noncontact configuration. If an UL is now introduced between the source and the object under study, the diffraction of the acoustic field inside the sample can be controlled. Two main effects may arise: focalization effect, where the ultrasonic beam is focused down to a minimum spot diameter at a certain position inside the sample (schematically shown in Figure 6-1b) and self-collimation, where the beam propagates with a constant diameter for a certain distance inside the sample, with a reduced diffraction (effect shown in Figure 6-1c) ,

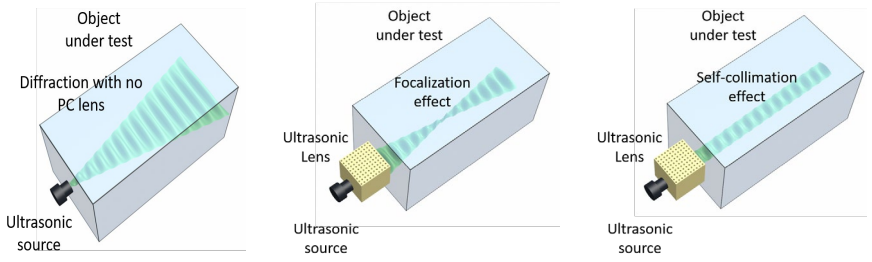

a) b) c)

Figure 6-1: Schematic representation of ultrasound propagation beam into the object under test. a) Beam diffraction of the ultrasonic source without, b) with coupling an acoustic lens to the object for focusing waves inside the object and c) with coupling to acoustic lens for self-collimation of waves inside the object.

6.1. Dispersion band analysis

Propagation of ultrasonic waves in a PC is determined by the acoustic parameters of the medium, by the constant of the periodic lattice and filling factor, as well as by the wavelength of the wave. The dispersion relation of a periodic medium is a useful representation of the propagating bands in the reciprocal space [77–79]. For certain geometries and propagation directions, frequency band gaps appear at specific frequency bands for which acoustic wave propagation is forbidden inside the crystal.

Another useful representation is the iso-frequency contour maps, that gives information about the propagation of the acoustic beams at different frequencies in different directions of the PCs. Different plane waves will acquire phase shifts depending on their propagation angles and consequently, this phase difference between different components results in a diffractive broadening of the beam [102]. A perfect circular isofrequency contour means that acoustic wave propagates isotopically, a concave contour line would result in positive diffraction (divergence) and a convex contour line on the contrary results in negative diffraction (convergence or focusing) [98–101]. Additionally, any flat contour line

would mean that all these wave vectors are going to pass without suffering any diffractions, hence the concept of self-collimation [81,102] (see Figure 1-18, Chapter 1).

We consider a 2D PC consisting of a periodic distribution of cylindrical holes (air) drilled in an aluminium block, arranged in a square periodic lattice, as schematically shown in Figure 6-2a. Figure 6-2b represents the square unit cell in real space, where a is the lattice constant and r is the radius of the air hole. Figure 6-2c shows the unit cell in the reciprocal space with the Bloch vector representation of the Γ-X-M directions where (*kx*,*ky*) are wave vectors in the 2D reciprocal space.

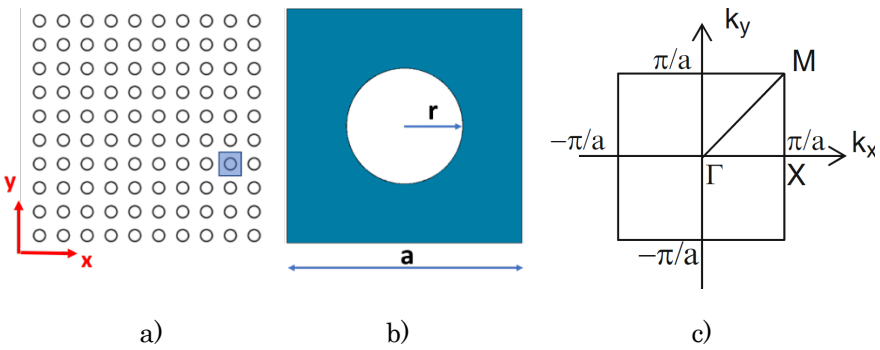

Figure 6-2: Schematic diagram of PC structure with inset of a unit cell a) the 2D lattice structure b) unit cell representation in real space (x, y) , described by the parameters r, a; c) unit cell representation on the reciprocal space (*kx* and *ky*): Bloch vector in the Γ-X-M directions.

In this study we have calculated the band structure and isofrequency surfaces of different PCs with square lattice and scatterer radius varying between 1.5mm and 3.5mm. We analysed them in all the representative propagation directions in the reciprocal space to fit the requirement of an appropriate diffraction pattern for simultaneously focusing of waves and collimation in the ultrasonic regime. The most adapted configuration for these conditions is a PC with radius of air holes r = 2.5mm and lattice

constant a = 10mm, corresponding to a filling factor $ff = \frac{\pi r^2}{a^2} = 0.2$. Figure 6-3a shows the band structure of this PC structure. For simplicity, only the Bloch vector in the Γ-X direction of the reciprocal space is represented in the horizontal axis. We can see that a bandgap in the Γ-X direction appears between 230kHz to 270kHz (both frequency limits are shown with dashed lines). The first two bands at low frequencies correspond to the low-frequency limit and the waves propagate in the crystal as in a homogeneous medium with and almost linear dispersion curve. Mode 1 (first curve from bottom) is linear across the most of Γ-X axis which corresponds to linear propagation with almost no diffraction as if no PC exists. Mode 2 and mode 3 (second and third curves from bottom) correspond to longitudinal and transverse waves that suffer some dispersion due to the presence of the PC.

The propagation through the phononic crystal can be described by the dispersion relation ω(*kx*,*ky*) of the periodic medium. The acoustic beams excited by the source outside the PC propagate inside the crystal as a set of plane waves and Bloch modes at different angles. A property of isofrequency or equifrequency surfaces (EFS) is that the direction of the energy flow for a given wavevector coincides with the normal to the equifrequency contour, pointing towards the increase in frequency [113].

According to this, beams projected into concave EFS, reduce their diffraction through propagation inside the crystal. This particular behaviour of waves in periodic media leads to focusing. The more tilted are the projected segments of the EFS, the more intense is focusing. When flat segments appear in the EFS of propagating Bloch modes, the self-collimation effect is produced. As the curvature of EFS is related to the diffractive broadening of the beams, then the flattening of these lines implies the vanishing of diffractive broadening, i.e., the self-collimation [114]. Consequently, under special circumstances, the propagation of narrow beams over long distances without diffractive broadening is

possible inside the PC. As it will be shown, conditions to propagate focused and collimated beams are found by exciting the PC used in this work at the eigenfrequencies f_f=172kHz (band 2) and f_c=193kHz (band 3), respectively (see Figure 6-3a).

Figure 6-3b,c show the EFS of both modes of interest, Mode 2 and Mode 3, respectively. Figure 6-3b shows the EFS for the frequencies of interest where focusing is expected to occur in band 2. This regime is close to the boundary of the band, next to the band-gap, where the dispersion curves are convex and the focusing of the beams behind the crystal is possible [115]. We note that the isofrequency curves present concave segments along the Γ-X direction ($ky = 0$) in Mode 2 for frequencies above 165Hz. More specifically, it can be seen that the focusing occurs with a convex shape of EFS and a wider spatial width at frequency f_f = 172 kHz. Figure 6-3c shows the EFS of band 3 where flat segments can be observed around 200kHz at the Γ-X direction. As propagation out of the crystal bends the surfaces towards concavity, it will be shown that the frequency of collimation is found at f_c= 193kHz.

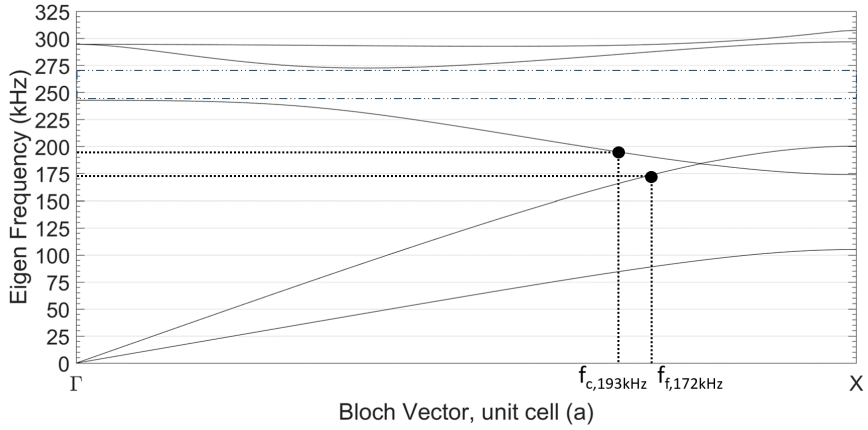

a)

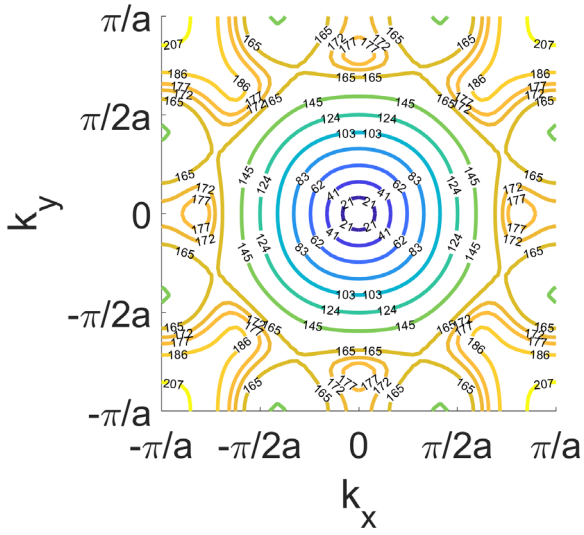

b)

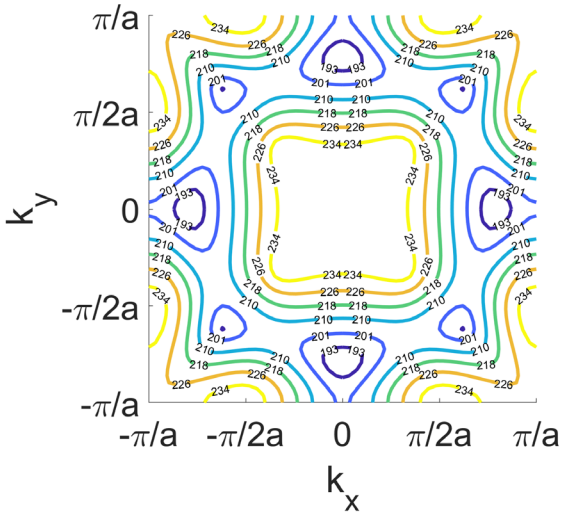

c)

Figure 6-3: Dispersion characteristics of the 2D periodic PC with square lattice, constant lattice, a = 10mm and radius of scatterers (holes), r = 2.5mm. a) Band structure for the ΓX direction. The lower and upper frequency limits of the first bandgap are shown in dashed lines. Equal-frequency surfaces (EFS) in the reciprocal space (*kx*, *ky*) b) for mode 2 and c) mode 3

6.2. Non-diffractive wave propagation

We consider now only the propagation of the mode 2 shown in Figure 6-4, where the curvature of the isofrequency lines is convex (corresponding to focusing effect), or flat (corresponding to self-collimation effect). Elastic equations are solved in the solid media by discretizing the medium with simulations based on the finite element method, using Comsol software with aluminium as the solid media and vacuum as the holes in the PC. We used perfectly matched layer to assume there is no reflections at the boundaries. Due to the very high impedance contrast between aluminium and air (vacuum), the scatterers are assumed to reflect perfectly the elastic waves. We simulate the frequency dependent propagation of an ultrasonic beam excited by a piston-like source. The input source was simulated as a prescribed displacement source with only amplitude in the horizontal direction, i.e: assuming the source is only exciting longitudinal waves. The displacement field x is composed by two components x(u,v). We applied calculations for surface plot of the absolute value of the horizontal displacement field abs(u) at different frequencies. The horizontal displacement represents the propagation of longitudinal waves.

Figure 6-4 shows different propagation regimes we obtain for different frequencies. Figure 6-4 shows the free propagation of the ultrasound emitted by the source at the frequency of 172 kHz in free propagation from the source to the medium. From the band structure of the PC shown in Figure 6-3 one can see that the second mode of propagation (longitudinal) is active up to 200kHz, where the band-gap appears. Figure 6-4b shows the surface plot intensity at the same 172kH frequency, when the PC is inserted in front of the source. The focusing occurs with a maximum intensity at a distance of 15 cm from the crystal output and a rather constant focalization diameter for a propagation distance of ~25cm, after which diffraction is similar to propagation in the

homogeneous metal. Figure 6-4c corresponds to self-collimation effect obtained at the frequency of 193 kHz that matches with the contour map in Figure 6-4. Within the bandgap, there is a complete diminishing of any propagation at frequency 250kHz, as shown in Figure 6-4d which matches with dispersion curves in Figure 6-3a. Colour map in Figure 6-4 and in all surface plots next described in this chapter represent percentage of maximum value of horizontal displacement abs(u), i.e: intensity at surface plot is normalized to the maximum intensity in the plot.

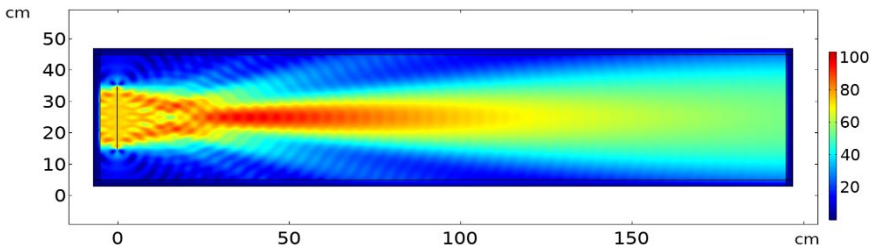

a)

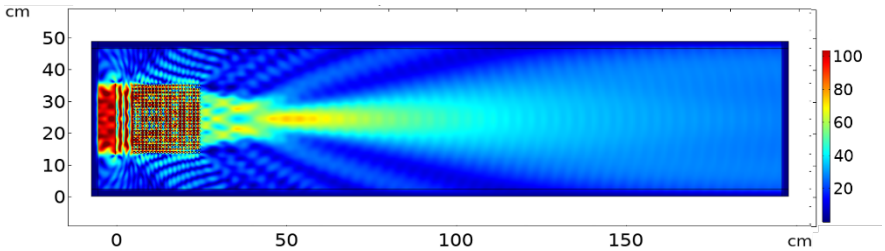

b)

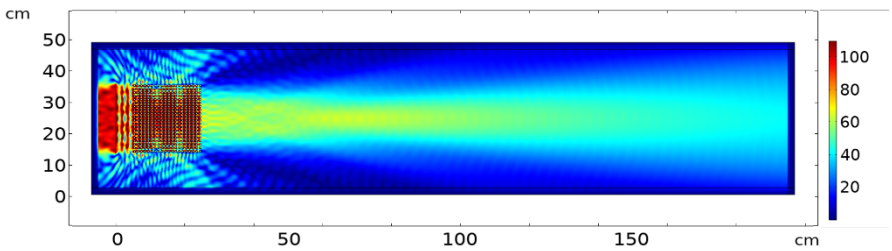

c)

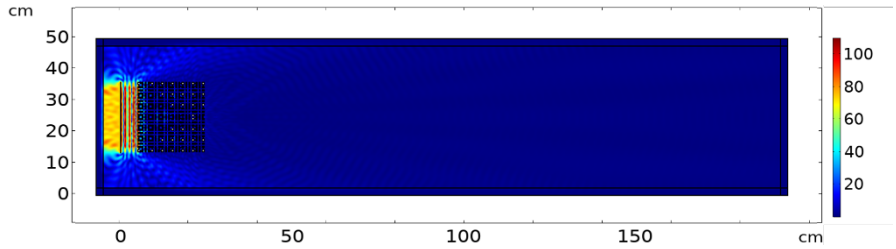

d)

Figure 6-4: Surface plot of absolute of horizontal output displacement (u) propagation using a phononic crystal size 20x20 elements with a line excitation source size 20cm as input displacement (u), and the spacing between source and the phononic crystal is 5.5cm. Detection frequency: a) 172kHz (no crystal) b) 172kHz with PC (focusing) c) 193kHz with PC (self-collimation) d) 250kHz with PC (bandgap). Color map represents percentage of maximum value of horizontal displacement abs(u), i.e: intensity at surface plot is normalized to the maximum intensity in the plot.

Figure 6-5a shows the response in case of free propagation without using PC at 172kHz. The amplitude is measured across a horizontal line at the center of the crystal passing from left to right. The natural oscillation can produce some sort of focalization due to nature of line source but is much broader than the case when a PC is used. Figure 6-5b shows the horizontal axial profile of the horizontal displacement for the surface geometry at 172kHz. Once the waves exit the PC it has only the focalization response allowed by the PC geometry. The percentage of maximum intensity at the focal point to source intensity in case of free propagation and using PC are 133% and 75% respectively. The insertion loss of the PC resulted in the focalization intensity to be 75% of input intensity.

The focalization appears at distance between horizontal line X=~45 to ~70cm in both Figure 6-4b, 6b).

It can be seen in Figure 6-5c that at the self-collimation frequency, the horizontal displacement is relatively constant across the majority of the horizontal line passing at the center of the object. One can see the percentage of self-collimation intensity to source intensity is ~65% at 193kHz. This is in comparison to the maximum focalization intensity percentage that is aforementioned to be 75% (only at focusing point and amplitude is decreasing rapidly with distance (Figure 6-5b) in comparison to self-collimation).

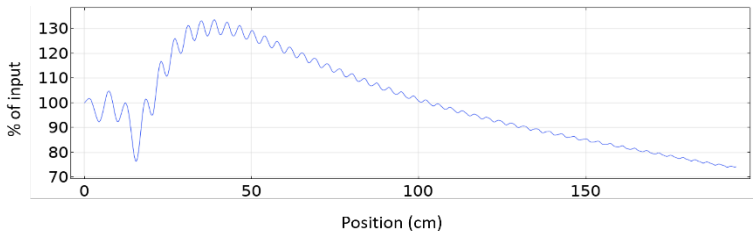

a)

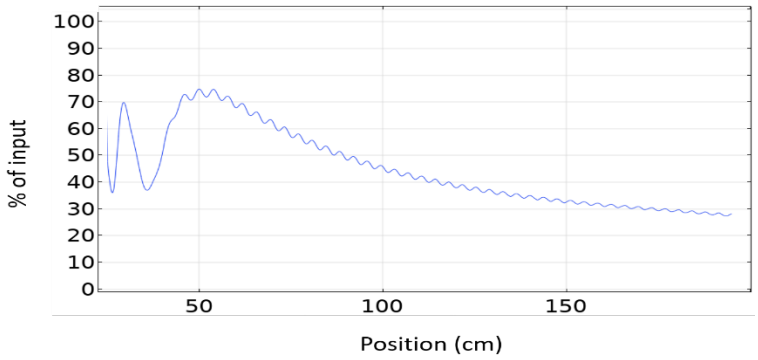

b)

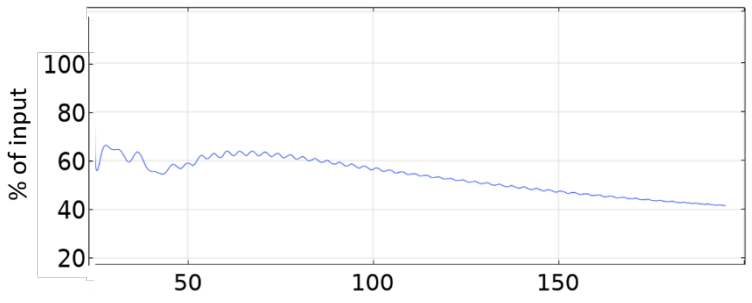

c)

Figure 6-5: Absolute of horizontal output displacement abs(u) propagation across horizontal line passing by center of object from source (arc length=0) to the end of the geometry, in case of a) 20x20 PC and at frequency f_f=172kHz b) no crystal and at frequency f=172kHz. c) 20x20 PC and at frequency at f_c=193kHz.

6.3. Ultrasonic lens device

The aforementioned analysis was performed using only solid material and considered the PC to be part of the same domain of propagation in the solid material. However, this does not actually match with the actual experimental configurations, where the excitation is done through an ultrasonic source (e.g: transducer) that is coupled to the PC (which can be considered as an acoustic beam-shaping lens for the purpose of focusing or self-collimation effect on the target object) using a coupling material (fluid gel with acoustic impedance matching with the material of propagation). The PC itself should be coupled to the main solid material on which we need to investigate the self-collimation or focusing effects. The coupling material is used with acoustic impedance similar to that of the solid material where ultrasonic propagation waves take place. In real experiments, the coupling has an acoustic impedance that should be very close to that of the material of interest to reduce coupling losses. Figure 6-6 shows the block diagram of the experimental configuration. The Comsol model uses acoustic/structure interaction physics to simulate the affect of propagation in the gel (fluid material) and the PC and the solid object (solid material). The input source in Comsol in this case is represented by pressure source in fluid (gel with acoustic impedance 75% of solid material). this pressure is converted to displacement filed in the solid materials using the acoustic interaction physics. Gel coupling thickness before and after crystal is 2mm.

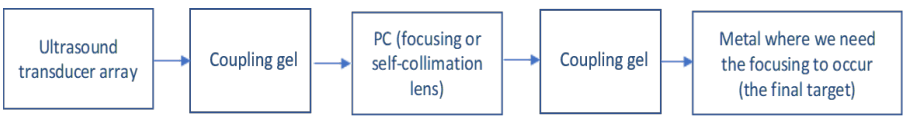

Figure 6-6: Block diagram of the experimental configuration where PC is used as a focusing or a self-collimation lens that is inserted halfway between ultrasonic transducer and object under test. An acoustic coupling gel is inserted at the interface between source, PC lens and solid object.

Figure 6-7 shows the results of propagation using a 30x20 element PC used as a focusing/self-collimation lens. The focusing/self-collimation effect of the PC is frequency-dependent as explained earlier in this article. The width of the input source of excitation and the PC lens is the same as the object under test (i.e: they cover all the object surface area).

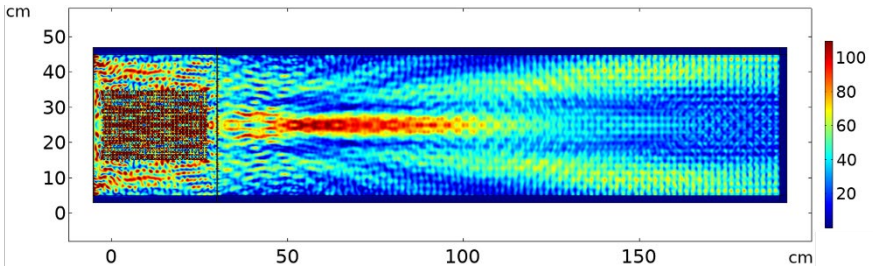

a)

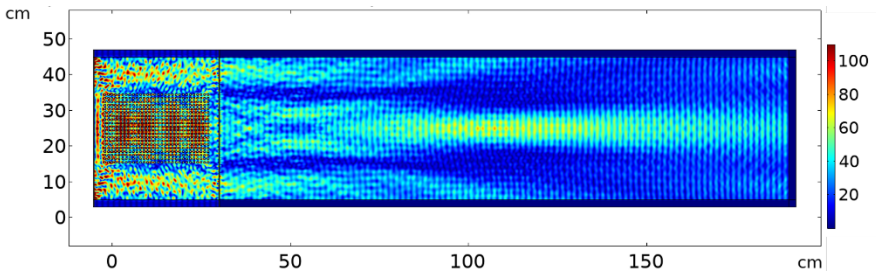

b)

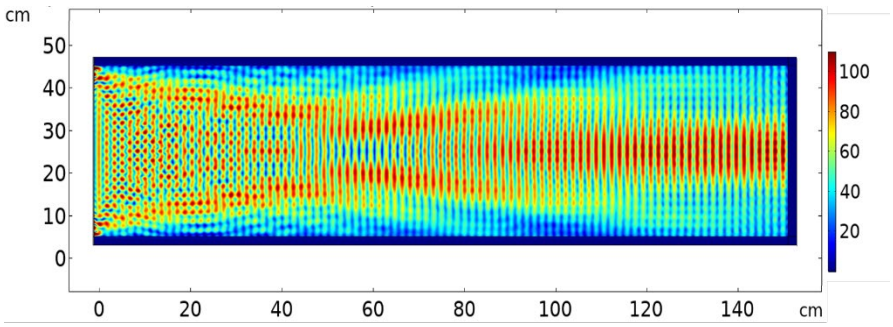

c)

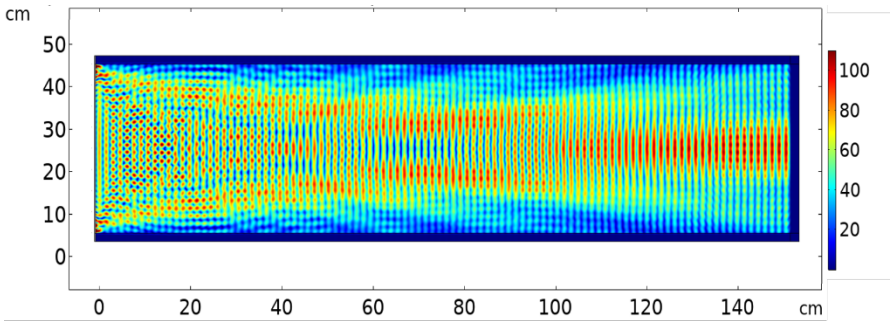

d)

Figure 6-7: using 30x20 element PC lens with coupling interface between source, lens and object for a) focusing at 172 b) Self-collimation at 193kHz c) no crystal, 172kHz d) no crystal, 193kHz.

Figure 6-8 shows the intensity across a horizontal line passing through the centre of the PC (Y=25 cm) for the same surface plot representation in Figure 6-7. Figure 6-8a shows the response at the focusing regime (172kHz), it is clear the intensity drops with distance from the focal point. When the horizontal line shifts up or down (Y=15 cm or Y=35 cm, red curve), the intensity is very low at early distances , because there is only focusing at the centre of the object (Y=25 cm, blue curve), but with larger distances the intensity slightly increases due to diffraction effect.

In Figure 6-8b, the response at frequency 193kHz (self-collimation regime), the intensity is almost uniform after the self-collimation is achieved and the decay is happening slowly. In this case, when the horizontal line shifts up or down (Y=15 cm or Y=35 cm, red curve), the intensity is very low across the whole object size because all the intensity is concentrated in the centre (Y=25 cm, blue curve) due to the self-collimation effect.

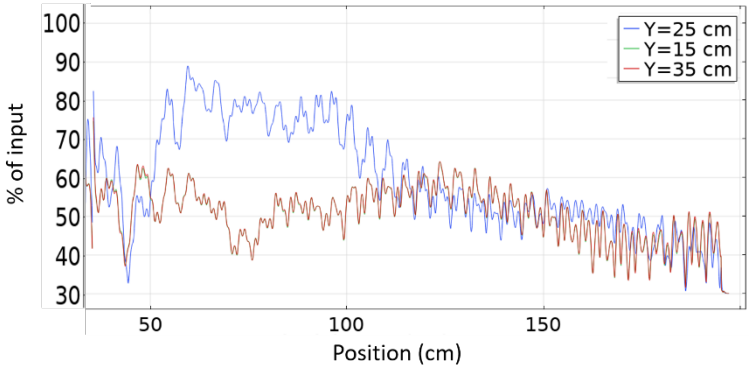

a)

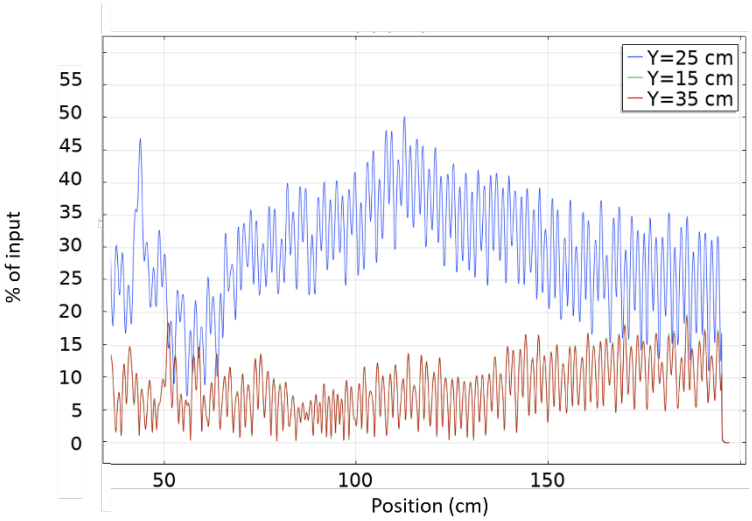

b)

Figure 6-8: Absolute of horizontal output displacement (u) propagation across horizontal line at Y=25 cm passing by center of

PC lens of 30x20 elements to the end of the geometry, in case of a) frequency 172kHz (focusing regime), b) frequency 193kHz (self-collimation regime).

Intensity ratio between focalization and source intensity at 172kHz is 90% (Figure 6-7a, Figure 6-8a) (source considered just at the entrance to the PC lens after coupling, while the ratio between self-collimation intensity and source intensity at 193kHz is 50% (Figure 6-7b, Figure 6-8b). Thus, the PC lens effectively focuses or self-collimates the beam with limited insertion loss. Comparing these results with the case of no crystal, we find that for same source intensity, the maximum diffraction intensity abs(u) compared to input intensity at the input to the solid object directly after the coupling gel is 142% at 172kHz (Figure 6-7c) and 128% at 193kHz (Figure 6-7d).

It is seen that after using the coupling the wave propagation inside the object has been distorted and diffraction increased significantly in the case of no crystal was used (Figure 6-7c,d). However, when we used the crystal, the diffraction was controlled to a great extent in both focalization and self-collimation regimes (Figure 6-7a,b). This is a great enhancement to the wave propagation pattern inside the object thanks to the PC lens.

Previous results were simulated at specific single frequencies. In actual experiments, we use ultrasonic transducers that are sensitive for a frequency bandwidth rather than single frequencies. Thus, we need to modify the simulation to match the actual experimental case. Figure 6-9 shows the results at focusing and self-collimation with a broader band frequency integration. Figure 6-9a shows the results for focusing at frequency bandwidth of 10kHz with cut-off frequencies 167 to 177 kHz, while Figure 6-9b shows the results for self-collimation regime for frequency integration at 10kHz bandwidth with cut-off frequencies 190-200kHz. It is shown that the focusing effect in Figure 6-9a is further enhanced and got so much stronger compared to the single frequency representation at Figure 6-7a since the whole bandwidth lies in the

focusing zone, while the self-collimation effect in Figure 6-9b in the frequency integration representation is further attenuated in comparison to single frequency surface plot in Figure 6-7b, because the self-collimation occurs at a very narrow frequency range, and beyond that, other phenomena occur (diffraction, or focusing).

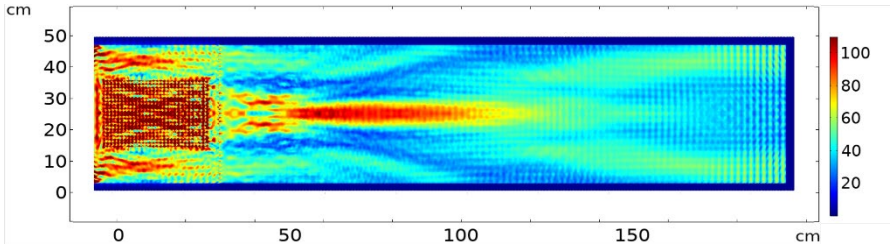

a)

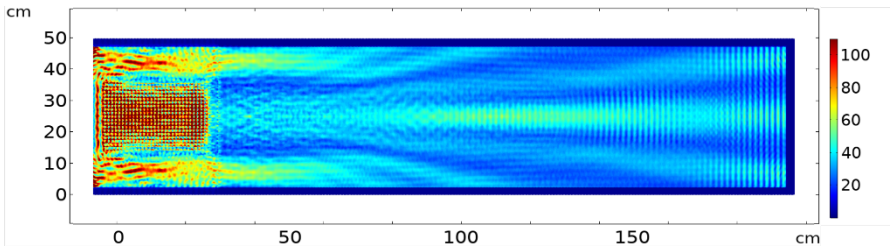

b)

Figure 6-9: Using 30x20 element PC lens with coupling interface between source, lens and object for: a) focusing at frequency bandwidth of 10kHz with cut-off frequencies 167 to 177kHz b) Self-collimation at frequency bandwidth of 10kHz with cut-off frequencies 190 to 200kHz.

6.4. Conclusion

We provided a 2D parametric study of wave propagation in metallic objects with and without PCs. The study considered 2D surface plots of the propagating waves across the object. In addition, frequency spectrum

across chosen points and lines of interest vertically and horizontally was considered to understand the behaviour of the wave propagation in the near field and far field at various angles. It was shown that the frequency spectrum analysis matches with the eigen frequency analysis using dispersion curves and iso-surface contour maps of the allowed and forbidden frequencies for the goal of studying the spatial focalization and self-collimation of ultrasound beams using 2D PCs. The use of PCs as focusing/self-collimation lens for ultrasound wave propagation in solids is possible with proper selection of crystal parameters and a matching coupling acoustic impedance.

Conclusion and future work

General conclusion

In this PhD thesis our main goal and achievement was to study different topologies for localizing and reconstructing embedded defects in large metallic objects using laser generated ultrasound as a modern non-destructive testing tool. The research started by reviewing the available literature and recent achievements in this field in the past few years. It was required to contribute in finding/enhancing solutions to technical problems and challenges that are confronted in both research and industry environments related to the subject field. During the study of NDT problem of defects in metal, we faced another problem related with ultrasound wave directionality and boundary effects in the target volume. We thought about the ability to direct ultrasound waves at certain angles, for instance far from boundaries or to propagate in a direct path towards the receiving transducer as an enhancement to the performance of non-destructive testing process. Using phononic crystals as an ultrasound lens for this goal was proposed and studied as a secondary goal in this thesis.

Chapter 1 provided an introduction to main concepts and theoretical background of basic physics of ultrasound. Section 1.1 discussed different types of ultrasound waves and ultrasound wave propagation in different media, and more specifically in solids. A brief note about the effect of media impedance on wave propagation and boundary effects between different media is studied. Mode conversion effects were mentioned as an example of different phenomena taking place at the interface between different media. The concept of group and phase velocities was introduced. A theoretical review of different ultrasound sources of excitation was described including point source radiation and piston source excitation. Side lobes were described as a side effect of wave propagation that we

need to minimize their effects. In section 1.2, we highlighted the modern applications of laser generated ultrasound as a tool for non-destructive testing. The basic physics of laser ultrasound were introduced and discussed in comparison to conventional ultrasound source techniques. Section 1.3 provided a review about Non-Destructive Testing techniques using ultrasound waves including the famous A-scan, B-scan, C-scan topologies. Section 1.4 focused on signal processing analysis using various signal processing algorithms. The mathematical background of different algorithms was provided including Wavelet Transform, clustering mathematics, SAFT analysis, Apodization mathematics in one and two dimensions. Section 1.5 provided a brief introduction about basic concepts of phononic Crystals and the physics of their propagation, dimensionality, diffraction and dispersion relationships. At the end of chapter 1, we described the structure of the thesis book and objectives of the work at hand at section 1.6.

Chapter 2 included the first results we had in non-destructive testing. We started the chapter by showing the experimental configuration. We provided a B-scan experiment for a thin metallic object. We used an experimental configuration where we do automatic scanning with fine resolution across a line on the face of the object using laser generated ultrasound and detection using a conventional contact transducer, hence the hybrid technique.

We provided a comparison between the B-scan results when the sample objects under test were healthy and unhealthy. Using the time-of-flight of the propagating waves and the reflected echoes showed the location of the defect in a one-dimensional section view. We compared our experimental and signal processing results with those of a commercial device from Olympus to judge the accuracy we got in our own results and show the constraints that we have and the possibilities to overcome them.

Chapter 3 extended the analysis and non-destructive testing to two-dimensional level. We used a different experimental configuration where we do the automatic scanning over an area on the face of the object instead of the scan line configuration used in chapter 2. The signal processing got more complex using wavelet algorithm. This technique has far more advantages compared to Fourier transform analysis as it gets information about time and frequency components of the signal simultaneously. We first tested our wavelet analysis algorithm over several measured signals to check its accuracy in predicting the correct time-of-flight of the defect-related echoes. Next step was to develop a novel technique to use the huge number of scanned points over the area of the object surface to predict and reconstruct the defect in a two-dimensional plane and determining the depth information of the defect location. This novel algorithm required extensive signal processing behind the wavelet analysis itself. We used the time-of-flight data to generate three-dimensional ellipsoid intersections at the defect location. We used the DB-scan clustering technique iteratively to segregate different groups of collected data based on the time-of-flights. The iterative clustering resulted in deducing the location of the defect based on the maximum number of ellipsoid intersections. An internal defect at 95 mm from the surface of inspection is considered, which represents a challenging condition. Under such a scenario, the proposed methodology shows reliable fault diagnosis results, with a location and sizing error of 4.53 mm and 11.1%, respectively. This methodology can be extended in future to generate a three-dimensional defect reconstruction.

Chapter 4 described the use of a different algorithm to reconstruct the location and position of the defect in two-dimensional regime as well, namely synthetic aperture focusing technique. We used the same experimental configuration used for chapter 3 with the use of two receiving contact sensors. We first applied an experiment to the thin sample. At the primary stage, the SAFT algorithm was applied to the

acquired data. The novelty in this stage was using the hybrid technique in such experiments which eases the scanning process in comparison to using conventional ultrasound exciters. In addition, SAFT algorithm was used in the past mainly with one-dimensional line scanning, while in our case we used a two-dimensional area scanning thanks to the capabilities of the laser excitation. A sizing error of 4.6%, concretely, ΔX_{error}=2.5% and ΔY_{error} =6.7% and a positioning error of 12.25%, concretely, X_{error} =2.5% and Y_{error} =22% was calculated for the reconstructed defect image in comparison to real defect information. However; there were some artifacts in the reconstructed images due to the presence of redundant echoes (with lower intensity compared to main reconstructed echo) due to the boundaries and side lobes' reflections. This was a challenge to overcome with traditional signal processing techniques. We developed a novel approach that uses the apodization technique to remove the side lobes and boundary effects. The apodization was previously used by other researchers in the past for one-dimensional scanning and one-dimensional reconstruction. However, in our case we extended the algorithm of the apodization function mathematic model to the two-dimensional space. This enhanced the resulting reconstructed defect image and significantly removed the side lobe echoes. The resulting size and position errors in this case are respectively: ΔX_{error}=2.5% and ΔY_{error}=38% and position errors X_{error}=2.5% and Y_{error}=0%. Later on, we applied another experiment on a cube sample instead of the thin sample and used the same experimental configuration. We applied SAFT analysis without the apodization function. The resulting size errors in this case is ΔX_{error}=30%, ΔY_{error}=20%, ΔZ_{error}=30% and the Positioning error in this case is X_{error}=6%, Y_{error}=0%, Z_{error}=3% in the three dimensions. It was a challenge to be able to detect defects at a deep position (100mm) inside the object with the worrying of signal attenuation inside the object but the experimental configuration, hardware and signal processing analysis was robust enough to provide clear and strong information that helped in successful defect reconstruction.

Chapter 5 considered the same SAFT analysis for a complete three-dimensional reconstruction. In order to achieve this goal, it was required to apply the laser scan and sensor detections on three orthogonal faces of the defect. It was impossible for this huge scanning data to use contact transducers nor the galvanometer scanning hardware anymore. Thus, in this case, we moved to use a non-contact transducer along with a motorized *XY* scanning stage. The use of the non-contact transducer, scanning motor stage, and laser exciter converted the experimental configuration into a completely remote system, that can fit later for industrial applications where the object under test is difficult to reach by contact methods. In addition, applying the scan over three orthogonal faces helped get information about the defect at different angles/perspectives that provided a full three-dimensional image of the defect. The two-dimensional apodization technique was used again in this remote scan/reconstruction system to enhance the results of reconstruction. The reconstruction accuracy results on the three faces are: size error of $\Delta X_{1,error}$ = 38% and $\Delta Y_{1,error}$ = 8%, $\Delta X_{2,error}$ = 46%, $\Delta Y_{2,error}$ = 3% and $\Delta X_{3,error}$ = 23%, $\Delta Y_{3,error}$ = 23%, while the positioning error was less than 1% in X_1, Y_1, and Z_1 planes, less than 5% in X_2, Y_2, and Z_2 planes and less than 1% in X_3, Y_3, and Z_3 planes. The accuracy and quality of the reconstructed image and the absence of redundant echoes or false echoes proves the robustness of the developed algorithm and the novel enhancements provided in this thesis.

In chapter 6 we discuss a simulation study using COMSOL and Matlab to model an ultrasound lens using phononic crystals for focalization and self-collimation of waves behind the crystal. The study was subdivided in different stages. In section 6.1, it was important to vary the unit cell size of a square lattice and study the effect on the dispersion curves and iso-frequency contour maps. These are the preliminary studies to know the diffraction response at different crystal configurations. In section 6.2, the frequency response analysis was performed where the

crystal is embedded as a part of a homogenous solid material. The analysis was performed in focalization regime (section 6.2.1) and self-collimation regime (section 6.2.2). A parametric study included the variation of crystal's and exciter source's parameters including crystal element size, excitation source size and spacing between crystal and source at different frequencies. This was in comparison to the case where no crystal was used. The focalization and self-collimation effects were promising in the homogamous case with strong matching with the dispersion curves and iso-frequency contour maps studied earlier in section 6.1. The percentage of focalization maximum intensity at the focal point to source intensity, in case of using PC at 172kHz and 20x20 crystal, 20cm source size, and in the case of no crystal are 75% and 133%, respectively. The percentage of self-collimation intensity to source intensity is 65% at 193kHz. These promising results moved us to the next step where we actually simulate the use of the crystal as a separate ultrasound lens coupled to the excitation source from one side and to the target solid object at the other side using an acoustic coupling gel. The coupling gel used in the simulation had an acoustic impedance adequately matching with the solid object and the material of the crystal was made also with the same material of the target object to allow for higher coupling efficiency. The results of the focalization and self-collimation provided in this case were very interesting with minimal insertion loss of the crystal and the matching between frequency analysis, dispersion curves and iso-frequency contour maps was very strong as well. Intensity ratio between focalization and source intensity at 172kHz is 90% while the ratio between self-collimation intensity and source intensity at 193kHz is 50%. Thus, the PC lens effectively focuses or self-collimates the beam with limited insertion loss. Comparing these results with the case of no crystal. We find that the percentage of maximum intensity to source intensity is 142% at 172kHz while at 193kHz, the percentage of maximum intensity to source intensity is 128%. A further step was required to simulate the actual response that we should meet in a real experiment

where our actual receiving sensor has a frequency bandwidth instead of the single frequency response as shown in previous analysis. We performed the frequency integration at focalization at frequency bandwidth of 10kHz with cut-off frequencies 167 to 177 kHz and self-collimation at frequency bandwidth of 10kHz with cut-off frequencies 190 to 200 kHz. The resulting simulations provided high quality focalization due to the integration of all focalization frequencies, while in the case of self-collimation, the results were affected by the integration. The reason was that the self-collimation frequency band is very narrow, this means that the receiving sensor would integrate frequency components from focalization band (below self-collimation band) and the bandgap (above the self-collimation band). This integration of unnecessary components reduces the efficiency of self-collimation detection. However, in actual cases if self-collimation is required, narrow band transducers could be used for this purpose to detect only the required frequency band and discard those that are out of interest. It was shown that the use of Phononic crystal as focusing/self-collimation lens for ultrasound wave propagation in solids is possible with proper selection of crystal parameters and a matching coupling acoustic impedance.

Future work

We believe that the work studied in this research thesis can be extended for further enhancements in the non-destructive testing techniques using laser generated ultrasound. We can enhance the wavelet algorithm discussed in chapter 3 to provide three-dimensional reconstruction of the defect by applying the clustering algorithm at a three-dimensional level. The work done in chapter 4 and 5 using SAFT algorithm can be enhanced by scanning other types of complex defects, and complex object structures. The analysis can be extended to composite materials as well. We plan to extend the simulation results presented in chapter 6 to perform lab experiments matching with the results of

simulations. We will look forward to developing and manufacturing a three-dimensional ultrasound lens to focus/self-collimate ultrasound waves propagating in solids behind the lens. In addition, we plan to extend the whole research work to industrial applications and collaborate with manufacturing companies to use our developed techniques to enhance the production quality control system by detecting defects generated during production processes.

List of publications and conferences

Excerpts of this thesis have been published in the following academic publications, book chapters and conference proceedings manuscripts.

[Journal papers]

1) H. Selim, M. Delgado-Prieto, J. Trull, R. Picó, L. Romeral, C. Cojocaru, Defect reconstruction by non-destructive testing with laser induced ultrasonic detection, Ultrasonics. 101 (2020) 106000. doi:10.1016/j.ultras.2019.106000.
2) H. Selim, M.D. Prieto, J. Trull, L. Romeral, C. Cojocaru, Laser ultrasound inspection based on wavelet transform and data clustering for defect estimation in metallic samples, Sensors (Switzerland). 19 (2019). doi:10.3390/s19030573.
3) H. Selim, J. Trull, M.D. Prieto, R. Picó, L. Romeral, C. Cojocaru, Fully noncontact hybrid NDT for 3D defect reconstruction using SAFT algorithm and 2D apodization window, Sensors (Switzerland). 19 (2019). doi:10.3390/s19092138.
4) H. Selim, R. Picó, J. Trull, M.D. Prieto, C. Cojocaru; Directional ultrasound source for solid materials inspection: diffraction management in a metallic phononic crystal, (*submitted to Sensors (Switzerland)*).

[Book chapter]

5) H. Selim, F. Piñal Moctezuma, M. Delgado Prieto, J. Francisco Trull, L. Romeral Martínez, C. Cojocaru, Wavelet Transform Applied to Internal Defect Detection by Means of Laser Ultrasound, in: Wavelet Transform Complex., IntechOpen, 2019. doi:10.5772/intechopen.84964.

[Conference proceedings]

6) H. Selim, M. Delgado, J. Trull, R. Picó, C. Cojocaru, Material Defect Reconstruction by Non-Destructive Testing with Laser Induced Ultrasonics, J. Phys. Conf. Ser. 1149 (2018). doi:10.1088/1742-6596/1149/1/012011.
7) H. Selim, R. Picó',J. Trull, M.D. Prieto, C. Cojocaru, Phononic Crystal Device As a Self-Collimator for Laser Induced Ultrasound, Congr. X I Acústica, Iberoam. Acústica, X Congr. Ibérico Español, Congr. Tec. Acústica Investig. Inst. Integr. Gestión Costeras, Zo. Val. Politècnica. (2018).

[Conference Presentation and participation]

1) 13th Intl conference on vibration measurements by laser and noncontact techniques & short course.
   Ancona, Italy, 19 - 22 June 2018.
   Contribution: Oral Presentation and Published conference paper.

2) FIA 2018 TECNIACUSTICA'18
   Cadiz (Spain), 23-27 October 2018.
   Contribution: Oral Presentation and Published conference paper.

3) SAM: Symposium on Acoustic Metamaterials - Xàtiva 2018
   Xàtiva (Spain), 7-9 November 2018
   Contribution: Participant.

References

[1] M. Abbas, M. Shafiee, Structural health monitoring (SHM) and determination of surface defects in large metallic structures using ultrasonic guided waves, Sensors (Switzerland). 18 (2018). doi:10.3390/s18113958.

[2] G. Aranguren, P.M. Monje, V. Cokonaj, E. Barrera, M. Ruiz, Ultrasonic wave-based structural health monitoring embedded instrument, in: Rev. Sci. Instrum., 2013. doi:10.1063/1.4834175.

[3] S.C. Her, S.T. Lin, Non-destructive evaluation of depth of surface cracks using ultrasonic frequency analysis, Sensors (Switzerland). 14 (2014) 17146–17158. doi:10.3390/s140917146.

[4] B. Mi, J.E. Michaels, T.E. Michaels, An ultrasonic method for dynamic monitoring of fatigue crack initiation and growth, J. Acoust. Soc. Am. 119 (2006) 74–85. doi:10.1121/1.2139647.

[5] M. Le, J. Kim, S. Kim, J. Lee, B-scan ultrasonic testing of rivets in multilayer structures based on short-time Fourier transform analysis, Meas. J. Int. Meas. Confed. 128 (2018) 495–503. doi:10.1016/j.measurement.2018.06.049.

[6] J.M.C. Ongpeng, A.W.C. Oreta, S. Hirose, Contact and noncontact ultrasonic nondestructive test in reinforced concrete beam, Adv. Civ. Eng. 2018 (2018). doi:10.1155/2018/5783175.

[7] L. Battaglini, S. Callegari, S. Caporale, L.A.J. Davis, S. Laureti, L. Senni, D.A. Hutchins, Industrial applications of noncontact ultrasonics techniques, in: Ultrason. Nondestruct. Eval. Syst. Ind. Appl. Issues, 2015: pp. 271–295. doi:10.1007/978-3-319-10566-6_11.

[8] J.F. Saillant, R. Marlier, F. Navacchia, F. Baqué, Ultrasonic transducer for non-destructive testing of structures immersed in liquid sodium at 200 °c, Sensors (Switzerland). 19 (2019). doi:10.3390/s19194156.

[9] P. Rizzo, J.G. Han, X.L. Ni, Structural health monitoring of immersed structures by means of guided ultrasonic waves, J. Intell. Mater. Syst. Struct. 21 (2010) 1397–1407. doi:10.1177/1045389X10384170.

[10] F. Ciampa, A. Mankar, A. Marini, Phononic Crystal Waveguide Transducers for Nonlinear Elastic Wave Sensing, Sci. Rep. 7 (2017). doi:10.1038/s41598-017-14594-4.

[11] C.H. Chen, Ultrasonic and advanced methods for nondestructive testing and material characterization, 2007. doi:10.1142/9789812770943.

[12] A. Surface, Directivity Patterns of Ultrasound Generated by Evanescent light at the Interface between Prism and Aluminum Surface, 34 (2013) 205–206.

[13] V. V. Krylov, Directivity patterns of laser-generated sound in solids: Effects of optical and thermal parameters, Ultrasonics. 69 (2016) 279–284. doi:10.1016/j.ultras.2016.01.011.

[14] P. Zhang, C.F. Ying, J. Shen, Directivity patterns of laser thermoelastically generated ultrasound in metal with consideration of thermal conductivity, Ultrasonics. 35 (1997) 233–240. doi:10.1016/S0041-624X(96)00106-0.

[15] J. Li, H. Zhang, C. Ni, Z. Shen, Analysis of laser generated ultrasonic wave frequency characteristics induced by a partially closed surface-breaking crack, Appl. Opt. 52 (2013) 4179–4185. doi:10.1364/AO.52.004179.

[16] X. Wang, G.M. Zhang, H. Ma, Y. Zhang, D. Wang, Measurement of a 3D ultrasonic wavefield using pulsed laser holographic microscopy for ultrasonic nondestructive evaluation, Sensors (Switzerland). 18 (2018). doi:10.3390/s18020573.

[17] T.D. Mast, G.A. Gordon, Quantitative flaw reconstruction from ultrasonic surface wavefields measured by electronic speckle pattern interferometry, IEEE Trans. Ultrason. Ferroelectr. Freq. Control. 48 (2001) 432–444. doi:10.1109/58.911726.

[18] T. Kreis, Application of Digital Holography for Nondestructive Testing and Metrology: A Review, IEEE Trans. Ind. Informatics. 12 (2016) 240–247. doi:10.1109/TII.2015.2482900.

[19] G. Wissmeyer, M.A. Pleitez, A. Rosenthal, V. Ntziachristos, Looking at sound: optoacoustics with all-optical ultrasound detection, Light Sci. Appl. 7 (2018). doi:10.1038/s41377-018-0036-7.

[20] S.M. Maswadi, B.L. Ibey, C.C. Roth, D.A. Tsyboulski, H.T. Beier, R.D. Glickman, A.A. Oraevsky, All-optical optoacoustic microscopy based on probe beam deflection technique, Photoacoustics. 4 (2016) 91–101. doi:10.1016/j.pacs.2016.02.001.

[21] R.J. Colchester, C. Little, G. Dwyer, S. Noimark, E.J. Alles, E.Z. Zhang, C.D. Loder, I.P. Parkin, I. Papakonstantinou, P.C. Beard, M.C. Finlay, R.D. Rakhit, A.E. Desjardins, All-Optical Rotational Ultrasound Imaging, Sci. Rep. 9 (2019). doi:10.1038/s41598-019-41970-z.

[22] S.L. Chen, Review of laser-generated ultrasound transmitters and their applications to all-optical ultrasound transducers and imaging, Appl. Sci. 7 (2017). doi:10.3390/app7010025.

[23] L. Cui, Y. Zhao, P. Zhao, J.C. Sun, Z.Q. Jia, Review of noncontact ultrasonic nondestructive testing for the solid materials, in: Appl. Mech. Mater., 2014: pp. 346–352. doi:10.4028/www.scientific.net/AMM.528.346.

[24] Y. Cheng, Y. Deng, J. Cao, X. Xiong, L. Bai, Z. Li, Multi-wave and hybrid imaging techniques: A new direction for nondestructive testing and structural health monitoring, Sensors (Switzerland). 13 (2013) 16146–16190. doi:10.3390/s131216146.

[25] A. Cavuto, M. Martarelli, G. Pandarese, G.M. Revel, E.P. Tomasini, Experimental investigation by laser ultrasonics for high speed train axle diagnostics, Ultrasonics. 55 (2015) 48–57. doi:10.1016/j.ultras.2014.08.010.

[26] D. Lévesque, Y. Asaumi, M. Lord, C. Bescond, H. Hatanaka, M.

Tagami, J.P. Monchalin, Inspection of thick welded joints using laser-ultrasonic SAFT, Ultrasonics. (2016). doi:10.1016/j.ultras.2016.04.001.

[27] K.A. Tiwari, R. Raisutis, O. Tumsys, A. Ostreika, K. Jankauskas, J. Jakutavicius, Defect estimation in non-destructive testing of composites by ultrasonic guided waves and image processing, Electron. 8 (2019). doi:10.3390/electronics8030315.

[28] H. Selim, M. Delgado-Prieto, J. Trull, R. Picó, L. Romeral, C. Cojocaru, Defect reconstruction by non-destructive testing with laser induced ultrasonic detection, Ultrasonics. 101 (2020). doi:10.1016/j.ultras.2019.106000.

[29] M. Le, J. Kim, S. Kim, J. Lee, Nondestructive testing of pitting corrosion cracks in rivet of multilayer structures, Int. J. Precis. Eng. Manuf. 17 (2016) 1433–1442. doi:10.1007/s12541-016-0169-7.

[30] H. Selim, M.D. Prieto, J. Trull, L. Romeral, C. Cojocaru, Laser ultrasound inspection based on wavelet transform and data clustering for defect estimation in metallic samples, Sensors (Switzerland). 19 (2019). doi:10.3390/s19030573.

[31] Y. Dun, X. Shi, Z. Xu, F. Wang, Wavelet-transform-based method of analysis for ultrasonic NDT signals of MMC adhesive interface, in: ICMIT 2005 Mechatronics, MEMS, Smart Mater., 2005: p. 604018. doi:10.1117/12.664214.

[32] H. Selim, F. Piñal Moctezuma, M. Delgado Prieto, J. Francisco Trull, L. Romeral Martínez, C. Cojocaru, Wavelet Transform Applied to Internal Defect Detection by Means of Laser Ultrasound, in: Wavelet Transform Complex., 2019. doi:10.5772/intechopen.84964.

[33] C. Prada, E. Kerbrat, D. Cassereau, M. Fink, Time reversal techniques in ultrasonic nondestructive testing of scattering media, Inverse Probl. 18 (2002) 1761–1773. doi:10.1088/0266-5611/18/6/320.

[34] H. Selim, J. Trull, M.D. Prieto, R. Picó, L. Romeral, C. Cojocaru, Fully noncontact hybrid NDT for 3D defect reconstruction using SAFT algorithm and 2D apodization window, Sensors (Switzerland). 19 (2019). doi:10.3390/s19092138.

[35] H. Selim, M. Delgado, J. Trull, R. Picó, C. Cojocaru, Material Defect Reconstruction by Non-Destructive Testing with Laser Induced Ultrasonics, in: J. Phys. Conf. Ser., 2018. doi:10.1088/1742-6596/1149/1/012011.

[36] M. Spies, H. Rieder, A. Dillhöfer, V. Schmitz, W. Müller, Synthetic aperture focusing and time-of-flight diffraction ultrasonic imaging - Past and present, in: J. Nondestruct. Eval., 2012: pp. 310–323. doi:10.1007/s10921-012-0150-z.

[37] K.A. Tiwari, R. Raisutis, V. Samaitis, Hybrid signal processing technique to improve the defect estimation in ultrasonic non-destructive testing of composite structures, Sensors (Switzerland). 17 (2017). doi:10.3390/s17122858.

[38] W. Zeng, H. Wang, G. Tian, G. Hu, Application of laser ultrasound

imaging technology in the frequency domain based on Wigner-Ville algorithm for detecting defect, Opt. Laser Technol. 74 (2015) 72–78. doi:10.1016/j.optlastec.2015.05.015.

[39] J.R. Lee, H.J. Shin, C.C. Chia, D. Dhital, D.J. Yoon, Y.H. Huh, Long distance laser ultrasonic propagation imaging system for damage visualization, Opt. Lasers Eng. 49 (2011) 1361–1371. doi:10.1016/j.optlaseng.2011.07.011.

[40] B. Park, H. Sohn, C.M. Yeum, T.C. Truong, Laser ultrasonic imaging and damage detection for a rotating structure, Struct. Heal. Monit. 12 (2013) 494–506. doi:10.1177/1475921713507100.

[41] C. Pei, T. Fukuchi, H. Zhu, K. Koyama, K. Demachi, M. Uesaka, A study of internal defect testing with the laser-EMAT ultrasonic method, IEEE Trans. Ultrason. Ferroelectr. Freq. Control. 59 (2012) 2702–2708. doi:10.1109/TUFFC.2012.2511.

[42] M.F. Kabir, D.L. Schmoldt, M.E. Schafer, Time domain ultrasonic signal characterization for defects in thin unsurfaced hardwood lumber, Wood Fiber Sci. 34 (2002) 165–182.

[43] A. Praveen, K. Vijayarekha, S. T Abraham, B. Venkatraman, Fourier Analysis of Ultrasonic TOFD Signals for Defect Detection in Austenitic Stainless Steel Welds, Int. J. Comput. Appl. 71 (2013) 14–17. doi:10.5120/12385-8737.

[44] P. Shokouhi, E. Paso, Time-Frequency Techniques for the Impact Echo Data Analysis and Interpretations, Non-Destructive Test. (2006) 1–10.

[45] Y. Zhang, L. Yang, J. Fan, Study on feature extraction and classification of ultrasonic flaw signals, WSEAS Trans. Math. (2010).

[46] M. Delgado Prieto, A. Garcia Espinosa, J.R. Riba Ruiz, J.C. Urresty, J.A. Ortega, Feature Extraction of demagnetization faults in permanent-magnet synchronous motors based on box-counting fractal dimension, IEEE Trans. Ind. Electron. 58 (2011) 1594–1605. doi:10.1109/TIE.2010.2066538.

[47] A. Praveen, Nikhilesh, K. Vijayarekha, K. Manjula, B. Venkatraman, Wavelet analysis and de-noising of signal, Res. J. Appl. Sci. Eng. Technol. 4 (2012) 5534–5538.

[48] J. Choi, J.W. Hong, Characterization of wavelet coefficients for ultrasonic signals, J. Appl. Phys. 107 (2010). doi:10.1063/1.3429087.

[49] A. Praveen, K. Vijayarekha, S.T. Abraham, B. Venkatraman, Signal quality enhancement using higher order wavelets for ultrasonic TOFD signals from austenitic stainless steel welds, in: Ultrasonics, 2013: pp. 1288–1292. doi:10.1016/j.ultras.2013.03.013.

[50] R. Raišutis, O. Tumšys, R. Kažys, L. Mažeika, A comparative study of time-frequency analysis techniques in the case of signal processing for ultrasonic NDT, Insight Non-Destructive Test. Cond. Monit. 50 (2008). doi:10.1784/insi.2008.50.11.628.

[51] H.S. Martin, Synthetic aperture ultrasound imaging with

application to interior pipe inspection, Univ. Tromsø. (2012) 1–135.
[52] Wulang Widada, Two Dimensional Window Functions, NAVAL POSTGRADUATE SCHOOL, 1979.
[53] L. De Marchi, A. Marzani, M. Miniaci, A dispersion compensation procedure to extend pulse-echo defects location to irregular waveguides, NDT E Int. 54 (2013) 115–122. doi:10.1016/j.ndteint.2012.12.009.
[54] N. Krohn, K. Pfleiderer, R. Stoessel, I. Solodov, G. Busse, Nonlinear Acoustic Imaging: Fundamentals, Methodology, and NDE-Applications, in: 2004: pp. 91–98. doi:10.1007/978-1-4020-2402-3_12.
[55] T.J. Ulrich, P.A. Johnson, A. Sutin, Imaging nonlinear scatterers applying the time reversal mirror, J. Acoust. Soc. Am. 119 (2006) 1514–1518. doi:10.1121/1.2168413.
[56] M. Miniaci, M. Mazzotti, M. Radzieński, P. Kudela, N. Kherraz, F. Bosia, N.M. Pugno, W. Ostachowicz, Application of a laser-based time reversal algorithm for impact localization in a stiffened aluminum plate, Front. Mater. 6 (2019). doi:10.3389/fmats.2019.00030.
[57] J.D.N. Cheeke, Fundamentals and applications of ultrasonic waves, second edition, 2017. doi:10.1201/b12260.
[58] T. Kundu, Ultrasonic and electromagnetic NDE for structure and material characterization: Engineering and biomedical applications, 2016.
[59] P.J. Shull, Nondestructive evaluation: Theory, techniques, and applications, 2016.
[60] R. Mohammadkhani, L.Z. Fragonara, M. Janardhan Padiyar, I. Petrunin, J. Raposo, A. Tsourdos, I. Gray, Improving depth resolution of ultrasonic phased array imaging to inspect aerospace composite structures, Sensors (Switzerland). 20 (2020). doi:10.3390/s20020559.
[61] http://nditoolbox.chriscoughlin.com/quickstart.html, (n.d.).
[62] R.X. Gao, R. Yan, Wavelets: Theory and applications for manufacturing, 2011. doi:10.1007/978-1-4419-1545-0.
[63] A. Abbate, J. Frankel, P. Das, Wavelet Transform Signal Processing Applied to Ultrasonics, in: Rev. Prog. Quant. Nondestruct. Eval., 1996: pp. 741–748. doi:10.1007/978-1-4613-0383-1_97.
[64] M.J. Gómez, C. Castejón, J.C. García-Prada, Review of recent advances in the application of the wavelet transform to diagnose cracked rotors, Algorithms. 9 (2016) 19. doi:10.3390/a9010019.
[65] K.R. Borisagar, R.M. Thanki, B.S. Sedani, K.R. Borisagar, R.M. Thanki, B.S. Sedani, Fourier Transform, Short-Time Fourier Transform, and Wavelet Transform, in: Speech Enhanc. Tech. Digit. Hear. Aids, 2019: pp. 63–74. doi:10.1007/978-3-319-96821-6_4.
[66] J. Han, M. Kamber, J. Pei, 10 – Cluster Analysis: Basic Concepts and Methods, in: Data Min. Concepts Tech., 2012: pp. 443–495.

doi:10.1016/B978-0-12-381479-1.00010-1.

[67] K.E.E. Biebler, B.P. Jäger, M. Wodney, Basic principles of data mining, in: Soc. Implic. Data Min. Inf. Priv. Interdiscip. Fram. Solut., 2009: pp. 266–289. doi:10.4018/978-1-60566-196-4.ch015.

[68] R.L. Hale, Cluster analysis in school psychology: An example, J. Sch. Psychol. 19 (1981) 51–56. doi:10.1016/0022-4405(81)90007-8.

[69] T.N. Tran, K. Drab, M. Daszykowski, Revised DBSCAN algorithm to cluster data with dense adjacent clusters, Chemom. Intell. Lab. Syst. 120 (2013) 92–96. doi:10.1016/j.chemolab.2012.11.006.

[70] N. Suthar, I.J. Rajput, V.K. Gupta, A Technical Survey on DBSCAN Clustering Algorithm, Ijser.Org. 4 (2013) 1775–1781. http://www.ijser.org/researchpaper%5CA-Technical-Survey-on-DBSCAN-Clustering-Algorithm.pdf.

[71] S. Baby, T. Balasubramanian, R.J. Pardikar, K. V. Rajkumar, T. Jayakumar, B. Raj, Sizing of cracks embedded in sub-cladding using the ultrasonic synthetic aperture focusing technique (SAFT), Insight Non-Destructive Test. Cond. Monit. 46 (2004) 26–30. doi:10.1784/insi.46.1.26.52659.

[72] R.L. Sternberg, Beamforming with Acoustic Lenses and Filter Plates, in: Prog. Underw. Acoust., 1987: pp. 651–655. doi:10.1007/978-1-4613-1871-2_77.

[73] C.M. Donahue, P.W.J. Anzel, L. Bonanomi, T.A. Keller, C. Daraio, Experimental realization of a nonlinear acoustic lens with a tunable focus, Appl. Phys. Lett. 104 (2014). doi:10.1063/1.4857635.

[74] A. Atalar, C.F. Quate, H.K. Wickramasinghe, Phase imaging in reflection with the acoustic microscope, Appl. Phys. Lett. 31 (1977) 791–793. doi:10.1063/1.89551.

[75] B. Kamgar-Parsi, L.J. Rosenblum, E.O. Belcher, Underwater imaging with a moving acoustic lens, IEEE Trans. Image Process. 7 (1998) 91–99. doi:10.1109/83.650853.

[76] S.C.S. Lin, T.J. Huang, J.H. Sun, T.T. Wu, Gradient-index phononic crystals, Phys. Rev. B - Condens. Matter Mater. Phys. 79 (2009). doi:10.1103/PhysRevB.79.094302.

[77] X. Zhang, Z. Liu, Negative refraction of acoustic waves in two-dimensional phononic crystals, Appl. Phys. Lett. 85 (2004) 341–343. doi:10.1063/1.1772854.

[78] J. Shi, S.C.S. Lin, T.J. Huang, Wide-band acoustic collimating by phononic crystal composites, Appl. Phys. Lett. 92 (2008). doi:10.1063/1.2895019.

[79] Z. He, X. Li, J. Mei, Z. Liu, Improving imaging resolution of a phononic crystal lens by employing acoustic surface waves, J. Appl. Phys. 106 (2009). doi:10.1063/1.3183908.

[80] C.N. Tsai, L.W. Chen, The manipulation of self-collimated beam in phononic crystals composed of orientated rectangular inclusions, Appl. Phys. A Mater. Sci. Process. 122 (2016). doi:10.1007/s00339-016-0187-4.

[81] J.H. Park, P.S. Ma, Y.Y. Kim, Design of phononic crystals for self-collimation of elastic waves using topology optimization method,

Struct. Multidiscip. Optim. 51 (2015) 1199–1209. doi:10.1007/s00158-014-1206-8.

[82] J.H. Page, Focusing of ultrasonic waves by negative refraction in phononic crystals, AIP Adv. 6 (2016). doi:10.1063/1.4972204.

[83] E.M. Hamham, Nonlinear self-collimated sound beams in sonic crystals, 054302 (2015) 1–6. doi:10.1103/PhysRevB.92.054302.

[84] N. Swinteck, J.O. Vasseur, C. Croënne, S. Bringuier, P.A. Deymier, S. Bringuier, Multifunctional solid / solid phononic crystal, 024514 (2017). doi:10.1063/1.4739264.

[85] V. Romero-García, R. Picó, A. Cebrecos, V.J. Sánchez-Morcillo, K. Staliunas, Enhancement of sound in chirped sonic crystals, Appl. Phys. Lett. 102 (2013). doi:10.1063/1.4793575.

[86] M. Science, Experimental observation of far-field and near-field focusing in a sonic crystal flat, (2011). doi:10.1088/0957-0233/22/11/115105.

[87] C. Croënne, E.J.S. Lee, H. Hu, J.H. Page, Band gaps in phononic crystals: Generation mechanisms and interaction effects, AIP Adv. 1 (2011) 0–13. doi:10.1063/1.3675797.

[88] B. Morvan, A. Tinel, J.O. Vasseur, R. Sainidou, P. Rembert, A.C. Hladky-Hennion, N. Swinteck, P.A. Deymier, Ultra-directional source of longitudinal acoustic waves based on a two-dimensional solid/solid phononic crystal, J. Appl. Phys. 116 (2014). doi:10.1063/1.4903076.

[89] C. Charles, B. Bonello, F. Ganot, Propagation of guided elastic waves in 2D phononic crystals, Ultrasonics. 44 (2006) 1209–1213. doi:10.1016/j.ultras.2006.05.096.

[90] R. Lucklum, Phononic crystals and metamaterials - Promising new sensor platforms, Procedia Eng. 87 (2014) 40–45. doi:10.1016/j.proeng.2014.11.261.

[91] A. Phys, Nonlinear focusing of ultrasonic waves by an axisymmetric diffraction grating embedded in water, 204103 (2016) 1–5. doi:10.1063/1.4935917.

[92] L. Maigyte, Shaping of light beams with photonic crystals : spatial filtering , beam collimation and focusing Lina Maigyte, (2014).

[93] L. Maigyte, K. Staliunas, Spatial filtering with photonic crystals, Appl. Phys. Rev. 2 (2015). doi:10.1063/1.4907345.

[94] J.H. Page, A. Sukhovich, S. Yang, M.L. Cowan, F. Van Der Biest, A. Tourin, M. Fink, Z. Liu, C.T. Chan, P. Sheng, Phononic crystals, Phys. Status Solidi Basic Res. (2004). doi:10.1002/pssb.200405363.

[95] A. Khelif, A. Adibi, Phononic crystals: Fundamentals and applications, 2015. doi:10.1007/978-1-4614-9393-8.

[96] P.K. Misra, Physics of Condensed Matter, 2010. doi:10.1016/C2010-0-65289-8.

[97] C.A. Bauer, G.R. Werner, J.R. Cary, Origin and reduction of wakefields in photonic crystal accelerator cavities, Phys. Rev. Spec. Top. - Accel. Beams. 17 (2014) 1–12. doi:10.1103/PhysRevSTAB.17.051301.

[98] I. Pérez-Arjona, V.J. Sánchez-Morcillo, J. Redondo, V. Espinosa, K.

Staliunas, Theoretical prediction of the nondiffractive propagation of sonic waves through periodic acoustic media, Phys. Rev. B - Condens. Matter Mater. Phys. 75 (2007) 1–7. doi:10.1103/PhysRevB.75.014304.

[99] S. Alagoz, An analysis of the spatio-spectral acoustic filtering effect of sonic crystals, Chinese J. Phys. 54 (2016) 788–794. doi:10.1016/j.cjph.2016.08.003.

[100] S. Tol, F.L. Degertekin, A. Erturk, 3D-printed phononic crystal lens for elastic wave focusing and energy harvesting, Addit. Manuf. 29 (2019). doi:10.1016/j.addma.2019.100780.

[101] Y. Sun, Y. Yu, Y. Zuo, L. Qiu, M. Dong, J. Ye, J. Yang, Band gap and experimental study in phononic crystals with super-cell structure, Results Phys. 13 (2019) 102200. doi:10.1016/j.rinp.2019.102200.

[102] L. Maigyte, K. Staliunas, Spatial filtering with photonic crystals, Appl. Phys. Rev. 2 (2015). doi:10.1063/1.4907345.

[103] a Abbate, J. Koay, J. Frankel, S.C. Schroeder, P. Das, Signal detection and noise suppression using a wavelet transform signal processor: application to ultrasonic flaw detection., IEEE Trans. Ultrason. Ferroelectr. Freq. Control. 44 (1997) 14–26. doi:10.1109/58.585186.

[104] N. B. Hamadi, S. Omri, Uncertainty principles for the continuous wavelet transform in the Hankel setting, Appl. Anal. 97 (2018) 513–527. doi:10.1080/00036811.2016.1276169.

[105] Q. Shan, R.J. Dewhurst, Surface-breaking fatigue crack detection using laser ultrasound, Appl. Phys. Lett. 62 (1993) 2649–2651. doi:10.1063/1.109274.

[106] S. Boonsang, J. Zainal, R.J. Dewhurst, Synthetic aperture focusing techniques in time and frequency domains for photoacoustic imaging, Insight Non-Destructive Test. Cond. Monit. 46 (2004) 196–199. doi:10.1784/insi.46.4.196.55648.

[107] T. Stepinski, F. Lingvall, Synthetic aperture focusing techniques for ultrasonic imaging of solid objects, Proc. Eur. Conf. Synth. Aperture Radar, EUSAR. (2010) 438–441. doi:papers2://publication/uuid/72BB2E26-227F-4027-9433-3990165E5916.

[108] J.A. Jensen, S.I. Nikolov, K.L. Gammelmark, M.H. Pedersen, Synthetic aperture ultrasound imaging, Ultrasonics. 44 (2006). doi:10.1016/j.ultras.2006.07.017.

[109] R.S.C. Cobbold, Foundations of Biomedical Ultrasound, Oxford Univ. Press. (2007) 45–51.

[110] T.L. Szabo, Diagnostic Ultrasound Imaging: Inside Out: Second Edition, 2004. doi:10.1016/C2011-0-07261-7.

[111] PANAMETRICS, Ultrasonic transducers, n.d. https://www.olympus-ims.com/data/File/panametrics/panametrics-UT.en.pdf.

[112] X.G. Wang, W.L. Wu, Z.C. Huang, J.J. Chang, N.X. Wu, Research on the transmission characteristics of air-coupled ultrasound in

double-layered bonded structures, Materials (Basel). 11 (2018). doi:10.3390/ma11020310.

[113] R. Picó, V.J. Sánchez-Morcillo, I. Pérez-Arjona, K. Staliunas, Spatial filtering of sound beams by sonic crystals, Appl. Acoust. 73 (2012) 302–306. doi:10.1016/j.apacoust.2011.09.011.

[114] E. Soliveres, I. Pérez-Arjona, R. Picó, V. Espinosa, V.J. Snchez-Morcillo, K. Staliunas, Simultaneous self-collimation of fundamental and second-harmonic in sonic crystals, Appl. Phys. Lett. 99 (2011). doi:10.1063/1.3643497.

[115] V.J. Sánchez-Morcillo, K. Staliunas, V. Espinosa, I. Pérez-Arjona, J. Redondo, E. Soliveres, Propagation of sound beams behind sonic crystals, Phys. Rev. B - Condens. Matter Mater. Phys. 80 (2009). doi:10.1103/PhysRevB.80.134303.